SANDIA REPORT
SAND98–2456
Unlimited Release
Printed November 1998

An Investigation of Wavelet Bases for Grid-Based Multi-Scale Simulations

Final Report

Mark A. Christon, Timothy G. Trucano, Joe R. Weatherby, Roy S. Baty, Shawn P. Burns, David W. Roach, David E. Womble, Thomas E. Voth

Prepared by
Sandia National Laboratories
Albuquerque, New Mexico 87185 and Livermore, California 94550

Sandia is a multiprogram laboratory operated by Sandia Corporation, a Lockheed Martin Company, for the United States Department of Energy under Contract DE-AC04-94AL85000.

Sandia National Laboratories

Issued by Sandia National Laboratories, operated for the United States Department of Energy by Sandia Corporation.

Available to DOE and DOE contractors from
Office of Scientific and Technical Information
P.O. Box 62
Oak Ridge, TN 37831

Prices available from (615) 576-8401, FTS 626-8401

Available to the public from
National Technical Information Service
U.S. Department of Commerce
5285 Port Royal Rd
Springfield, VA 22161

NTIS price codes
Printed copy: A03
Microfiche copy: A01

SAND98-2456
Unlimited Release
Printed November 1998

An Investigation of Wavelet Bases for Grid-Based Multi-Scale Simulations[1]

Final Report

Mark A. Christon, Timothy G. Trucano and Joe R. Weatherby
Computational Physics R & D Department

Roy S. Baty
Aerosciences & Computational Fluid Mechanics Department

Shawn P. Burns
The Unsteady & Reactive Fluid Mechanics Department

David W. Roach and David E. Womble
Applied Mathematics Department

Thomas E. Voth
Thermal Sciences Department

Sandia National Laboratories
P. O. Box 5800
Albuquerque, NM 87185-0819

[1]Keywords and Phrases: wavelets, multi-wavelets, reproducing kernel, multi-resolution.

Abstract

The research summarized in this report is the result of a two-year effort that has focused on evaluating the viability of wavelet bases for the solution of partial differential equations. The primary objective for this work has been to establish a foundation for hierarchical/wavelet simulation methods based upon numerical performance, computational efficiency, and the ability to exploit the hierarchical adaptive nature of wavelets. This work has demonstrated that hierarchical bases can be effective for problems with a dominant elliptic character. However, the strict enforcement of orthogonality was found to be less desirable than weaker semi-orthogonality or bi-orthogonality for solving partial differential equations. This conclusion has led to the development of a multi-scale linear finite element based on a hierarchical change of basis. The reproducing kernel particle method has been found to yield extremely accurate phase characteristics for hyperbolic problems while providing a convenient framework for multi-scale analyses.

Acknowledgments

The authors of this manuscript would like to acknowledge the contributions of Prof. Wing Kam Liu at Northwestern University, Prof. Douglas P. Hardin at Vanderbilt University, and Prof. Peter M. Massopust at Sam Houston University. In particular, the contributions by Prof. Hardin on the semi-orthogonal wavelets and Schauder basis were significant and his hard work is greatly appreciated. The principal investigator also wishes to thank Philip M. Gresho at Lawrence Livermore National Laboratory for his helpful suggestions. Special thanks go to Thomas M. Smith and Allen C. Robinson for reading the preliminary version of this manuscript. In addition, the principal investigator would like to acknowledge the support of the Computation, Computers and Math Center at Sandia National Laboratories in this endeavor.

Contents

List of Figures

List of Tables

Chapter 1

Introduction

Wavelets are a relatively new mathematical tool that dissect data, functions, and differential operators into components of different frequency with a resolution (in space or time) that is simultaneously matched to the scale of each component. The use of wavelet bases for the solution of partial differential equations (PDEs) has promised to deliver hierarchical solutions matched to the scales of the physical problem. The application of wavelet bases to the solution of partial differential equations has evolved to the point where there are a number of competing formulations that include, but are not limited to wavelet-Galerkin, wavelet-collocation, and reproducing kernel methods.

Despite the growing number of formulations and solution algorithms that use wavelets, the field is still relatively new, and many technical issues remain. The state of wavelet bases for solving partial differential equations is roughly that of finite element technology 20 years ago. That is to say there is great promise in this approach, but there is a clear need for fundamental research that characterizes the numerical and computational performance of wavelets for the solution of partial differential equations. Before proceeding with a historical perspective on wavelets and their application to partial differential equations, a brief introduction to wavelets is presented first in words and then using the mathematical formalisms of the wavelet community.

The objective for wavelet decompositions is to represent a function in terms of multiple scales of resolution – particularly functions that are local in both time and frequency (or space and wave number). A precise definition of wavelets is somewhat elusive, but one of the best overall definitions is given by Chui:[20]

> The term "wavelets" has a very broad meaning, ranging from singular integral operators of the Calderòn type in harmonic analysis to sub-band coding algorithms in signal processing, from coherent states in quantum physics to spline analysis in approximation theory, from multi-resolution transform in computer vision to a multilevel approach in the numerical solution of partial differential equations, and so on.

To be a bit more precise, wavelets permit the representation of functions in terms of a family of wavelet basis functions and their associated wavelet coefficients, i.e., $f(x) = \sum a_{j,k}\psi(2^j x - k)$, where $\psi(2^j x - k)$ are the wavelets and $a_{j,k}$ are the coefficients. Wavelets are based on the application of translation $(\psi(x) \rightarrow \psi(x-k))$, and dilation $(\psi(x) \rightarrow \psi(jx))$. Here, j is the dilation parameter and is understood to range over all the scales of interest, while k indicates the translation and ranges over all possible integer translates (shifts). The construction of a wavelet begins with a dilation equation, that is, a two-scale difference equation, and its solution which is typically referred to as the scaling function, ϕ. The wavelet at a given scale can be expressed in terms of differences of scaling functions. With the definition of wavelets in "words" out of the way, attention is turned to the mathematical foundation for wavelets and multi-resolution analysis.

1.1 Multi-Resolution Analysis and Wavelets

The relationship between the scaling function or "mother" wavelet and the wavelets themselves was suggested above, but the details of this relationship were not made precise in a mathematical sense. The basic idea behind the relationship hinges on a multi-resolution analysis whose goal is to break down the original $\mathbf{L}^2(\mathbb{R})$ space into a sequence of nested subspaces. The multi-scale representation of a function in $\mathbf{L}^2(\mathbb{R})$ (see Daubachies[36]) relies upon a sequence of nested subspaces, $\mathcal{V}_j$ such that

$$\{0\} \cdots \subset \mathcal{V}_{-1} \subset \mathcal{V}_0 \subset \mathcal{V}_1 \subset \mathcal{V}_2 \cdots \subset \mathbf{L}^2(\mathbb{R}). \tag{1.1}$$

The nested subspaces have the following properties.

(a) The closure of the subspaces is dense in $\mathbf{L}^2(\mathbb{R})$, $\overline{\cup_{j\in\mathbf{Z}}\mathcal{V}_j} = \mathbf{L}^2(\mathbb{R})$, where $\mathbf{Z}$ is the set of integers.

(b) The intersection of the subspaces is the trivial space, $\bigcap_{j\in\mathbf{Z}} \mathcal{V}_j = \{0\}$.

(c) The embedded spaces in a multi-resolution analysis are related by a scaling law where

$$f(x) \in \mathcal{V}_j \Longleftrightarrow f(2x) \in \mathcal{V}_{j+1}. \tag{1.2}$$

(d) There exists a refinable function whose integer translates form an orthogonal basis for the central space, $\mathcal{V}_0$, i.e.,

$$\mathcal{V}_0 = span\{\phi(x-k), k \in \mathbf{Z}\}. \tag{1.3}$$

This refinable function is referred to as the scaling function.

In the nested sequence of spaces, the $\mathcal{V}_0$ subspace lies in the $\mathcal{V}_1$ subspace, and so, any function in $\mathcal{V}_0$ may be expressed in terms of the scaling functions in $\mathcal{V}_1$. That is,

$$\phi(x) = \sum_{k=-\infty}^{\infty} a_k \phi(2x-k), \tag{1.4}$$

where $k \in \mathbf{Z}$, and a_k are coefficients that must be computed for the two-scale difference relation. Equation (1.4) is the *dilation* equation, and it is sometimes referred to as the *refinement* equation.

In the more general case, for a given scale, j,

$$\phi_{j,k}(x) = 2^{j/2}\phi(2^{j/2}x - k), \tag{1.5}$$

where k represents the integer translates of the scaling function. In the subsequent chapters, the dilation parameter, j, will be referred to frequently as the "scale".

Example 1 *Translation and Dilation*

Two examples of translation and dilation are shown in Figure 1.1 for the box and hat functions. Here, the box function is the piecewise constant function,

$$\phi(x) = \begin{cases} 1, & \text{if } 0 \le x \le 1, \\ 0, & \text{otherwise,} \end{cases} \tag{1.6}$$

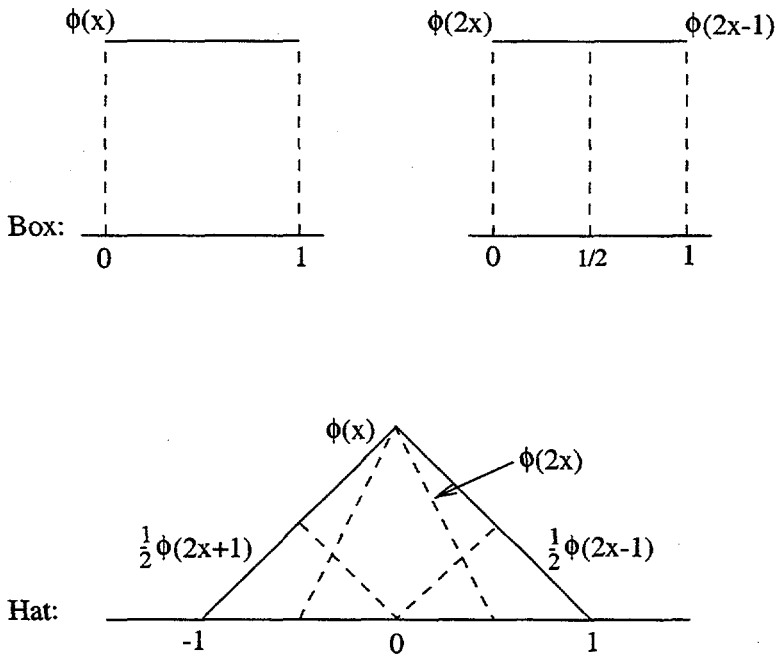

Figure 1.1: Translation and dilation of the box function and hat function.

and satisfies $\phi(x) = \phi(2x) + \phi(2x+1)$. *Similarly, the hat function is*

$$\phi(x) = \begin{cases} 1 - |x|, & \text{if } 0 \leq |x| \leq 1, \\ 0, & \text{otherwise,} \end{cases} \tag{1.7}$$

and satisfies $\phi(x) = \frac{1}{2}\phi(2x+1) + \phi(2x) + \frac{1}{2}\phi(2x-1)$ *as its dilation equation. Unlike the constant function, the hat function is not orthogonal to its integer translates and requires an orthogonalization procedure for use as a scaling function in the linear spline Battle-Lemarie' construction.*[36]

Attention is now turned to the wavelets and their subspaces. The difference between subspaces at different scales is key in the construction of the wavelets and in multi-resolution analysis. For every scale, j, the wavelet subspace, $\mathcal{W}_j$, is defined to be the orthogonal complement of $\mathcal{V}_j$ in $\mathcal{V}_{j+1}$ as

$$\mathcal{V}_{j+1} = \mathcal{V}_j \bigoplus \mathcal{W}_j, \tag{1.8}$$

where $\bigoplus$ indicates an orthogonal direct sum, $\mathcal{V}_j \perp \mathcal{W}_j$, and $\mathcal{W}_{j'} \perp \mathcal{W}_j$ for $j' \neq j$. From this, it follows that the wavelet spaces provide an orthogonal

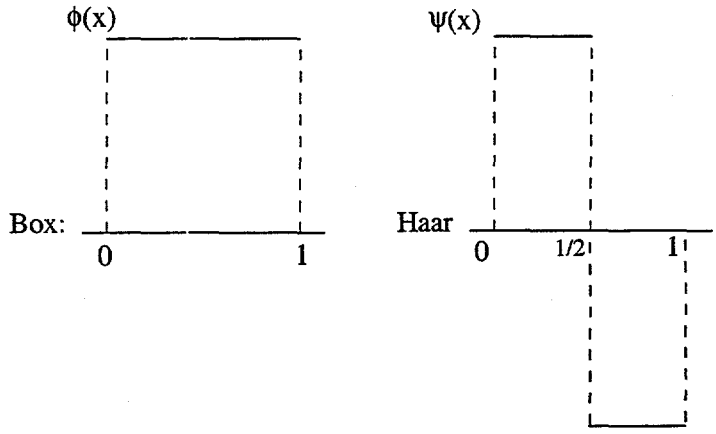

Figure 1.2: Box function and the corresponding Haar wavelet.

decomposition of $\mathbf{L}^2(\mathbb{R})$,

$$\bigoplus_{j\in\mathbf{Z}} \mathcal{W}_j = \mathbf{L}^2(\mathbb{R}). \tag{1.9}$$

Like the scaling functions, the wavelets can be defined in terms of a two-scale difference equation as

$$\psi_{j,k}(x) = 2^{j/2}\psi(2^{j/2}x - k), \tag{1.10}$$

where

$$\mathcal{W}_j = span\{2^{j/2}\psi(2^j x - k), k \in \mathbf{Z}\}. \tag{1.11}$$

As an example of this relationship, the wavelet that corresponds to the box function in Figure 1.1 is the Haar wavelet shown in Figure 1.2.

With the basics for the relationship between the wavelet and scaling function defined, attention is turned to the projection of a function onto a wavelet basis. Here, $\mathcal{P}_j f$ represents the projection of a function, f onto the space $\mathcal{V}_j$, and $\mathcal{Q}_j f$ represents the projection of f onto the wavelet space, $\mathcal{W}_j$. Making use of the orthogonality between $\mathcal{V}_j$ and $\mathcal{W}_j$,

$$\mathcal{P}_j f = \mathcal{P}_{j-1} f + \mathcal{Q}_{j-1} f. \tag{1.12}$$

Here, the projection operators are idempotent and orthogonal, i.e., $\mathcal{P}_j^2 = \mathcal{P}_j$, $\mathcal{Q}_j^2 = \mathcal{Q}_j$, and $\mathcal{P}_j\mathcal{Q}_j = \mathcal{Q}_j\mathcal{P}_j = 0$. In Eq. (1.12), the projection onto the wavelet basis, $\mathcal{Q}_{j-1}f$ constitutes the detail in the projected function that is required to move from a coarse level to a level with higher resolution. From

this point of view, multi-resolution decomposition breaks $\mathbf{L}^2(\mathbb{R})$ into a series of orthogonal subspaces at varying resolution. At each level of resolution, j, a function in $\mathbf{L}^2(\mathbb{R})$ may be represented in terms of the scaling functions at scale j, or in terms of scaling functions and wavelets at scale $j-1$.

Example 2 *Projections*

As a simple example, consider the projection of $f(x) = \sin(\pi x)$ *onto* $\mathcal{V}_0$ *with the scaling function being the "box" function defined by Eq. (1.6), and* $0 \leq x \leq 1$. *The projection onto this function is simply*

$$\mathcal{P}_0 f(x) = \int_0^1 \sin(\pi x)\phi(x)dx = \frac{2}{\pi}, \tag{1.13}$$

and is shown in Figure 1.3 as the Scale-0 projection. The amplitude of the constant function, $\mathcal{P}_0 f(x)$ *is* $\pi/2$ *which is the area under the half-sine wave.*

Similarly, the result of projecting onto the next finer grid associated with $\mathcal{V}_1$ *yields* $\mathcal{P}_1 f(x) = \frac{2}{\pi}\phi(2x) + \frac{2}{\pi}\phi(2x-1)$. *This is shown as the Scale-1 projection in Figure 1.3, and again the area is preserved in the orthogonal projection onto* $\mathcal{V}_1$. *Note that both the Scale-0 and Scale-1 projections yield a "top-hat" representation of the half-sine wave, albeit a top-hat representation with the area equal to that under the half-sine wave.*

Subsequent projections onto increasingly larger spaces yields more accurate representations of the original sine function. Between any two scales, the difference between the discrete functions is clearly seen to be the projection onto the space associated with the Haar wavelet at a given scale. For example, to move from Scale-2 to Scale-3, the $\mathcal{Q}_2 f(x)$ *projection may be computed directly using the Haar wavelet rather than the box functions at Scale-3, i.e.,* $\mathcal{P}_3 f(x) = \mathcal{P}_2 f(x) + \mathcal{Q}_2 f(x)$.

This brief overview of scaling functions, wavelets and multi-resolution analysis has been presented as background for the chapters that follow in this report. Additional details on wavelet construction and multi-resolution analysis may be found in Strang,[88,89] Daubechies,[35,36] Mallat,[74] Meyer,[77] Strichartz,[93] Massopust,[75,76] Williams,[107] Graphs,[44] Jawerth,[54] and Chui.[20] Attention is now turned to a review of the salient literature on the solution of partial differential equations using wavelet bases.

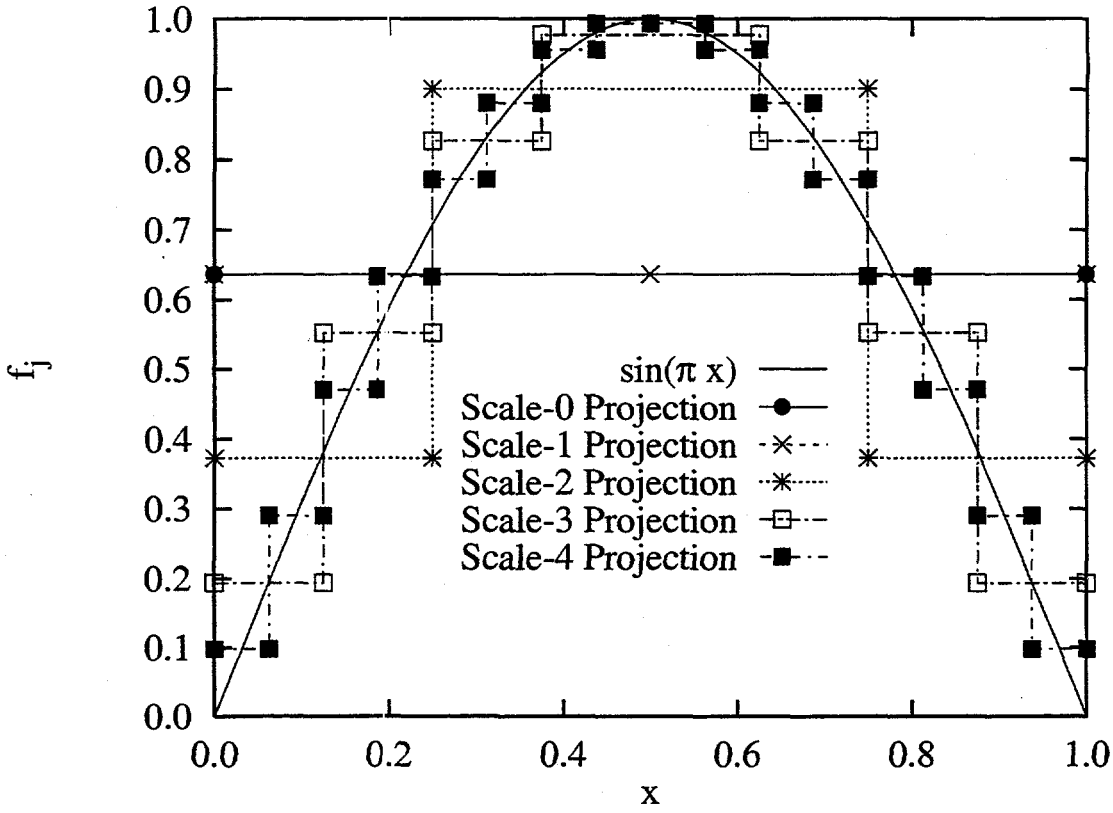

Figure 1.3: Multi-scale projection of $f(x) = sin(\pi x)$ onto $\mathcal{V}_j$, for $j = 0, 1, 2, 3, 4$.

1.2 Historical Perspective

The name "wavelet" or "ondelette" was coined in the early 1980s by French researchers Morlet, Arens, Fourgeua, Giard and Grossman.[47,79,80] However, functions with the attributes of wavelets have been known for almost 100 years. Meyer[77] points out that there are seven primary origins for wavelets that date from around 1930 with the Haar wavelet dating back to 1909. However, the literature from this era does not use the term "wavelet", and it has been asserted that this work did not explicitly include the concepts of multi-resolution analysis.

A brief overview of some of the current literature on wavelet based approaches to solving is presented in the subsequent sections. For a recent survey of the current state of wavelets and multi-scale methods for solving

partial differential equations, see Dahmen et al.[30] and Dahmen.[33] As a cautionary word, the literature survey presented here is undoubtedly incomplete. The rate at which publications on wavelets for partial differential equations have appeared in the last two years has made it difficult to present all of the recent work in this area.

1.2.1 Finite Difference and Collocation Methods

There has been a variety of work with wavelets in both finite difference and in collocation methods. In 1994, Jameson[53] introduced a finite difference scheme that used Daubachies wavelets. The use of Daubachies wavelets was shown to yield a method that is equivalent to a finite difference scheme with adaptive grid refinement where local refinement is based upon the decomposition of the local solution. In 1995, Harten[49] demonstrated the use of wavelets and multi-resolution analysis in the computation of the time-evolution of hyperbolic conservation laws where the solution at each time level was represented in terms of the wavelet coefficients. This representation yielded a numerical solution strategy where data compression was built into the method. In this work, the computational complexity of the time-integration scheme was shown to be directly dependent on the rate of data compression.

Cai and Wang[13,14] (1996, 1993) used a cubic spline wavelet with a discrete wavelet transform and collocation in their method for solving PDEs. Adaptivity was introduced in the solution procedure by examination of the amplitude of the wavelet coefficients at a given time step. A similar approach has been taken by Vasilyev and Paolucci[98,99] (1996,1997) where the computational cost of their method has been demonstrated to be on the order of the total number of collocation points and independent of the spatial dimension of the problem. Holmström[50] (1996) introduced an interpolating wavelet transform and used a threshold on the amplitude of the wavelet coefficients to obtain adaptive solutions for hyperbolic PDEs. Holmström also demonstrated that the order of accuracy of the underlying finite difference discretization is preserved with the interpolating wavelet transform. More recently, work by Cai and Zhang[15] (1997) has extended the adaptive spline wavelet method in order to treat reaction-diffusion equations for reacting flows.

1.2.2 Wavelet-Galerkin Methods

The wavelet-Galerkin method has received a great deal of attention over the past 7-8 years. This is undoubtedly due to the generality that the Galerkin method provides, and the ease with which alternative bases may be implemented and tested. In this section, only a subset of the past work is reviewed, beginning in 1990.

Glowinski et al.[41] (1990) investigated the use of Daubechies wavelets to both linear and nonlinear elliptic, parabolic and hyperbolic PDEs in one space dimension. In this work, they concluded that wavelet bases compared favorably with both traditional finite elements and finite difference methods, combining aspects of both finite element and spectral methods. In addition, it was suggested that wavelet bases lend themselves naturally to multi-level solution methods, but that the extension to multiple dimensions is non-trivial. Although a multi-level approach is outlined, scaling functions are used for the test and trial functions, and no direct use of the wavelets in the solution algorithm is apparent.

Latto and Tenenbaum[61] (1990) also used Daubachies wavelets ($D6^{36}$) in the solution of equation with a Galerkin procedure. In this work, only the Daubechies scaling functions were used in the solution method.

Glowinski et al.[42] (1992) used a Galerkin procedure to solve an elliptic PDE in two space dimensions with a "fictitious domain" treatment for the boundary, i.e., a uniform grid imposed over an irregular domain. Again, Daubachies scaling functions were used as the basis, and it was determined that the wavelet-Galerkin method is "comparable" to the classical finite element method. Also in 1992, Wells and Zhou[104] considered the use of wavelets to represent domains and boundary data for the solution of elliptic partial differential equations. In 1993, Wells et al.[105] introduced a penalty method in conjunction with a fictitious domain using the wavelet boundary representation.

Xu and Shann[108] (1992) also used Daubachies wavelets in the solution of one-dimensional elliptic problems using orthogonality of the wavelets in the construction of an iterative solution strategy. Here, only Dirichlet boundary conditions were considered and a change of basis was used to reduce the operations count during the iterative solution procedure. The relationship between the change of basis and a hierarchical basis (see Yserentant[109]) is illustrated in this paper.

In 1993, Dahlke and Weinreich[23] adapted biorthogonal wavelets to a

Galerkin procedure for the solution of integral and partial differential equations. Biorthogonality refers to the fact that a scaling function and its dual are used as generators for the multi-resolution analysis with orthogonality between the primary and dual basis. More precisely, the orthogonality between $\mathcal{V}_m$ and $\mathcal{W}_m$ is relaxed with the requirement that $\mathcal{V}_m \cap \mathcal{W}_m = \{0\}$ imposed instead. A wavelet-Galerkin procedure was considered, and it was demonstrated that the biorthogonal wavelet bases yield stiffness matrices with uniformly bounded condition numbers. Dahlke and Kunoth,[22] also in 1993, formulated a Galerkin method using biorthogonal wavelets and a two-grid solution strategy that made use of the wavelets for the construction of the restriction and prolongation operations.

Qian and Weiss[84] (1993) used Daubachies scaling functions to solve a Helmholtz equation in two dimensions. Here, the wavelet-Galerkin method was demonstrated to converge when their finite difference schemes failed to do so.

The use of wavelets has also emerged in multi-level schemes and preconditioners. An early example of this is demonstrated by Rieder et al.[85] (1993) in the construction of a wavelet based version of Hackbusch's frequency decomposition multi-grid method.[48] A later paper by Rieder et al.[86] (1994) considers the application of the wavelet-based frequency decomposition multi-grid scheme and demonstrates that the wavelet reconstruction yields a robust multi-level algorithm. Work by Glowinski et al.,[43] also in 1994, used a wavelet multi-grid preconditioner with a wavelet-Galerkin discretization of Dirichlet boundary-value problems with the penalty/fictitious domain approach.

The work by Amaratunga and Williams[1] (1994) used Daubachies D6, D8, D10, and D12 scaling functions with a Galerkin procedure to generate solutions to a Helmholtz equation on a periodic domain in one spatial domain. Comparisons with finite difference solutions illustrated that the "wavelet" (actually scaling function) solutions converged more rapidly, albeit with an additional cost for the boundary treatment.

In 1994, Ko and his co-workers[58] developed triangular wavelet-based finite elements. In this work application to elliptic problems in a unit square is demonstrated. However, no assessment of the computational complexity or numerical performance of these elements was made.

Also in 1994, Urban[97] demonstrated the construction and application of divergence-free refinable functions for incompressible flow. The use of multi-level preconditioning yielded uniformly bounded condition numbers

for Stokes flow in a lid-driven cavity. Later work by Dahmen, Kunoth and Urban[29] (1995) demonstrated that wavelet-Galerkin methods with shift-invariant refinable spaces yield trial spaces that satisfy the LBB (Ladysenkaya-Babuska-Brezzi), i.e., the div-stability, condition. Here, a multi-scale decomposition of the Schur complement of the discrete system is suggested for time-dependent problems.

In related work, Kunoth[59] (1994) developed a class of multi-level preconditioners for elliptic boundary value problems. In 1995, Perrier and Charton[82] demonstrated the solution of the incompressible, time-dependent, Navier-Stokes equations using a wavelet-Galerkin method. A subsequent effort by Charton and Perrier[16] in 1996 used collocation for the non-linear advective terms, and presented comparisons with calculations using a spectral code. Identical results were obtained with both the wavelet and spectral approaches although the computational effort for the wavelet code was higher. More recently, Weiss[103] (1997) has used the wavelet-Galerkin method for the study of enstrophy transfers in two-dimensional turbulence in simple geometries.

Strela and Strang[91] (1995) have constructed finite element multi-wavelets that have local support on "two intervals" with the wavelet subspace spanned by wavelets with support over "three intervals". Simple examples of these elements consist of the linear hat-function and its associated sombrero wavelet. In their construction, the resulting finite elements are orthogonal to the wavelets and their translates, but the wavelets are only semi-orthogonal, i.e., orthogonal across scales.

The treatment of boundary conditions – especially for more traditional wavelets, i.e., Daubachies wavelets – has proven somewhat problematic. The work by Monasse and Perrier[78] (1995) is one of the few efforts that has explicitly considered the implications of boundary conditions on multi-resolution analysis in the context of solving partial differential equations.

In 1997, Walter[102] extended the work of Strela and Strang by proposing a Sobolev inner product to make the scaling functions orthogonal to their translates yielding simplified decomposition – reconstruction algorithms. Later work by Strela and Strang[92] (1997) proposed a pseudo-biorthogonal completion of Hermite cubics for finite elements as a means to obtain wavelets that are "quick" to evaluate in a Galerkin procedure.

As an aside, Latto, Resnikoff and Tenenbaum[60] (1996) present a method for evaluating "connection coefficients" for wavelet-Galerkin applications. Dahmen and Micchelli[31] in 1993 also considered the evaluation of Galerkin integrals that involve derivatives of wavelets and demonstrated that the eval-

uation of the Galerkin integrals reduces to an eigenvector-moment problem.

The application of wavelets that are constructed to be biorthogonal in the sense of a weighted inner product was demonstrated by Sweldens[94] in 1996. For an inner product of the form $< \mathcal{L}u, v >$, it was shown that the biorthogonal wavelets can diagonalize the operator. In Sweldens work, it was suggested that a similar idea could be used for more general operators such as the weak-form of the Helmholtz equation. (Chapters 3 and 4 follow this general line of reasoning.)

Work on element-by-element construction methods has been reported by Dahmen and Stevenson[34] (1997) with a focus on wavelets for unstructured grids that yield uniformly bounded condition numbers for elliptic operators. Here, the construction procedure relies strictly on a uniform refinement of the initial elements – a small penalty in the mesh generation process.

Fröhlich and Schneider[39] (1997) have used operator-adapted biorthogonal wavelets with a discrete wavelet transform and semi-implicit time integration to yield a Petrov-Galerkin method with a diagonalized stiffness operator. These authors refers to this method as a "adaptive inversion scheme" since there is no linear system to be solved at each time step.

As evidenced by the brief review of this wavelet-Galerkin literature, the work in the early 1990s relied heavily on Daubechies wavelets. However, the trend in recent years has been away from Daubachies wavelets and towards wavelets that are constructed to yield specific algorithmic properties, e.g., diagonalize the stiffness operator for elliptic problems. The strict use of orthogonality has been relaxed[32] yielding biorthogonal and semi-orthogonal wavelets. This approach has led to the idea that wavelets may be most useful for solving PDEs if they are used to simply "complete" a space, i.e., moving from $\mathcal{V}_{m-1}$ to $\mathcal{V}_m$. These ideas have been used in the work reported on in the subsequent chapters.

1.2.3 Reproducing Kernel Methods

An alternative to traditional grid-based approaches is the class of methods based on moving least-squares, reproducing kernels, and partitions of unity. An overview of the development of these methods is presented by Belytschko, et al.[3] The methods based upon reproducing kernels are of interest here because they promise to deliver enhanced numerical performance on a broad range of physical problems and provide a framework for incorporating multi-resolution analysis in PDE solution algorithms.

Liu and his co-workers have been developing Reproducing Kernel Particle Methods (RKPM) for a number of years and have demonstrated applications ranging from structural acoustics to large deformation mechanics problems.[66–68,71] In addition, Liu et al.[65,73] have combined reproducing kernel ideas with multi-resolution analysis using wavelets, permitting the decomposition of discrete solutions into multiple scales. The application of RKPM to structural dynamics has been demonstrated by Liu et al.[70] in addition to showing that the reproducing kernel interpolation functions satisfy necessary consistency conditions. Uras et al.[96] have applied RKPM to acoustics problems demonstrating that the dilation parameter in the window function may be used to perform the RKPM analogue of "h-p adaptivity".

In a series of papers by Liu, Li and Belytschko[62,64,72] moving least squares reproducing kernel methods are developed beginning with the basic formulation and continuing through a Fourier analysis and the incorporation of wavelet packets. The possibility for RKPM to deliver equivalent rates of convergence for the discrete functions and their derivatives has also been explored by Li and Liu.[63] The term "synchronized convergence" has been coined for the situation when convergence rates for the functions and their derivatives are of equal order. The application of RKPM to nearly incompressible, hyper-elastic solids was considered by Chen et al.,[17] while the treatment of large deformation problems has been explored by Liu et al.[55,69] The enrichment of finite element computations with RKPM has also been addressed permitting local regions of the computational domain to be treated with RKPM while the global problem is treated with a standard finite element formulation.[18]

1.2.4 Multi-Level Methods

A topic closely related to the use of wavelets in the solution of partial differential equations is the use of wavelets for multi-level preconditioners. The use of multi-level splitting of finite element spaces is discussed in Chapters 3 and 4 below. A brief and incomplete historical review of the relevant literature is presented here.

In 1986, Yserentant[109] introduced the use of multi-level splitting of finite element spaces in the solution of elliptic partial differential equations. Here, the principal idea was to replace the usual finite element nodal basis by an equivalent hierarchical basis. The effect of the change of basis is a preconditioning of the discrete operator that results in uniformly bounded

condition number in one-dimension, and a condition number that grows as $O(\log(1/h^2))$ in two-dimensions. Later work by Yserentant[111] (1990) compared the hierarchical basis preconditioner to the Bramble, Pasciak and Xu[12] (BPX) preconditioner and demonstrated that there is a close relationship between the two approaches.

The work by Tong, Chan and Kuo[95] in 1991 used a nodal change of basis as a preconditioner and demonstrated that their method yields condition numbers that grow as $O(\log^2(1/h))$ in two dimensions with condition numbers of $O(1)$ for their model Poisson problem. In 1992, Dahmen and Kunoth[28] derived general estimates for condition numbers for elliptic problems where a multi-level preconditioning is used. These estimates were used to demonstrate that the BPX preconditioner yields uniformly bounded condition numbers. Jaffard[52] has also considered the use of wavelets that provide, in effect, preconditioning for an elliptic PDE in the context of a Galerkin procedure. Here, diagonal preconditioning of the wavelet-based elliptic operator is used to yield a uniformly bounded condition number.

A detailed theoretical treatment of finite element multi-level methods may be found in Oswald[81] (1994). More recent work by Dahmen et al.[30] (1997) considers the relationship between multi-grid and multi-scale decompositions and the use of multi-scale methods for physical problems with strong material anisotropy.

1.2.5 Fast Wavelet Algorithms and Nonstandard Forms

Since about 1990, Beylkin and his colleagues have been developing wavelet centric algorithms for a broad range of applications. A review of this work is presented in a separate context because it is not easily categorized with wavelet-Galerkin, wavelet-collocation, finite differences, or multi-level methods.

In the early 1990s, Beylkin et al.[10] introduced a new class of numerical algorithms designed to achieve fast wavelet transforms. The importance of orthogonality, vanishing moments and recursion in terms of fast algorithms for multi-resolution analysis was presented by Beylkin[5] in 1991. In 1992 – 1993, fast wavelet algorithms were developed for point-wise function multiplication,[6] as well as for the representation of operators in terms of wavelet bases with compact support.[7,9]

In 1995, Beylkin and Keiser[8] reported on the application of the "fast" wavelet algorithms to the adaptive solution of nonlinear partial differential

equations where the sparse representation of operators was used to obtain algorithms with $O(N)$ complexity in the the wavelet coefficients. The Ph.D. thesis of Keiser[56] provides a detailed presentation of nonstandard operator representation and adaptive PDE solution strategies. Averbuch, Beylkin, et al.[2] (1995) addressed the solution of elliptic PDEs using the "fast" wavelet algorithms and nonstandard operator representation. Recently, Beylkin and Coult[11] (1998) have focused on multi-resolution methods for the solution of elliptic PDEs and eigenvalue problems.

1.3 Technical Issues

With the historical review of wavelets and PDEs in place, attention is turned to some of the technical issues involved in applying discrete solution techniques to PDEs. The accurate simulation of physical problems using grid-based numerical schemes for wave propagation, advection and diffusion hinges upon having a clear understanding of the constraining numerical errors, the requisite grid resolution to minimize such errors, and sufficient computational resources to effect solutions with the required grid scale. Examples of this may be seen when attempting to simulate wave propagation in an acoustic medium, or compute turbulent flow fields via direct numerical simulation (DNS) or large eddy simulation (LES).

In wave propagation (or pure advection), controlling the dispersive errors, i.e., phase and group velocity errors, to within 5% requires a minimum of 8 to 10 grid points per wavelength for most numerical methods. Thus, the computation of wave propagation problems is limited by the wavelength, or frequency, that the grid can accurately represent. A failure to respect the so-called Nyquist limit of the grid introduces deleterious aliasing effects that corrupt the fidelity of the simulation. Similarly, the calculation of turbulent flows via DNS and LES is limited by the range of length scales that the grid can accurately resolve. Simple turbulent channel flow requires a grid resolution approximately proportional to the square of the Reynolds number,[106] i.e., the attainable Reynolds number is limited by the resolving power of the grid. The application of graded meshes is appropriate in boundary layers or in regions of steep gradients (shocks) in compressible flow fields that are known a-priori. However, for problems with complex geometry and coupled physics, graded, unstructured meshes (or alternatively non-uniform particle distributions) are limited by the conservative estimates made for the

wavelengths that can be resolved.

In principle, the many variants of grid-based spatial adaptivity provide an alternative to the conservative approach described above. However, current approaches to adaptivity introduce many difficulties associated with unstructured grids, error estimates, and dynamic load balancing for parallel computations (particularly for distributed memory machines with large numbers of processors). In contrast, wavelets have the capability of decomposing solutions into a set of coefficients that depend upon scale and location, and have properties that enable the automatic detection of regions where the solution is non-smooth, i.e., built-in adaptivity. Wavelet bases for grid-based simulation have promised the capability to compute multi-scale solutions with potentially higher convergence rates than conventional finite difference and finite element methods. However, the application of wavelet bases to the grid-based solution of physical problems involving wave propagation, advection and diffusion is quite new, and there remain questions about the numerical and computational performance of this approach.

1.3.1 Numerical Performance

Numerical performance is a broad term, and is defined here to include the following: truncation error, consistency and stability, rate of convergence, dispersive character, and spatial adaptivity. At this point in time, the numerical performance of wavelet based methods, as defined here, has not been rigorously established, although there has been some preliminary work suggesting that the rate of convergence is comparable to both finite difference (FD) and finite element (FE) methods.[84]

In this effort, the evaluation of the numerical performance was initiated by attempting to collect baseline data for the performance of FD and FE methods on the suite of model problems representative of the three classes of problems of interest, i.e., wave propagation, advection and diffusion. Note that these problems have been selected because they constitute the primary components required to assemble more complicated solution methods for nonlinear problems such as high-rate Lagrangian deformation problems or high-Reynolds number, time-dependent, incompressible viscous flow.

Phase, group and amplitude errors constitute some of the most constraining numerical errors for simulating wave propagation and advection dominated flows. A reduction in the number of grid points per wavelength can provide a significant computational advantage and permit the exploration of

problems containing shorter wavelengths and higher frequencies, e.g., higher Reynolds numbers. An example of this has been demonstrated by Christon[19] where an optimized mass matrix leads to a factor of 4 reduction in the required 1-D grid resolution for acoustic wave propagation - a factor of 64 in 3-D. The promise of wavelets is to deliver an even greater advantage in terms of accuracy. However, the characterization of the dispersive errors for wavelet formulations is virtually nonexistent in the literature. Therefore, attention has been placed on characterizing the phase and group errors and their source. This is a necessary step in evaluating wavelet formulations in terms of accuracy, and ultimately assessing their grid resolution requirements.

1.3.2 Computational Performance

One of the goals for this effort was to develop the framework for applying wavelets to the computation of complex, multi-scale, multi-physics problems. The success of many computational strategies hinges upon the ability to treat high-resolution and non-uniform meshes, complicated geometry and coupled nonlinear physical phenomena in a computationally efficient fashion. Although the intrinsic adaptive nature of wavelet bases promises to relieve the need for increasingly high-resolution meshes, most of the existing wavelet formulations have not been assessed for their computational performance. Thus, this effort has also attempted to quantify the following: computational efficiency, sequential scaling (complexity), compatibility with FE (unstructured grid) data structures, and adaptivity. In addition, the methods selected for this study have been chosen based on the ability to exploit parallelism.

1.4 Overview

The subsequent chapters of this report consider the so-called DGHM multiwavelet element and the use of semi-orthogonal wavelets for solving elliptic partial differential equations. In Chapter 2, the development of a residual-based multi-level solution strategy that directly uses the wavelet basis and a discrete wavelet transform is presented. Chapter 3 presents the construction of wavelets that, by design, are semi-orthogonal with respect to the bilinear form of an elliptic operator. The use of the wavelet transform as a multi-scale preconditioner is also outlined in this chapter. The ideas of splitting finite element spaces are presented with the development of a multi-scale finite

element in Chapter 4. Finally, the numerical performance of the reproducing kernel method for hyperbolic and parabolic problems is addressed in Chapter 5. A summary of the exploratory research efforts and recommendations for further work are presented in Chapter 6.

Chapter 2

The DGHM Multi-wavelet

This chapter provides an overview of a finite element based on the DGHM (Donovan-Geronimo-Hardin-Massopust) multi-wavelets and the use of both the DGHM multi-scaling functions and the multi-wavelets in a Galerkin framework. The DGHM multi-wavelets are not new, and their use in solving elliptic partial differential equations has been investigated by Ko et al.[57] where the so-called AFIF element was considered. Here, we choose to refer to the AFIF element as the DGHM element to acknowledge the researchers that introduced the DGHM multi-wavelets. The theoretical development and background on the DGHM multi-wavelets may be found in the series of papers by Donovan et al.,[37] Geronimo et al.,[40] and Massopust.[76] The piecewise quadratic form of the multi-scaling functions with approximation order $p = 3$ was constructed by Roach[87] in the context of pre-filters for signal processing. Additional information on multi-wavelets may be found in the work by Strela,[90] Strela and Strang[92] and Plonka and Strela.[83]

In the work presented here, the choice to use the DGHM multi-wavelet was driven by the desire to have a basis with compact support while focusing on developing algorithms that make use of both the scaling functions and their associated wavelets. Here, both the linear (DGHM) and quadratic[87] forms of the multi-wavelets are considered. Figure 2.1 shows the linear DGHM multi-scaling and multi-wavelet functions at the element level and in an assembled form for two elements. In the element form, the multi-scaling functions exhibit some similarities to the quadratic finite element. That is to say, the DGHM multi-scaling functions looks like a fractal version of the quadratic finite element.

Before proceeding with a description of the multi-scale Galerkin solution

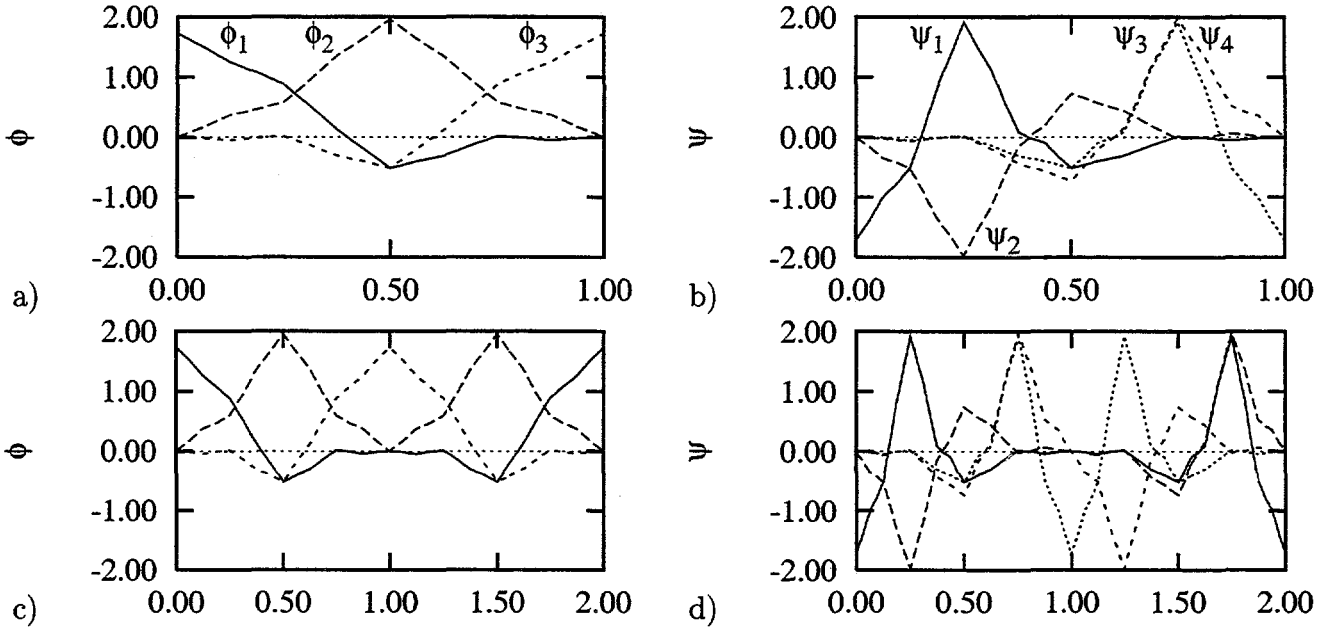

Figure 2.1: Donovan-Geronimo-Hardin-Massopust (DGHM) multi-wavelet element showing (a) the DGHM "shape" functions (ϕ), (b) the element view of the multi-wavelet shape functions (ψ), (c) an assembly of two DGHM multi-wavelet elements, and (d) the corresponding wavelets.

algorithm for elliptic partial differential equations, the mathematical framework for the Galerkin procedure is outlined in terms of the multi-scaling functions. A detailed description of the DGHM multi-wavelets is not presented here. The interested reader may refer to the work by Donovan, Geronimo and Massopust[37,40,76]

2.1 A Scaling Function Galerkin Formulation

Let Φ_k be a column vector containing all of the translations of a set of scaling functions supported in $\Omega \subset \mathbf{R}$ at scale k,

$$\Phi_k = \begin{bmatrix} \phi^1 \\ \phi^2 \\ \vdots \\ \phi^{M(k)} \end{bmatrix}, \tag{2.1}$$

where the length, $Ndof$, of Φ_k depends on the scale, k. Here, $Ndof$ indicates the number of degrees-of-freedom associated with scale k neglecting boundary degrees-of-freedom. This form of the scaling functions is somewhat inconsistent with equation (1.5), since here k is used to designate the "scale" and the vector of basis elements, Φ_k, corresponds to the collection of all the integer translates of the scaling functions at scale k. An assembly of two DGHM elements is shown in Figure 2.1c corresponding to $Ndof = 3$ and $k = 0$.

Given a differential operator $\mathcal{L}$ consider the boundary value problem

$$\begin{aligned} \mathcal{L}u &= f \text{ on } \Omega \\ u &= g \text{ on } \Gamma. \end{aligned} \tag{2.2}$$

Let the trial solution be in $\mathcal{V}_k$, i.e.

$$u_k = c_k^{0^T} \Phi_k. \tag{2.3}$$

In a Bubnov-Galerkin formulation with $\mathcal{V}_k$ being the test space, after integration by parts, the problem becomes

$$K_k^{\Phi\Phi} c_k^0 = F_k^{\Phi}, \tag{2.4}$$

where c_k^0 are the unknown coefficients at scale k.

For the model elliptic problem considered here, $\mathcal{L}u = -u''$, the condition number associated with the stiffness matrix, $K_k^{\Phi\Phi}$, grows as $O(h^{-2})$ for the finite elements as well as the multi-scaling function elements as shown in Table 2.1. Here, h is the node spacing, and the superscript "$\Phi\Phi$" on the operator K has been used to indicate that the scaling functions, Φ, have been used as both test and trial functions.

The condition numbers presented in Table 2.1 show that the initial condition number is approximately $2 - 6$ times worse for the multi-wavelet elements than the corresponding quadratic finite element. A precise reason for the degraded condition number relative to the finite elements at a given mesh resolution is not clearly understood, but it is thought to be related to the underlying fractal nature of these scaling functions.

It was shown by Donovan et al.[38] that the DGHM element based on multi-scaling functions has the same approximation order as the linear finite element, i.e., the approximation order is two. Massopust[76] showed that the rate of convergence of the DGHM scaling function element for a simple

Element	Linear FEM	Quadratic FEM	DGHM Multi-Wavelet	Quadratic Multi-Wavelet
Scale k	cond$(K_k^{\Phi\Phi})$	cond$(K_k^{\Phi\Phi})$	cond$(K_k^{\Phi\Phi})$	cond$(K_k^{\Phi\Phi})$
0	5.8	7.2	14.4	43.2
1	25.3	33.1	79.8	198.8
2	103.1	136.8	346.1	824.6
3	414.3	551.8	1413.2	3328.7
4	1659.4	2211.8	5681.9	13345.2

Table 2.1: Condition numbers of the stiffness matrix $K_k^{\Phi\Phi}$ at scale k for the linear and quadratic finite elements and DGHM multi-scaling function elements.

elliptic problem is the same as for the linear finite element. Therefore, ignoring the difficulties in performing numerical quadrature due to the fractal nature of the scaling functions, the DGHM element has a computational cost that is about the same as a quadratic finite element but the approximation properties of a linear finite element.

Using the wavelets

As suggested in the historical overview of wavelet-based PDE solution methods, few researchers have made use of the wavelet bases directly in the solution algorithm. In order to make use of the multi-wavelets, let Φ_k and Ψ_k be column vectors containing all of the translations of the scaling and wavelet functions supported in $\Omega \subset \mathbb{R}$ at scale k. Let $u_{k+1} := c_k^T \Phi_k + d_k^T \Psi_k$ where c_k and d_k are column vectors of the appropriate lengths. Implicit in this definition is the fact that multiple grid levels are being used – a coarse grid representation associated with scale k, and a finer grid associated with scale $k+1$. Given a differential operator, $\mathcal{L}$, consider the boundary value problem defined by equation (2.2). Let $< \cdot, \cdot >$ denote the $\mathbf{L}^2$ inner-product between $\mathbf{L}^2(\mathbb{R})$ functions. The Galerkin approximation for u_{k+1} is determined by

$$\begin{aligned} \left\langle \begin{bmatrix} \Phi_k \\ \Psi_k \end{bmatrix}, \mathcal{L}\left(\begin{bmatrix} c_k^T & d_k^T \end{bmatrix} \begin{bmatrix} \Phi_k \\ \Psi_k \end{bmatrix} \right) \right\rangle &= \left\langle \begin{bmatrix} \Phi_k \\ \Psi_k \end{bmatrix}, f \right\rangle \\ \left\langle \mathcal{L} \begin{bmatrix} \Phi_k \\ \Psi_k \end{bmatrix}, \begin{bmatrix} \Phi_k \\ \Psi_k \end{bmatrix} \right\rangle \begin{bmatrix} c_k \\ d_k \end{bmatrix} &= \begin{bmatrix} F_k^{\Phi} \\ F_k^{\Psi} \end{bmatrix}. \end{aligned} \tag{2.5}$$

After integration by parts, the matrix form of the two-scale formulation is

$$\begin{bmatrix} K_k^{\Phi\Phi} & K_k^{\Phi\Psi} \\ K_k^{\Psi\Phi} & K_k^{\Psi\Psi} \end{bmatrix} \begin{bmatrix} c_k \\ d_k \end{bmatrix} = \begin{bmatrix} F_k^{\Phi} \\ F_k^{\Psi} \end{bmatrix}, \tag{2.6}$$

where the operators $K_k^{\Phi\Phi}$, $K_k^{\Psi\Psi}$, and $K_k^{\Phi\Psi}$ are understood to contain weakened derivatives obtained by integration by parts.

In the subsequent algorithm development, the initial coarse-grid solution is chosen to be $c_k^0 := K_k^{\Phi\Phi^{-1}} F_k^{\Phi}$ with $d_k^0 = \mathbf{0}$ for convenience. With this convention it can be shown that

$$u_{k+1} := (c_{k+1}^0)^T \Phi_{k+1} = c_k^T \Phi_k + d_k^T \Psi_k. \tag{2.7}$$

To see this equivalence, recall that

$$\Phi_{k+1} = W_k \begin{bmatrix} \Phi_k \\ \Psi_k \end{bmatrix}, \tag{2.8}$$

where the wavelet transform is given by

$$W_k := [H_k \; G_k]. \tag{2.9}$$

For DGHM, the wavelet transform matrices are

$$H_1 = \frac{1}{20\sqrt{2}} \begin{bmatrix} 12 & -\sqrt{2} & 0 \\ 16\sqrt{2} & -6 & 0 \\ 12 & 9\sqrt{2} & 0 \\ 0 & 20 & 0 \\ 0 & 9\sqrt{2} & 12 \\ 0 & -6 & 16\sqrt{2} \\ 0 & -\sqrt{2} & 12 \end{bmatrix}, \tag{2.10}$$

$$G_1 = \frac{1}{20} \begin{bmatrix} -2 & -\sqrt{2} & -1 & 0 \\ -6\sqrt{2} & -6 & -3\sqrt{2} & 0 \\ 18 & 9\sqrt{2} & 9 & 0 \\ 0 & 0 & -10\sqrt{2} & 0 \\ 0 & -9\sqrt{2} & 9 & 18 \\ 0 & 6 & -3\sqrt{2} & -6\sqrt{2} \\ 0 & \sqrt{2} & -1 & -2 \end{bmatrix}. \tag{2.11}$$

The action of the wavelet transform is to act as a finite-domain convolution where H_k is essentially an averaging operator, and G_k is a "differencing" operator that accounts for detail in the function.

Proceeding with these definitions, the wavelet transform is used to develop the Galerkin formulation in terms of coarse-scale unknown coefficients, c_k, and wavelet coefficients, d_k. Beginning with the original problem,

$$\begin{aligned}
\mathcal{L}u_{k+1} &= f \\
\left\langle \Phi_{k+1}, \mathcal{L}(c^0_{k+1})^T \Phi_{k+1} \right\rangle &= \langle \Phi_{k+1}, f \rangle \\
\left\langle [H_k\ G_k] \begin{bmatrix} \Phi_k \\ \Psi_k \end{bmatrix}, \mathcal{L}\left((c^0_{k+1})^T [H_k\ G_k] \begin{bmatrix} \Phi_k \\ \Psi_k \end{bmatrix} \right) \right\rangle &= \left\langle [H_k\ G_k] \begin{bmatrix} \Phi_k \\ \Psi_k \end{bmatrix}, f \right\rangle \\
[H_k\ G_k] \left\langle \mathcal{L} \begin{bmatrix} \Phi_k \\ \Psi_k \end{bmatrix}, \begin{bmatrix} \Phi_k \\ \Psi_k \end{bmatrix} \right\rangle \begin{bmatrix} H^T_k \\ G^T_k \end{bmatrix} c^0_{k+1} &= [H_k\ G_k] \begin{bmatrix} F^\Phi_k \\ F^\Psi_k \end{bmatrix} \\
\begin{bmatrix} K^{\Phi\Phi}_k & K^{\Phi\Psi}_k \\ K^{\Psi\Phi}_k & K^{\Psi\Psi}_k \end{bmatrix} \begin{bmatrix} H^T_k \\ G^T_k \end{bmatrix} c^0_{k+1} &= \begin{bmatrix} F^\Phi_k \\ F^\Psi_k \end{bmatrix}. \qquad (2.12)
\end{aligned}$$

Therefore using equations (2.6) and (2.12) we have

$$c^0_{k+1} = \begin{bmatrix} H^T_k \\ G^T_k \end{bmatrix}^{-1} \begin{bmatrix} c_k \\ d_k \end{bmatrix}. \qquad (2.13)$$

Now because Φ and Ψ each form an orthonormal basis, H_k and G_k combine to form an orthogonal matrix, i.e. $(A^{-1} = A^T)$. Thus

$$c^0_{k+1} = [H_k\ G_k] \begin{bmatrix} c_k \\ d_k \end{bmatrix}. \qquad (2.14)$$

2.2 A Multi-Scale Algorithm

As we have seen, the Galerkin formulation just described leads to the following linear system,

$$\begin{bmatrix} K^{\Phi\Phi}_k & K^{\Phi\Psi}_k \\ K^{\Psi\Phi}_k & K^{\Psi\Psi}_k \end{bmatrix} \begin{bmatrix} c_k \\ d_k \end{bmatrix} = \begin{bmatrix} F^\Phi_k \\ F^\Psi_k \end{bmatrix}. \qquad (2.15)$$

Consider the individual discrete equations for c_k and d_k

$$K_k^{\Phi\Phi} c_k = F_k^{\Phi} - K_k^{\Phi\Psi} d_k \tag{2.16}$$
$$K_k^{\Psi\Psi} d_k = F_k^{\Psi} - K_k^{\Psi\Phi} c_k. \tag{2.17}$$

Remark 1 *Given any wavelet trial basis for the operator $\mathcal{L}u = -u''$, the two sparse block -Toeplitz matrices $K_k^{\Phi\Phi}$ and $K_k^{\Phi\Psi}$ have the property that*

$$T_k^{\Phi\Psi} := K_k^{\Phi\Phi^{-1}} K_k^{\Phi\Psi} \tag{2.18}$$

is also sparse block-Toeplitz. This property is true for the DGHM and the piecewise quadratic multi-wavelets and may be true for all wavelets.

Using the relation between the stiffness operators in equations (2.16) and (2.17),

$$c_k = c_k^0 - T_k^{\Phi\Psi} d_k, \tag{2.19}$$

where c_k^0 is the coarse-grid solution at scale k that is associated with the scaling functions. Thus, c_k is determined by reconstruction using c_k^0, d_k, and $T_k^{\Phi\Psi}$ which can be assembled in the finite element sense for any scale k. Substituting equation (2.19) into equation (2.17) yields

$$(K_k^{\Psi\Psi} - K_k^{\Psi\Phi} T_k^{\Phi\Psi}) d_k = F_k^{\Psi} - K_k^{\Psi\Phi} c_k^0. \tag{2.20}$$

Table 2.2 shows that, for the elliptic model problem, the matrix, $(K_k^{\Psi\Psi} - K_k^{\Psi\Phi} T_k^{\Phi\Psi})$, in equation (2.20) is well-conditioned for both the DGHM and piecewise-quadratic multi-wavelet elements. (The condition number of a matrix is the ratio of the largest to smallest eigenvalues and is used as a measure of the difficulty associated with solving the linear system involving the operator $K_k^{\Psi\Psi} - K_k^{\Psi\Phi} T_k^{\Phi\Psi}$.)

At this point the problem is reduced to solving for d_k using the well-conditioned system in (2.20). Numerous methods can be used, but for simplicity we will consider two stationary iterative methods, i.e., Jacobi and Gauss-Seidel.

The discussion of these methods begins with the following splitting

$$A_k = M_k - N_k, \tag{2.21}$$

where $A_k = (K_k^{\Psi\Psi} - K_k^{\Psi\Phi} T_k^{\Phi\Psi})$, and M_k is the diagonal (lower triangle) of A_k for the Jacobi (Gauss-Seidel) method. Applying this splitting to equation (2.21) yields

$$d_k = M_k^{-1}(N_k d_k + b_k), \tag{2.22}$$

Element	DGHM Multi-Wavelet	Quadratic Multi-Wavelet
Scale k	$\text{cond}(K_k^{\Psi\Psi} - K_k^{\Psi\Phi}T_k^{\Phi\Psi})$	$\text{cond}(K_k^{\Psi\Psi} - K_k^{\Psi\Phi}T_k^{\Phi\Psi})$
0	2.3533	5.5676
1	2.5497	5.7478
2	2.6057	5.7945
3	2.6201	5.8063
4	2.6238	5.8093

Table 2.2: Condition numbers for the matrix $(K_k^{\Psi\Psi} - K_k^{\Psi\Phi}T_k^{\Phi\Psi})$ for scale 0 through 4.

which will be used in the iteration process in the multi-scale algorithm described below.

Multi-Scale Algorithm

The multi-scale solution algorithm proceeds as follows.

1. Solve for the coarse-grid coefficients, $c_k^0 = K_k^{\Phi\Phi^{-1}}F_k^{\Phi}$ with $d_k^0 = \mathbf{0}$.

2. Use an iterative method (here, Jacobi or Gauss-Seidel) to find the wavelet coefficients, d_k^N.

$$d_k^{n+1} = M_k^{-1}(N_k d_k^n + b_k), \quad n = 1, \ldots, N.$$

3. Correct the coarse-grid coefficients using the wavelets.

$$c_k = c_k^0 - T_k^{\Phi\Psi} d_k^N.$$

4. Reconstruct the coefficients associated with the next higher-resolution grid using the wavelet transform, i.e.

$$c_{k+1}^0 = W_k \begin{bmatrix} c_k \\ d_k \end{bmatrix}.$$

5. Repeat 2-4 until the wavelet coefficients, d_k, are sufficiently small.

Although this example algorithm only explicitly refers to two scales, it is understood that multiple levels of grid resolution may be nested in the computation of the wavelet coefficients. That is to say, the computation of d_k implies that as many levels of grid resolution as are required are included in steps 2-4 in the multi-scale algorithm. It is also important to note that the matrices $M_k^{-1}, T_k^{\Phi\Psi}, N_k$, and W_k are all assembled matrices, reducing the algorithm to matrix-vector multiplications.

Example 3 *As an example application of the multi-scale algorithm, consider the differential equation*

$$-u''(x) = x(x - 5/4)(x - 2) \text{ on } [0, 2], \tag{2.23}$$

with essential boundary conditions

$$u(0) = u(2) = 0. \tag{2.24}$$

The solution to this problem is shown in Figure 2.2 at four scales (levels of grid resolution) with the exact solution.

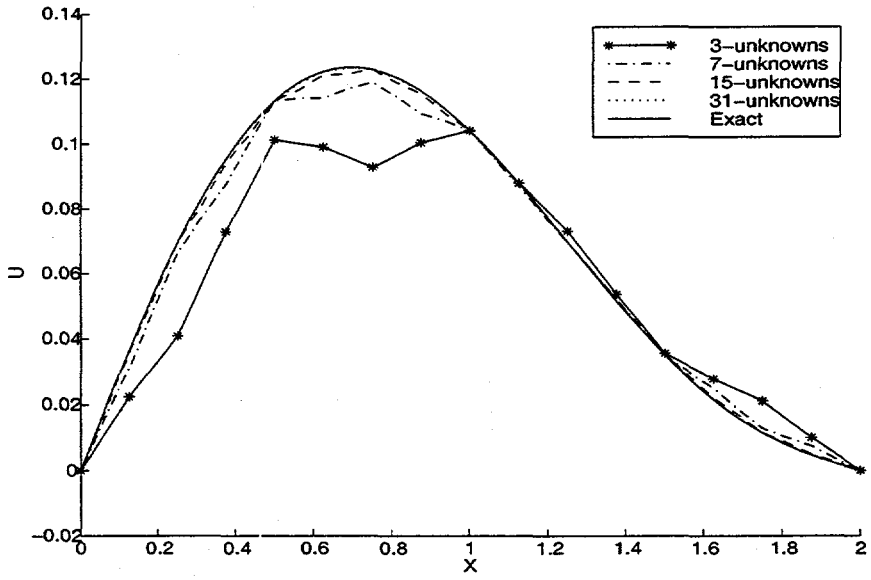

Figure 2.2: DGHM multi-wavelet multi-scale solution.

Table 2.3 shows the spectral radii for the Jacobi and Gauss-Seidel iteration matrices associated with the multi-wavelet elements for the model problem.

The spectral radii quickly asymptote, are bounded away from unity and remain constant with respect to increasing mesh resolution, i.e., increasing from scale 0 *to scale* 8 *corresponds to increasing the mesh resolution by a factor of* 256. *This result reinforces the idea that application of an iterative method to* $(K_k^{\Psi\Psi} - K_k^{\Psi\Phi}T_k^{\Phi\Psi})$ *is an appropriate choice for the development of efficient solution methods.*

	DGHM Multi-Wavelet Jacobi	Quadratic Multi-Wavelet Jacobi	DGHM Multi-Wavelet Gauss-Seidel	Quadratic Multi-Wavelet Gauss-Seidel
Scale k	$\rho(M_k^{-1}N_k)$	$\rho(M_k^{-1}N_k)$	$\rho(M_k^{-1}N_k)$	$\rho(M_k^{-1}N_k)$
0	0.135	0.575	0.018	0.306
1	0.135	0.581	0.018	0.329
2	0.135	0.582	0.018	0.340
3	0.135	0.582	0.018	0.343
4	0.135	0.582	0.018	0.344
5	0.135	0.582	0.018	0.344
6	0.135	0.582	0.018	0.344
7	0.135	0.582	0.018	0.344
8	0.135	0.582	0.018	0.344

Table 2.3: Spectral radii for for Jacobi and Gauss-Seidel iteration matrices associated with $A_k = (K_k^{\Psi\Psi} - K_k^{\Psi\Phi}T_k^{\Phi\Psi})$ for the DGHM and piecewise-quadratic elements.

In order to further evaluate the DGHM multi-wavelet element and the multi-scale algorithm the condition number associated with the generalized stiffness matrix was computed for both the multi-scaling functions and the multi-wavelets. The model problem considered is $-\epsilon u'' + u = f$ with $\epsilon \geq 0$, and $u(0) = u(L) = 0$. In the weak form, this problem becomes $M^{\Phi\Phi}U + K^{\Phi\Phi}U = F$ which introduces the mass matrix, $M^{\Phi\Phi}$ in addition to the stiffness.

Table 2.4 shows the condition numbers for both $\hat{K}^{\Phi\Phi} = [M^{\Phi\Phi} + K^{\Phi\Phi}]$ and $\hat{K}^{\Psi\Psi} = [M^{\Psi\Psi} + K^{\Psi\Psi}]$ after diagonal scaling for $0 \leq \epsilon \leq \infty$. Here, k indicates the scale with increasing k corresponding to increasing mesh resolution, i.e., $\Delta x = 2^{-(k+1)}$. As shown by the results, increasing the mesh resolution by a factor of 256 results in condition numbers that grow by 5 orders of magnitude

ϵ	0		1		10		10000		∞	
k	$\hat{K}^{\Phi\Phi}$	$\hat{K}^{\Psi\Psi}$	$\hat{K}^{\Phi\Phi}$	$\hat{K}^{\Psi\Psi}$	$\hat{K}^{\Phi\Phi}$	$\hat{K}^{\Psi\Psi}$	$\hat{K}^{\Phi\Phi}$	$\hat{K}^{\Psi\Psi}$	$\hat{K}^{\Phi\Phi}$	$\hat{K}^{\Psi\Psi}$
0	1	1	15	4	19	4	20	4	20	4
1	1	1	78	12	104	13	109	13	109	13
2	1	1	334	17	453	19	471	19	471	19
3	1	1	1355	24	1846	26	1922	26	1923	26
4	1	1	5441	29	7418	31	7727	31	7727	31
5	1	1	21785	33	29708	36	30945	36	30947	36
6	1	1	87160	40	118866	40	123819	40	123824	40
7	1	1	348662	44	475500	43	495311	43	495332	43
8	1	1	1394658	47	1902035	46	1981282	46	1981365	46

Table 2.4: Condition numbers for the diagonally scaled $\hat{K}^{\Phi\Phi}$ and $\hat{K}^{\Psi\Psi}$ operators for multiple mesh scales, $0 \leq k \leq 8$, and $0 \leq \epsilon \leq \infty$.

for $\hat{K}^{\Phi\Phi}$, while the condition numbers for $\hat{K}^{\Psi\Psi}$ increase by only a factor of 10 and appear to be approaching asymptotic values. Note that for small values of the parameter, ϵ, the eigenvalues associated with the mass matrix dominate in $\hat{K}^{\Phi\Phi}$ yielding condition numbers that are $O(1)$. In contrast, for finite values of ϵ, the eigenvalues of the stiffness matrix, $K^{\Phi\Phi}$ dominate and yield condition numbers for $\hat{K}^{\Phi\Phi}$ that grow as h^{-2}. In contrast, the condition numbers for $\hat{K}^{\Psi\Psi}$ are relatively well behaved independent of ϵ.

2.3 Numerical Performance

In this section, a brief digression is made in order to present a finite difference interpretation of the DGHM element. In addition, the dispersive behavior of the DGHM element is presented relative to the quadratic finite element.

2.3.1 A Finite Difference Interpretation

In order to gain a sense of what the DGHM element yields in terms of a finite difference discretization, the equivalent difference stencils for a centered approximation to u'' is presented here. In order to undo the Galerkin weighting introduced by the multiplication of the test functions, the procedure outlined by Gresho[46] (see pp. 52-53) is used for the linear, quadratic

and DGHM elements.

A cautionary warning is needed here because the use of a Taylor series, i.e., a finite difference, interpretation of the Galerkin discretizations can be misleading. As pointed out by Gresho[46] (and many others), the global finite element theory prevails over local Taylor series analyses. This point will be emphasized below with the quadratic element. The finite difference stencils presented below are simply intended to aid in the understanding and interpretation of the DGHM wavelet element.

In a Galerkin finite element setting, the element level mass, M^e, and stiffness, K^e, operators associated with the second order wave equation for the one-dimensional DGHM element are

$$M^e = \frac{d}{6}\begin{bmatrix} 1 & & \\ & 4 & \\ & & 1 \end{bmatrix}, \tag{2.25}$$

and

$$K^e = \frac{1}{21d}\begin{bmatrix} 85 & -128 & 43 \\ & 256 & -128 \\ sym. & & 85 \end{bmatrix}. \tag{2.26}$$

Here, $d = 2\Delta x$ is the element diameter in the grid, and Δx is the node spacing. A partition of unity scaling has been applied to the multi-scaling functions to obtain the "unit" mass and stiffness. Surprisingly, the element level mass matrix is identical to the row-sum lumped mass matrix for the quadratic finite element and is diagonal because the DGHM multi-wavelet scaling functions are orthogonal in $\mathbf{L}^2(\mathbb{R})$. In contrast, the stiffness in equation (2.26) differs somewhat from the stiffness for the quadratic element shown in Eq. (2.27) (see Belytschko and Mullen[4]).

$$K^e = \frac{1}{3d}\begin{bmatrix} 7 & -8 & 1 \\ & 16 & -8 \\ sym. & & 7 \end{bmatrix}. \tag{2.27}$$

Remark 2 *Despite the fractal nature of the DGHM multi-wavelet, the mass and stiffness entries can be calculated exactly for the one-dimensional DGHM element. This is accomplished by using the refinement equations associated with each scaling function. The recursion relation associated with the refinement equation provides a convenient way to solve for the moments, polynomial inner products, and in particular the mass and stiffness entries. For*

inner products with general functions, there is no exact calculation, but by conveniently representing the function of interest with a polynomial spline function a very good approximation to the inner product is obtained by using the exact polynomial inner product.

The local finite difference stencils are shown in Table 2.5 with the corresponding order of the local truncation error for each discretization scheme. In a finite difference sense, the second-order central difference scheme and the linear finite element yield identical difference stencils. Similarly, the center node for the quadratic finite element yields a difference stencil identical to the linear element and 3-point finite difference stencil. Interestingly, the edge node of the quadratic does not appear to yield the fourth-order 5-point finite difference stencil. However, Gresho[46] has demonstrated that this apparent result is in error and misleading since the global finite element theory leads to $O(\Delta x^3)$ estimates rather than the local estimates of $O(\Delta x^2)$ based on a Taylor series expansion.

The DGHM element yields center and edge node stencils that are similar in some respects to the quadratic element stencils. However, the leading fractional multiplier for each stencil is a result of the fractal nature of the basis functions. Although it would be natural to suspect that the global finite element theory would show that the DGHM element, like the quadratic element, yields an $O(\Delta x^3)$ approximation, Massopust[76] has demonstrated that the DGHM element delivers accuracy no better than the linear finite element, i.e., $O(\Delta x^2)$. This is due to the fact that the DGHM multi-scaling functions can only represent functions comprised of $\{1, x\}$, unlike the quadratic element that can represent $\{1, x, x^2\}$. Thus, the DGHM element is a quadratic-like element, with the concomitant computational cost of a quadratic element, that performs like a linear element!

2.3.2 Dispersive Behavior

Attention is now turned to the question of numerical dispersion. For this discussion, the model problem under consideration is the second-order wave equation in Cartesian coordinates,

$$\frac{\partial^2 u}{\partial t^2} - c^2 \frac{\partial^2 u}{\partial x^2} = 0. \tag{2.28}$$

Because of the similarities to the quadratic element, the dispersion results for the DGHM element are compared to those for the quadratic element.

Remark 3 *The hierarchical nature of the DGHM wavelet-Galerkin formulation permits multi-scale solution strategies to be formulated. However, for the purposes of numerical analysis, only the scaling functions need to be considered because the total, solution is considered to be represented in terms of the scaling functions at the finest scale, i.e., at the highest mesh resolution. Thus, the operators based only on the scaling functions are sufficient for a von Neumann analysis.*

The details of the von Neumann analysis are omitted here, but follow the analysis performed by Belytschko and Mullen[4] for the quadratic element. A detailed introduction to dispersion analysis is also presented in Chapter 5. The semi-discrete Galerkin form of the second-order wave equations is

$$\mathbf{M}\ddot{\mathbf{U}} + \mathbf{K}\mathbf{U} = 0, \tag{2.29}$$

where $\mathbf{M}$ is the mass matrix, $\mathbf{K}$ is the stiffness matrix, and $\mathbf{U}$ are the unknown coefficients.

The non-dimensional frequency, $\omega\Delta x/c$, for the DGHM wavelet element is shown in Figure 2.3 with the frequency spectra for the quadratic finite element. Here, c is the sonic velocity, Δx the grid spacing, and λ the wavelength. The frequency response for each element admits two solutions, the so-called optical and acoustical branches. The gap between the branches of the frequency response is often referred to as a "stopping" band. The similarities between the spectra for the DGHM and quadratic elements suggests that the dispersive nature of the DGHM element will be somewhat worse than the quadratic element, due in part to the lack of spatial coupling of time-derivatives associated with the diagonal mass matrix.

An alternative view of the dispersion error may be seen in Figure 2.4 which shows the non-dimensional phase speed, i.e., the discrete or apparent sound speed normalized by the true sound speed. Here, only the "acoustic" branch from the dispersion relations is shown, and there is clearly significant leading phase error in the mid-range of the spectrum relative to the acoustic branch for the quadratic element.

2.4 Summary

In this chapter, the Donovan-Geronimo-Hardin-Massopust (DGHM) multi-wavelets were used to develop a multi-level solution algorithm in which both

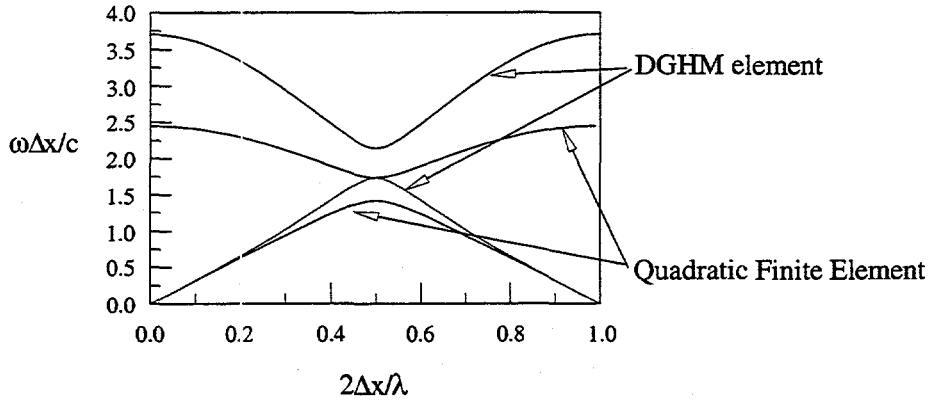

Figure 2.3: Non-dimensional circular frequency for the quadratic finite element and the DGHM multi-wavelet element.

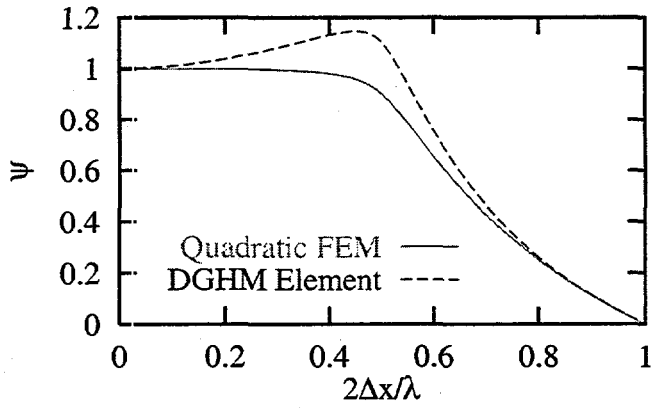

Figure 2.4: Non-dimensional phase speed for the quadratic finite element and the DGHM multi-wavelet element.

the multi-scaling functions and the multi-wavelets are used directly in the solution procedure. However, the DGHM wavelet element is inferior to the quadratic finite element in terms of its numerical performance because the element has the computational cost of a quadratic element, the convergence properties of a linear element, and inferior dispersive characteristics. Although the DGHM element is not appropriate for use in applications, it has been useful in developing the concepts for multi-level solution algorithms in terms of a true wavelet basis. These concepts are expanded in the subsequent chapters.

Stencil	Truncation Error
FDM – Centered 3 Point $\frac{1}{\Delta x^2}(u_{i-1} - 2u_i + u_{i+1})$	$O(\Delta x^2)$
FDM – Centered 5 Point $\frac{1}{12\Delta x^2}(u_{i-2} - 16u_{i-1} + 30u_i - 16u_{i+1} + u_{i+2})$	$O(\Delta x^4)$
FEM – Linear $\frac{1}{\Delta x^2}(u_{i-1} - 2u_i + u_{i+1})$	$O(\Delta x^2)$
FEM – Quadratic (center node) $\frac{1}{\Delta x^2}(u_{i-1} - 2u_i + u_{i+1})$	$O(\Delta x^2)$
FEM – Quadratic (edge node) $\frac{1}{4\Delta x^2}(-u_{i-2} + 8u_{i-1} - 14u_i + 8u_{i+1} - u_{i+2})$	$O(\Delta x^2)$
DGHM – Center Node $\frac{10}{7\Delta x^2}(u_{i-1} - 2u_i + u_{i-1})$	$O(\Delta x^2)$
DGHM – Edge Node $\frac{2}{49\Delta x^2}(-2u_{i-2} + 25u_{i-1} - 46u_i + 25u_{i+1} - 2u_{i+2})$	$O(\Delta x^2)$

Table 2.5: Finite difference stencils and leading order of truncation error for u''.

Chapter 3

The "Semi-hat" Basis

In this chapter, we present a construction of wavelets that are (a) semi-orthogonal with respect to an arbitrary elliptic bilinear form $a(\cdot,\cdot)$ on the Sobolev space $H_0^1(0,L)$ and (b) continuous and piecewise linear on an arbitrary discretization of $[0,L]$. Here, semi-orthogonal is understood to indicate orthogonality of the wavelets between multiple scales with respect to the bilinear form, i.e., $a(\psi(2^k\cdot),\psi(2^j\cdot)) = 0$ for $k \neq j$. We illustrate this construction using the model problem

$$\begin{aligned} -\epsilon^2 u'' + u &= f \\ u(0) = u(L) &= 0. \end{aligned}$$

We also construct a-orthogonal Battle-Lemarié type wavelets that fully diagonalize the Galerkin discretized matrix for the model problem with domain $\mathbb{R}$.

Finally, we describe a hybrid basis consisting of a combination of elements from the semi-orthogonal wavelet basis and a hierarchical Schauder basis. Numerical experiments indicate that this basis leads to robust, scalable Galerkin discretizations of the model problem that remain well-conditioned independent of ϵ, L, and the refinement level K.

3.1 Introduction

In this section, we review some basic theory about Galerkin discretizations of elliptic variational problems and their relationship to the Riesz bounds of the underlying basis (cf. Cohmas and Masson,[21] Dahmen[26]).

Let $\mathcal{H}$ be a Hilbert space with inner product $\langle \cdot, \cdot \rangle_{\mathcal{H}}$. Let $a(\cdot, \cdot)$ be a symmetric coercive continuous bilinear form on $\mathcal{H}$, that is, a is a symmetric bilinear form such that

$$C\|v\|_{\mathcal{H}}^2 \leq a(v, v) \leq D\|v\|_{\mathcal{H}}^2$$

for some positive constants C and D. Let $\|\cdot\|_E := \sqrt{a(\cdot, \cdot)}$ is the energy norm generated by a. The coercivity and continuity of a imply that the energy norm is equivalent to the norm associated with $\mathcal{H}$.

Let $\mathcal{H}'$ ($\cong \mathcal{H}$) denote the dual of $\mathcal{H}$. Consider the elliptic variational problem:

$$\begin{aligned} &\text{Given } F \in \mathcal{H}', \text{ find } u \in \mathcal{H} \text{ such that} \\ &\quad a(u, v) = F(v), \quad \forall v \in \mathcal{H}. \end{aligned} \tag{3.1}$$

Let $\mathcal{V}$ be a finite dimensional subspace of $\mathcal{H}$. Then the Galerkin approximate solution $u_{\mathcal{V}}$ is the unique solution of (3.1) with $\mathcal{H}$ replaced by $\mathcal{V}$. Let $\Phi = (\phi^1, \ldots, \phi^N)^T$ be a basis for $\mathcal{V}$. (Throughout this paper, a basis will be arranged as a column vector.) Then $u_{\mathcal{V}} = c^T\Phi$ can be found by solving the linear system

$$a(\Phi, \Phi)c = F(\Phi), \tag{3.2}$$

where $a(\Phi, \Phi)$ is the $N \times N$ matrix $(a(\phi^i, \phi^j))$ and $F(\Phi)$ is the column vector $(F(\phi^1), \ldots, F(\phi^N))^T$.

For large N, it is usually impractical to solve the linear system (3.2) using direct solution methods. When the matrix $A^\Phi := a(\Phi, \Phi)$ is well-conditioned, the system can be efficiently solved using iterative methods. We say that $\underline{\alpha}$ (respectively $\overline{\alpha}$) is a lower (upper) Riesz bound for the basis Φ with respect to $\|\cdot\|_E$ if

$$\underline{\alpha}\, c^T c \leq \|c^T\Phi\|_E^2 \leq \overline{\alpha}\, c^T c. \tag{3.3}$$

Define $\underline{\alpha}_\Phi$ ($\overline{\alpha}_\Phi$) to be the largest (smallest) lower (upper) Riesz bound for Φ with respect to $\|\cdot\|_E$. Observe that

$$\|c^T\Phi\|_E^2 = c^T A^\Phi c.$$

Since A^Φ is symmetric and positive definite we have

$$\begin{aligned} \|A^\Phi\|_2 &= \max_c \frac{c^T A^\Phi c}{c^T c} = \overline{\alpha}_\Phi \\ \|(A^\Phi)^{-1}\|_2^{-1} &= \min_c \frac{c^T A^\Phi c}{c^T c} = \underline{\alpha}_\Phi. \end{aligned}$$

Therefore, the condition number of A^Φ, $\text{cond}(A^\Phi)$, is related to the Riesz bounds for Φ in the following way:

$$\text{cond}(A^\Phi) = \overline{\alpha}_\Phi / \underline{\alpha}_\Phi. \tag{3.4}$$

Suppose Ψ is another basis for $\mathcal{V}$ and suppose W is the nonsingular $N \times N$ matrix such that

$$\Psi = W^T \Phi.$$

Then defining $u_\mathcal{V} = d^T \Psi$, d may be found by solving

$$a(\Psi, \Psi) d = F(\Psi). \tag{3.5}$$

Note that

$$A^\Psi = a(\Psi, \Psi) = W^T a(\Phi, \Phi) W. \tag{3.6}$$

Thus the linear system (3.5) resulting from (3.2) by a change of basis can also be considered to arise from (3.2) by preconditioning with W.

3.2 Multi-Scale Transformations

As demonstrated in Chapter 2, the wavelet transform plays a key role in multi-scale solution algorithms. Given that

$$\mathcal{V}_0 \subset \mathcal{V}_1 \subset \cdots \subset \mathcal{V}_k \subset \cdots$$

is a one-sided sequence of nested finite-dimensional subspaces of $\mathcal{H}$ such that $\overline{\bigcup \mathcal{V}_k} = \mathcal{H}$. Define $\mathcal{W}_0 := \mathcal{V}_0$ and, for $k \geq 1$, choose $\mathcal{W}_k$ in $\mathcal{V}_k$ so that

$$\mathcal{V}_k = \mathcal{V}_{k-1} \oplus \mathcal{W}_k \tag{3.7}$$

where $\oplus$ denotes the direct sum. (Note that here, the direct sum is not an orthogonal direct sum). Let Φ_k be a basis for $\mathcal{V}_k$ and let ψ_k be a basis for $\mathcal{W}_k$ (we choose $\psi_0 = \Phi_0$). Then

$$\Psi_k := \begin{pmatrix} \psi_0 \\ \vdots \\ \psi_k \end{pmatrix}$$

is also a basis for $\mathcal{V}_k$. Let W_k be the multi-scale transformation such that

$$\Psi_k = W_k^T \Phi_k,$$

and let T_k be the two-scale transformation such that

$$\begin{pmatrix} \Phi_{k-1} \\ \psi_k \end{pmatrix} = T_k^T \Phi_k.$$

Observe that

$$W_k = T_k \begin{pmatrix} T_{k-1} & 0 \\ 0 & I_{k-1} \end{pmatrix} \cdots \begin{pmatrix} T_1 & 0 \\ 0 & I_1 \end{pmatrix}$$

where I_k is the $n \times n$ identity matrix with $n = \dim(\mathcal{V}_k)$.

Fix K and let $\Psi = \Psi_K$, $\Phi = \Phi_K$, and $W = W_K$. We assume that (a) multiplication by W can be implemented with a fast algorithm (this is the case for compactly supported wavelet bases), (b) A^Ψ is well-conditioned, and (c) $F(\Phi)$ can be easily approximated. Algorithm A summarizes the solution of the discretized problem given in (3.2) using the multi-scale transform W.

Algorithm A:

- Approximate F^Φ.
- Calculate $F^\Psi = W^T F^\Phi$.
- Solve $A^\Psi d = F^\Psi$.
- $c = Wd$.

One very important aspect of this algorithm is that it does not use the decomposition matrix W^{-1}. This is significant because it permits the relaxation of strict orthogonality in the construction of the wavelet basis.

3.3 Wavelet Construction

Let $(X_k)_{k \geq 0}$ be a given sequence of nested knot sequences on $[0, 1]$ (i.e., a series of logically ordered and nested grids) satisfying

- $X_k = (x_k^j)_{0 \leq j \leq N_k}$
- $0 = x_k^0 < \cdots < x_k^j < \cdots < x_k^{N_k} = L$

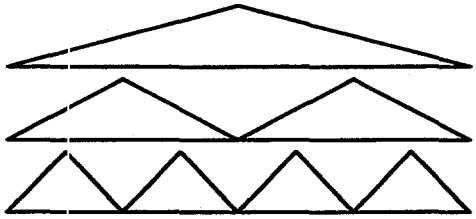

Figure 3.1: Schauder basis $\Psi_2 = (\psi_0^T \quad \psi_1^T \quad \psi_2^T)^T$ with dimension 7 on a uniform discretization.

- $x_{k+1}^{2j} = x_k^j$

Let ϕ_k^j be the piecewise linear continuous function associated with knot sequence X_k such that $\phi_k^j(x_k^{j'}) = \delta_{j,j'}$. If $\Phi_k = (\phi_k^1, \ldots, \phi_k^{N_k-1})^T$, then Φ_k is a nodal basis for $\mathcal{V}_k$ that is the usual finite element space of piecewise linear continuous functions on $[0, L]$ with knot sequence X_k.

We next describe two choices for $\mathcal{W}_k$.

3.3.1 Hierarchical Schauder Basis

One simple choice for $\mathcal{W}_k$ satisfying (3.7) is the well known Schauder basis[27,110,112]

$$\psi_k^j := \phi_k^{2j-1}, \quad j = 1, \ldots, N_k$$

illustrated in Figure 3.1.

Next we construct the two-scale transformation for the Schauder basis. Denote the length of the subinterval $[x_k^{j-1}, x_k^j]$ by

$$\Delta_k^j := x_k^j - x_k^{j-1}.$$

The function values $h_k^{j,j'}$ and $g_k^{j,j'}$ for ϕ_{k-1}^j and ψ_k^j respectively at the knot

(grid point) $x_k^{j'}$ are given by

$$h_k^{j,j'} = \begin{cases} \frac{\Delta_k^{j'}}{\Delta_{k-1}^{j}}, & j' = 2j-1 \\ 1, & j' = 2j \\ \frac{\Delta_k^{j'+1}}{\Delta_{k-1}^{j}}, & j' = 2j+1 \\ 0, & \text{otherwise} \end{cases}$$

$$g_k^{j,j'} = \delta_{j',2j-1}.$$

Then

$$\phi_{k-1}^{j} = \sum_{j'} h_k^{j,j'} \phi_k^{j'}$$

$$\psi_k^{j} = \sum_{j'} g_k^{j,j'} \phi_k^{j'}.$$

Now let H_k be the $(N_k - 1) \times (N_{k-1} - 1)$ matrix $H_k = (h_k^{j,j'})_{j',j}$ and let G_k be the $(N_k - 1) \times (N_{k-1})$ matrix $G_k = (g_k^{j,j'})_{j',j}$. Thus, the two-scale transformation for the Schauder basis is given by

$$T_k = (H_k \;\; G_k).$$

3.3.2 Semi-Orthogonal Sombrero Wavelets

Here we choose $\mathcal{W}_k$ to be the orthogonal complement of $\mathcal{V}_{k-1}$ in $\mathcal{V}_k$ with respect to the scalar product $a(\cdot,\cdot)$, that is

$$\mathcal{W}_k := \mathcal{V}_k \cap \mathcal{V}_{k-1}^{\perp_a}.$$

Regardless of the choice of basis ψ_k for $\mathcal{W}_k$, the matrix A^{Ψ_k} is then decoupled between grid levels so that it is a block diagonal matrix:

$$A^{\Psi_k} = \text{diag}(A^{\psi_0}, A^{\psi_1}, \ldots, A^{\psi_k}).$$

We next give a procedure for constructing a local basis of wavelets for $\mathcal{W}_k$. Let

$$B := B(k) = a(\Phi_{k-1}, \Phi_k)$$

where we suppress the k dependence when the choice for k is unambiguous. Note that

$$\mathcal{W}_k = \{g^T \Phi_k \mid g \in \ker B\}.$$

We will use certain sub-blocks of B in our construction. To this end we define R_{i_1,i_2} to be the $(i_2 - i_1 + 1) \times (N_k - 1)$ matrix whose i-th row is the $(i - i_1 + 1)$-th row of the $(N_k - 1) \times (N_k - 1)$ identity matrix. Then the $[i_1, i_2] \times [j_1, j_2]$ block of B is given by

$$B^{i_1,i_2}_{j_1,j_2} := R_{i_1,i_2} B R^T_{j_1,j_2}.$$

Let

$$C_n := \begin{cases} B^{1,n}_{1,2n-1} & \text{for } n = 2, 3 \\ B^{n-3,n}_{2n-5,2n-1} & \text{for } 3 \leq n \leq N_{k-1} - 1 \\ B^{n-3,n-1}_{2n-5,2n-1} & \text{for } n = N_{k-1} \end{cases}$$

For $4 \leq n < N_{k-1}$, the matrix C_n is a 4×5 matrix that generically has a kernel of dimension one. This kernel then corresponds to a wavelet with support contained in $[x_k^{2n-6}, x_k^{2n}] = [x_{k-1}^{n-3}, x_{k-1}^{n}]$. More generally, we define the following procedure for constructing a local basis for $\mathcal{W}_k$.

Let $K_n := \ker(C_n)$ and, for $n \geq 3$, let K_n^0 denote the subspace of K_n consisting of the elements in $w \in K_n$ whose last two components are both zero. In the generic case, K_n^0 is the trivial subspace. Let

$$\Phi_k^n := \begin{cases} (\phi_k^1, \phi_k^2, \phi_k^3)^T, & n = 2 \\ (\phi_k^{2n-5}, \ldots, \phi_k^{2n-1})^T, & 3 \leq n \leq N_{k-1}. \end{cases} \tag{3.8}$$

Algorithm B:

- Let w_3 denote a basis for C_3 and set $\psi_k^3 = \{w^T \Phi_k^3 \mid w \in w_3\}$.

- For $n = 3, \ldots, N_{k-1}$, do
  - Choose K_n^1 so that $K_n = K_n^0 \oplus K_n^1$ and choose a basis w_n for K_n^1.
  - Set $\psi_k^n = \{w^T \Phi_k^n \mid w \in w_n\}$.

- $\psi_k = \bigcup_{n=3}^{N_{k-1}} \psi_k^n$.

We next give a sufficient condition that the above procedure produces a basis for $\mathcal{W}_k$. For $4 \leq n < N_{k-1}$, we note that C_n has the following block form

$$C_n = \begin{pmatrix} D_n & E_n \\ 0 & F_n \end{pmatrix} \tag{3.9}$$

where D_n is 3×3, E_n is 3×2, and F_n is 1×2.

Lemma 3.3.1 *Let ψ_k be the set produced by Algorithm B. Suppose*

$$\text{range } D_n \supset E_n(\ker F_n) \quad (4 \leq n \leq N_{k-1}). \tag{3.10}$$

Then ψ_k is a basis for $\mathcal{W}_k := \mathcal{V}_k \cap \mathcal{V}_{k-1}^{\perp_a}$.

Proof:
Let $S^{n_1,n_2} := \{f \in W_k \mid \text{ supp}(f) \subset [x_k^{2n_1}, x_k^{2n_2}]\}$. Let $B_n := B_{1,2n-1}^{1,n}$. Note that $f \in S^{0,n}$ if and only if $f = y^T(\phi_k^1, \ldots, \phi_k^{2n-1})^T$ for some $y \in \ker B_n$ and that $f \in S^{n-3,n}$ if and only if $f = y^T \Phi_k^n$ for some $y \in \ker C_n$. Hence, the proof will be complete if we can show that

$$S^{0,n} = S^{0,n-1} + S^{n-3,n}, \qquad (4 \leq n \leq N_{k-1}). \tag{3.11}$$

Observe that

$$B_n = \begin{pmatrix} B_{n-1} & E_n \\ 0 & F_n \end{pmatrix} \tag{3.12}$$

for $n \geq 4$.

Suppose $v \in \ker F_n$, then by (3.10) there is some $u \in \ker C_n$ such that $(u^4, u^5)^T = v$. Suppose $y \in \ker B_n$. From (3.12) it is clear that $w := (y_{2n-2}, y_{2n-1})^T \in \ker F_n$ and hence there is some $u \in \ker C_n$ such that the last two components of y agree with the last two components of u. We then obtain

$$\ker B_n = P_1(\ker B_{n-1}) + P_2(\ker C_n) \tag{3.13}$$

where P_1 is the padding operator that takes a vector v of length $2n-3$ to one of length $2n-1$ by appending two zeros to v and P_2 is the padding operator that takes a vector v of length 5 to one of length $2n-1$ by prepending $2n-6$ zeros to v.

Then (3.11) follows from (3.13) and the proof is complete. ■

An example is shown in Figure 3.2 for a non-uniform discretization with an arbitrary refinement.

3.4 Uniform Discretization

In this section we give the construction of piecewise-linear wavelets on a uniform discretization that are semi-orthogonal with respect to the bilinear form associated with the following model problem:

$$\begin{aligned} -\epsilon^2 u'' + u &= f \\ u(0) = u(L) &= 0. \end{aligned} \tag{3.14}$$

Let $\langle \cdot, \cdot \rangle$ be the usual inner product on $L_2([0, L])$ and let $\mathcal{H}$ be the Sobolev space $\mathcal{H}_0^1((0, L))$ for some $L \in \mathbb{R}^+$. We assume f is such that $F := \langle f, \cdot \rangle$ is in $\mathcal{H}'$. Then the weak formulation becomes: Find $u \in \mathcal{H}$ so that

$$a(u, v) := \epsilon^2 \langle u', v' \rangle + \langle u, v \rangle = \langle f, v \rangle \quad \forall v \in \mathcal{H}. \tag{3.15}$$

Moreover, suppose (X_k) is a uniform discretization of $[0, L]$. In order to avoid special cases associated with boundary wavelets, we let $L = 4$ and $N_0 = 4$:

$$x_k^j = \frac{j}{2^k}, \quad j = 0, \ldots, N_k = 2^k L.$$

Let $\phi(x) = (1 - |x - 1|)$ and define

$$\phi_k^j := 2^{k/2} \phi(2^k \cdot - j).$$

(Here we have chosen a different normalization of ϕ_k^j than the normalization used in the non-uniform case.) Then

$$\phi_k^j = \sum_{l=-1}^{1} h_l \phi_{k+1}^{j-l}$$

where $h_{-1} = h_1 = \frac{1}{2\sqrt{2}}$, and $h_0 = \frac{1}{\sqrt{2}}$.

As in the previous section, let Φ_k^n be defined by (3.8). Because of the differentiation in the scalar product a, the ϵ in the model problem is scaled differently at each level resulting in a level dependent parameter ϵ_k given by

$$\epsilon_k := 2^k \epsilon.$$

In this case, C_n is independent of $4 \leq n \leq N_{k-1} - 1$ and its kernel is the space spanned by the vector

$$w = (24\epsilon_k^2 - 1, 6, 48\epsilon_k^2 - 10, 6, 24\epsilon_k^2 - 1)^T \tag{3.16}$$

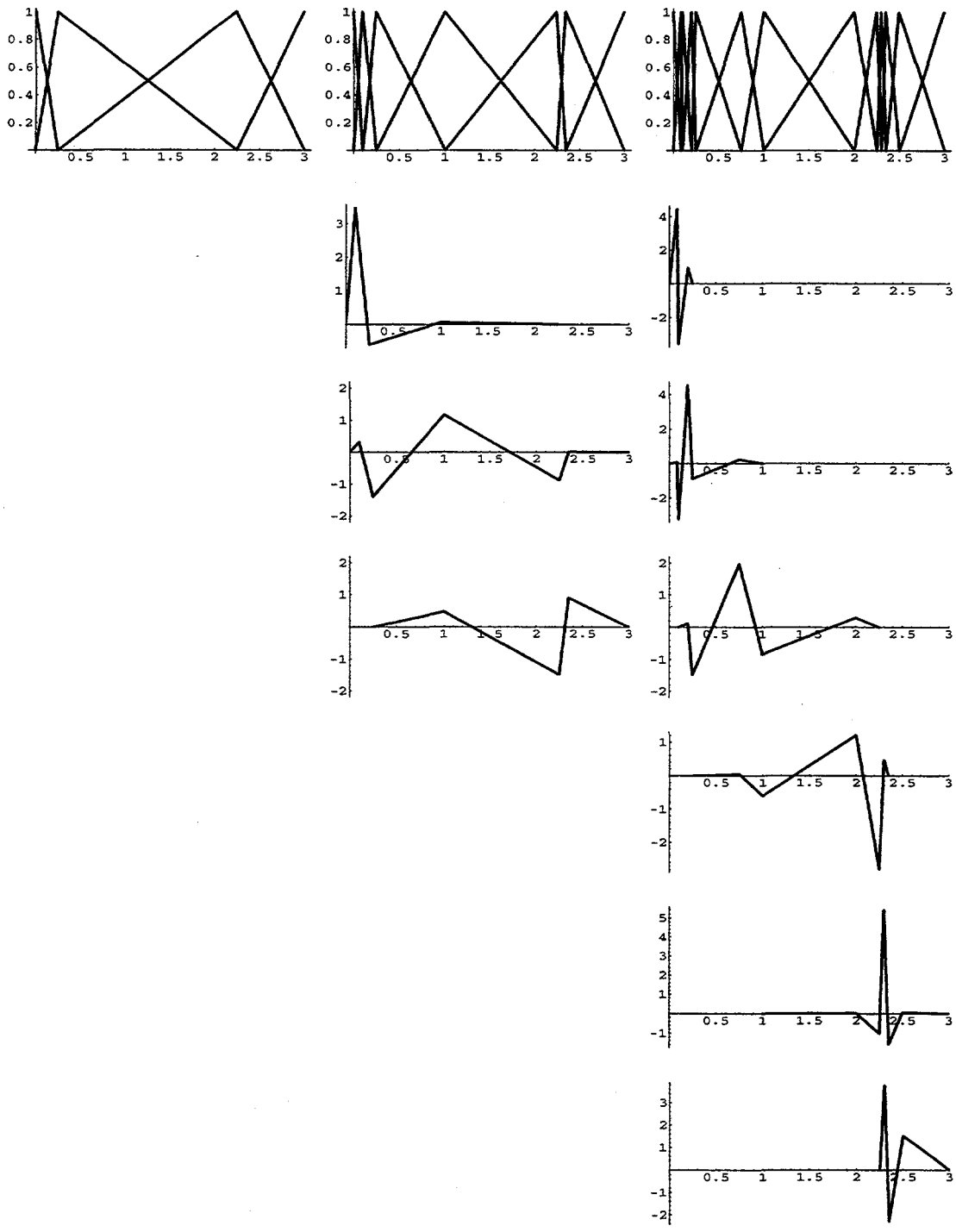

Figure 3.2: $\mathcal{V}_0$, $\mathcal{V}_1 \oplus \mathcal{W}_1$, and $\mathcal{V}_2 \oplus \mathcal{W}_2$ bases respectively for the semi-orthogonal wavelets with a non-uniform discretization and arbitrary refinement.

The kernel of C_3 (respectively, $C_{N_{k-1}}$) contains w plus an additional vector w_L (respectively, w_R) given below:

$$w_L = (9 + 72\epsilon_k^2, -6, 1 - 24\epsilon_k^2, 0, 0)^T$$

and

$$w_R = (0, 0, 1 - 24\epsilon_k^2, -6, 9 + 72\epsilon_k^2)^T.$$

Then we let $\psi_k^1 = w_L^T \Phi_k^3$, $\psi_k^j = w^T \Phi_k^{j+1}$ for $2 \le j \le N_{k-1} - 1$ and $\psi_k^{N_{k-1}} = w_R^T \Phi_k^{N_{k-1}}$.

The wavelet ψ is shown in Figure 3.3 for $0 \le \epsilon \le 3$. Another more general construction of semi-orthogonal wavelets on a uniform grid using Fourier techniques was given in[24,25] that includes these wavelets.

3.4.1 Unbounded Domain: Riesz bounds and Battle-Lemarié Type Wavelets

We next consider the simpler choice of domain $\mathbb{R}$. In this case we can calculate the Riesz bounds for the wavelet bases ψ_k for $\mathcal{W}_k$ using Fourier transform techniques. For $\theta \in L_2(\mathbb{R})$ we define the Grammian symbol E_θ (with respect to the scalar product $a(\cdot,\cdot)$) by

$$E_\theta(\omega) = \frac{1}{2\pi} \sum_{n \in \mathbb{Z}} a(\theta, \theta(\cdot - n)) e^{in\omega} \tag{3.17}$$

It is a standard result (see,[36] for example) that the Riesz bounds $\underline{\alpha}_\Theta$ and $\overline{\alpha}_\Theta$ for the infinite basis $\Theta = (\theta(\cdot - n))_{n \in \mathbb{Z}}$ with respect to $a(\cdot,\cdot)$ are equal to the essential infimum and essential supremum of E_Θ, respectively. The L_2-condition number of the infinite matrix (A^Θ) is then the ratio $\overline{\alpha}_\Theta / \underline{\alpha}_\Theta$.

In the case of our model problem with the sombrero wavelets ψ_k we get

$$E_{\psi_k}(\omega) = \alpha_0 + 2\alpha_1 \cos(w) + 2\alpha_2 \cos(2w)$$

where

$$\begin{aligned} \alpha_0 &= 12(3 + 122\epsilon_k^2 + 480\epsilon_k^4 + 1152\epsilon_k^6) \\ \alpha_1 &= 20/3 + 384\epsilon_k^2 - 2304\epsilon_k^4 - 9216\epsilon_k^6 \\ \alpha_2 &= (2/3)(1 - 24\epsilon_k^2)^2(-1 + 6\epsilon_k^2). \end{aligned}$$

It is an elementary, but tedious, exercise to verify that

$$\frac{\max_\omega E_{\psi_k}(\omega)}{\min_\omega E_{\psi_k}(\omega)} = \begin{cases} 4\frac{(1+12\epsilon_k^2)^3}{9+432\epsilon_k^2} & \text{for } 0 \le \epsilon_k \le 0.33 \\ 4\frac{9+432\epsilon_k^2}{(1+12\epsilon_k^2)^3} & \text{for } 0.36 \le \epsilon_k < \infty \end{cases}$$

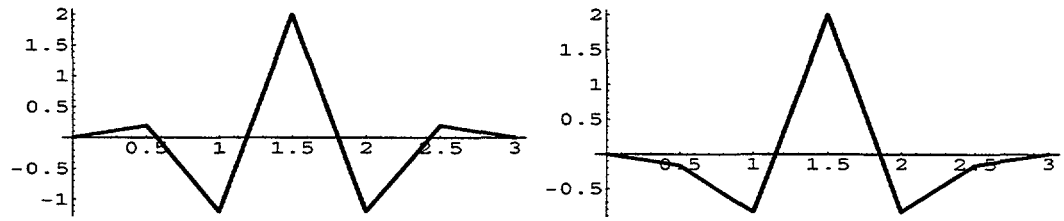

a)

b)

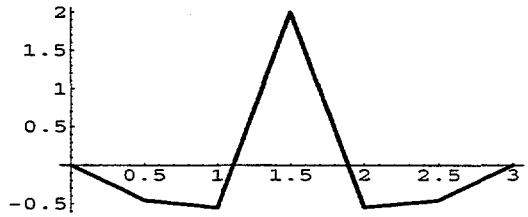

c)

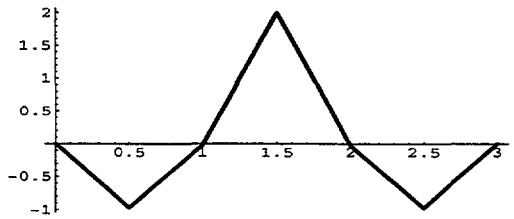

d)

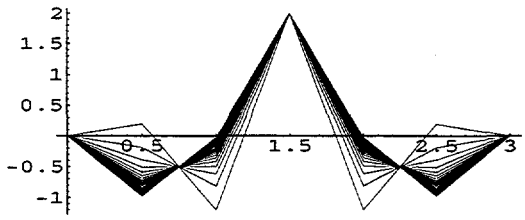

e)

Figure 3.3: Semi-orthogonal Sombrero for a) $\epsilon = 0$, b) $\epsilon = 0.3$, c) $\epsilon = 0.5$, d) $\epsilon = 3$, and e) $0 \leq \epsilon \leq 3$ on a uniform grid with $0 \leq x \leq 3$.

and that

$$\frac{\max_\omega E_{\psi_k}(\omega)}{\min_\omega E_{\psi_k}(\omega)} \leq 1.2 \quad \text{for } 0.33 \leq \epsilon_k \leq 0.36. \tag{3.18}$$

Since A^{Ψ_k} is block diagonal, A^{Ψ_k} can be preconditioned with a simple diagonal preconditioner so that the resulting A^{Ψ_k} satisfies

$$\text{cond}(A^{\Psi_k}) = \max_{j \leq k} \text{cond}(A^{\psi_j}).$$

Then (3.18) shows that $\text{cond}(A^{\Psi_k})$ is uniformly bounded for $0 \leq \epsilon_k \leq \epsilon^*$ for any fixed ϵ^*. For instance, we get the following:

$$\text{cond}(A^{\Psi_k}) < \begin{cases} 2.4 & \text{for } \epsilon_k < .5 \\ 271 & \text{for } \epsilon_k < 2 \\ 1330 & \text{for } \epsilon_k < 3 \end{cases}$$

For the unbounded domain case we use the following well known Fourier trick (cf.[36]) to construct an a-orthogonal basis for $\mathcal{W}_k$. Let $(\xi_\ell)_{\ell \in \mathbb{Z}}$ denote the Fourier coefficients of $\sqrt{1/E_{\psi_k}}$ and define

$${}^{BL}\psi_k^j := \sum_\ell \xi_\ell \psi_k^{j+\ell}.$$

In the case $\epsilon = 0$, we get the usual Battle-Lemarié wavelets. In this case, A^{Ψ_k} is the identity matrix. It is interesting to observe that ${}^{BL}\psi_0^0$ appears to converge point-wise to the Schauder wavelet ${}^h\psi_0^0 = \phi_1^1$ as ϵ goes to infinity. The wavelet ${}^{BL}\psi$ is shown in Figure 3.4 for selected ϵ.

3.4.2 Hybrid Basis

Our goal is to achieve a robust, fully scalable algorithm that is uniformly $\mathcal{O}(N_K)$ independent of the size of the problem L, the maximum refinement level K, and the parameter ϵ. In this section we assume that our bases are normalized in the a-norm. This corresponds to a preconditioning of the form $D^{-1/2}AD^{-1/2}$ where D is the diagonal of A. We let ${}^h\Psi_k$ denote the normalized Schauder basis described in Section 3.3.1 and ${}^s\Psi_k$ the normalized Sombrero basis described in Section 3.4.

For the model problem, the semi-orthogonal basis is ill-conditioned for large ϵ and well-conditioned for small ϵ. One approach we have explored

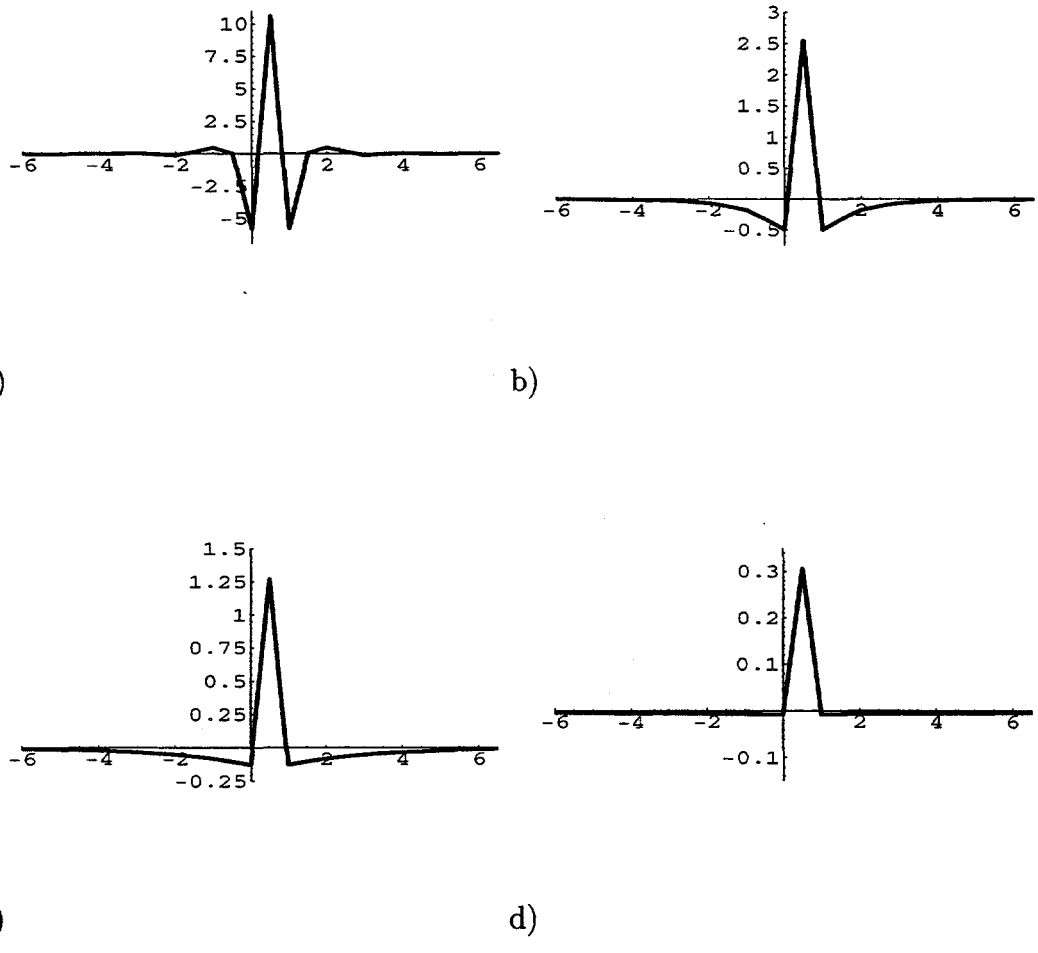

Figure 3.4: Battle-Lemarié type wavelets for a) $\epsilon = 0$, b) $\epsilon = 1$, c) $\epsilon = \sqrt{5}$, and d) $\epsilon = 10$.

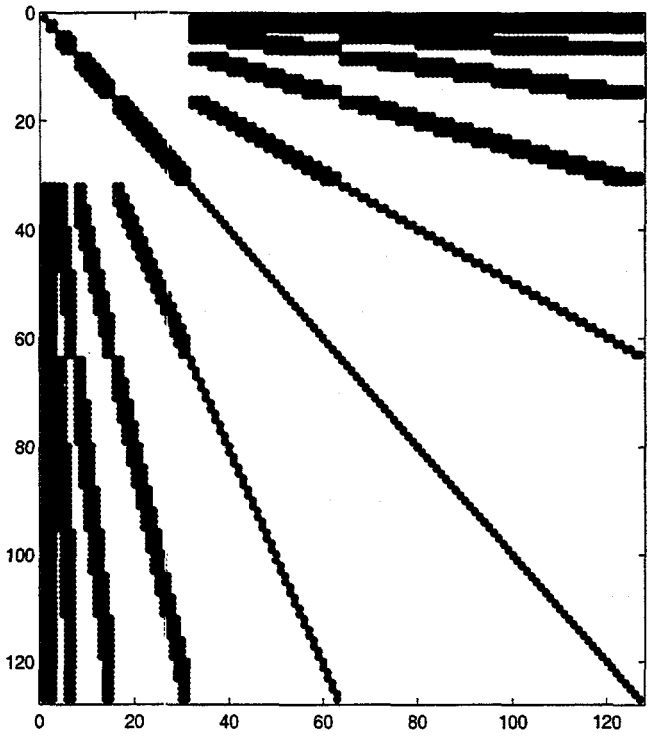

Figure 3.5: Non-zero entries in $A^{{}^{sh}\Psi_K}$ with 4 levels and the semi-orthogonal basis combined with 2 additional levels with the Schauder basis.

numerically is to use the hybrid basis

$$ {}^{sh}\Psi_K := \begin{pmatrix} {}^{s}\Psi_{\tilde{k}} \\ {}^{h}\psi_{\tilde{k}+1} \\ \vdots \\ {}^{h}\psi_K \end{pmatrix} $$

where $\tilde{k}$ is chosen so that $\epsilon_{\tilde{k}} = \mathcal{O}(1)$. The resulting discretized matrix $A^{{}^{sh}\Psi_K}$ is illustrated in Figure 3.5. Our numerical experiments indicate that the hybrid basis achieves the above mentioned goals for the model problem.

3.5 Summary

The approach taken for the semi-hat bases has relied on relaxing the orthogonality constraints and relying on an algorithmic approach that does not require the inverse wavelet transform, W^{-1}. The goal for these bases was to demonstrate the use of semi-orthogonal wavelets that are constructed to have certain algorithmic properties, i.e., semi-orthogonal with respect to an elliptic bilinear form, $a(\cdot,\cdot)$. The construction of a hybrid basis was demonstrated to provide well-conditioned Galerkin discretizations of an elliptic model problem independent of the model parameters, ϵ, L, and the refinement level or grid resolution. This approach follows the lines of the most recent research (see for example Dahmen and Stevenson[34] and Fröhlich and Schneider[39]) where wavelet bases are being designed specifically to yield stable discretizations with the condition number uniformly bounded independent of the grid resolution. The concepts put forward here are extended in the subsequent chapter where the theoretical issues and computational performance of the hierarchical Schauder basis are addressed.

Chapter 4

The Schauder Basis

In this chapter, the theoretical issues surrounding the well known Schauder basis[109,111] are presented. In one-spatial dimension, the "hierarchical" Schauder basis is the simplest uniformly stable H^1 basis that is available today. The uniform stability in H^1 yields uniformly bounded condition numbers, i.e., independent of refinement level (grid resolution), for elliptic operators in a Galerkin form. In the ensuing discussion, the details of a uniformly stable basis will be made concrete. In addition, a comparison between a hierarchical Schauder basis and the linear finite element basis is presented. The use of the wavelet transform in conjunction with the assembly of the mass and stiffness operators for a hierarchical basis is also presented. The application of an ad-hoc row-column lumping procedure for the hierarchical basis is outlined, and its effectiveness for solving elliptic boundary value problems in one and two-dimensions is demonstrated. Finally, 1-D and 2-D multi-scale finite elements based on the Schauder basis are outlined.

4.1 Stability

To begin the discussion on stability, several definitions are required.

Definition 1 *Given a basis* $\Phi = (\phi_0, \phi_1, \phi_2, \ldots)^T$ *for a subspace of a Hilbert Space,* H*, with norm* $\|\cdot\|_H := \sqrt{\langle \cdot, \cdot \rangle_H}$*. Define the associated discretized matrix as*

$$A^{\Phi} := \langle \Phi, \Phi \rangle_H := \left(\langle \phi_i, \phi_j \rangle_H \right)_{i,j \in \mathbb{Z}}.$$

Definition 2 *Suppose the vector Φ is a normalized basis for a Hilbert space, H. Then Φ is said to be stable in H if there exists constants $\alpha, \beta > 0$ such that*

$$\alpha\|c\|_{\ell^2}^2 \leq \|c^T\Phi\|_H^2 \leq \beta\|c\|_{\ell^2}^2.$$

This definition of stability is equivalent to the definition of a Riesz basis with respect to the $\|\cdot\|_H$ norm.

Now consider the following set of nested subspaces of H,

$$\mathcal{V}_0 \subset \mathcal{V}_1 \subset \cdots \subset \mathcal{V}_j \cdots \subset H,$$

such that Φ_j is a basis for $\mathcal{V}_j$.

Definition 3 *Given a nested sequence $\{\mathcal{V}_j\}_{j\in\mathbb{Z}^+}$ of subspaces of a Hilbert space H and their respective bases $\{\Phi_j\}_{j\in\mathbb{Z}^+}$ (normalized in H), then $\{\Phi_j\}_{j\in\mathbb{Z}^+}$ is uniformly stable in H if there exists constants $\alpha, \beta > 0$ independent of j such that*

$$\alpha\|c_j\|_{\ell^2}^2 \leq \|c_j^T\Phi_j\|_H^2 \leq \beta\|c_j\|_{\ell^2}^2 \qquad j = 0, 1, \ldots.$$

Next, the relationship between stability of a basis and the condition number of its associated discretized matrix is outlined. In particular, it will be demonstrated that a uniformly stable set of bases yields uniformly bounded condition numbers for the discretized matrices independent of the refinement level.

Lemma 1 *Let Φ be a basis for a subspace of a Hilbert space H such that A^Φ is positive definite. Let $\alpha = \|A^{\Phi^{-1}}\|_2^{-1}$ and $\beta = \|A^\Phi\|_2$. Then*

$$\alpha\|c\|_{\ell_2}^2 \leq \|c^T\Phi\|_H^2 \leq \beta\|c\|_{\ell^2}^2,$$

and

$$\mathrm{cond}(A^\Phi) = \frac{\beta}{\alpha}.$$

Proof:
For the second part, by definition the condition number of a symmetric matrix is given by $\mathrm{cond}(A^\Phi) = \|A^\Phi\|_2\|A^{\Phi^{-1}}\|_2$.

For the stability condition, note that

$$\frac{\|c^T\Phi\|_H^2}{\|c\|_{\ell^2}^2} = \frac{\left\langle c^T\Phi, c^T\Phi\right\rangle_H}{c^Tc} = \frac{c^TA^\Phi c}{c^Tc}.$$

Moreover, for symmetric matrices

$$\beta = \|A^\Phi\|_2 = \rho(A^\Phi) = \max_c \frac{c^T A^\Phi c}{c^T c}$$

which gives us the upper bound. For the lower bound, observe that for symmetric positive definite matrices

$$\alpha = \|A^{\Phi^{-1}}\|_2^{-1} = \left(\max_c \frac{c^T A^{\Phi^{-1}} c}{c^T c}\right)^{-1} = \min_c \frac{c^T A^\Phi c}{c^T c}.$$

■

Remark 4 *The proof of Lemma 1 states that the best stability bounds are provided by the smallest and largest eigenvalues of the discretized matrix – a well known fact.*

Example 4 *Linear finite element basis:*
Let $H = L^2(0,2)$, $h(x) = (1 - |x-1|)$, *and* $\phi_{j,k} = 2^{j/2}\sqrt{\frac{3}{2}}h(2^j \cdot -k)_+$ *where* $(\cdot)_+$ *is the usual ramp function. (Here, the subscript* $+$ *indicates that only the positive contributions to* $h(x)$ *are retained and all other function values are set to zero.) Define*

$$\begin{aligned} \mathcal{V}_j &= \text{span}\{\phi_{j,k}, k = 0, \ldots, 2^{j+1} - 2\}, \qquad j = 0, 1, \ldots, \\ \Phi_j &= \left(\phi_{j,0}, \phi_{j,1}, \ldots, \phi_{j,2^{j+1}-2}\right)^T. \end{aligned}$$

This basis for $j = 3$ *is shown in Figure 4.1.*

Note that the normalization of $\phi_{j,k}$ *is equivalent to diagonal preconditioning applied to the finite element mass matrix.*

Lemma 2 *The sequence of bases* $\{\Phi_j\}_j$ *from Example 4 is uniformly stable in* $L^2(0,2)$.

Proof:
The discretized matrix A^{Φ_j} corresponds to the diagonally scaled finite element mass matrix, and is a symmetric tridiagonal matrix consisting of 1 on

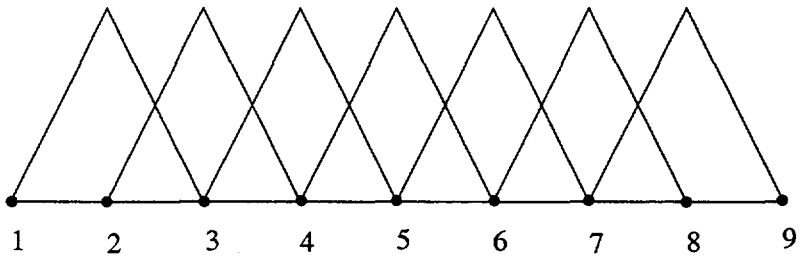

Figure 4.1: The linear finite element basis for level $j = 3$ with 8 elements and 9 nodes.

the diagonal and $1/4$ on the off diagonals. Using Gershgorin's theorem, the eigenvalues for A^{Φ_j} lie in the interval $[1/2, 3/2]$ giving

$$\frac{1}{2}\|c_j\|_{\ell^2}^2 \leq \|c_j^T \Phi_j\|_{L^2}^2 \leq \frac{3}{2}\|c_j\|_{\ell^2},$$

and $\text{cond}(A^{\Phi_j}) \leq 3$. ■

Recall the norm and semi-norm for the Sobolev space H^1 for one space dimension are

$$\begin{aligned} \|u\|_{H^1}^2 &= \|u'\|_{L^2} + \|u\|_{L^2} \\ |u|_{H^1}^2 &= \|u'\|_{L^2}. \end{aligned}$$

Theorem 1 *(Poincaré-Friedrich) For bounded domains, the H^m norm and semi-norm are equivalent in the sense that there exists constants $\alpha, \beta > 0$ such that*

$$\alpha|u|_{H^m} \leq \|u\|_{H^m} \leq \beta|u|_{H^m} \quad \textit{for} \quad u \in H_0^m.$$

Remark 5 *The stability associated with the finite element basis in L^2 is consistent with the empirical observation that the consistent mass matrix is well behaved in terms of its condition number. In practice, this is reflected in the ability to easily solve mass matrix dominated problems with simple iterative techniques.*

Lemma 3 *After re-normalization with respect to the H^1 semi-norm, the sequence of bases $\{\Phi_j\}_j$ from Example 4 is not uniformly stable in $H_0^1(0, 2)$.*

Proof:
Using the equivalence of the norm and semi-norm, we will construct a sequence of vectors $\{c_j\}_j$ for which uniform bounds are not possible. If

$$c_j = (\overbrace{1,1,1,\ldots,1,1}^{2^{j+1}-1}) \quad for \quad j = 0,1,2,\ldots,$$

then

$$\|c_j\|_{\ell^2}^2 = 2^{j+1} - 1 \quad and \quad |c_j^T \Phi_j|_{H^1}^2 = 1 \quad for \quad j = 0,1,2,\ldots.$$

■

Example 5 *Hierarchical Schauder Basis: Let ϕ and $\mathcal{V}_0$ be the same as in Example 4 and let*

$$\begin{aligned} \mathcal{W}_j &= \text{span}\{\phi_{j,k}, k = 0,2,4,\ldots 2^{j+1}-2\} \\ \mathcal{V}_j &= \mathcal{V}_0 \bigoplus_{k=1}^{j} \mathcal{W}_k \\ \Psi_j &= \left(\phi_{0,0}, \phi_{1,0}, \phi_{1,2}, \ldots, \phi_{j,0}, \phi_{j,2}, \ldots, \phi_{j,2^{k+1}-2}\right)^T \end{aligned}$$

where $\bigoplus$ is the direct sum. The hierarchical basis for $j = 3$ is shown in Figure 4.2.

Lemma 4 *After re-normalization with respect to the H^1 semi-norm, the sequence of bases $\{\Psi_j\}_j$ from Example 5 is uniformly stable in $H_0^1(0,2)$.*

Proof:
The H^1 semi-norm of $\{\Psi_j\}_j$ is equivalent to the L^2 norm of the orthogonal Haar wavelet basis. The Haar basis is an orthogonal basis for $L^2[0,2]$ and thus A^{Ψ_j} is the identity with respect to the semi-norm for $j = 0,1,2,\ldots,\infty$.
■

Lemma 5 *After re-normalization with respect to the L^2 norm, the sequence of bases $\{\Psi_j\}_j$ from Example 5 is not uniformly stable in $L^2(0,2)$.*

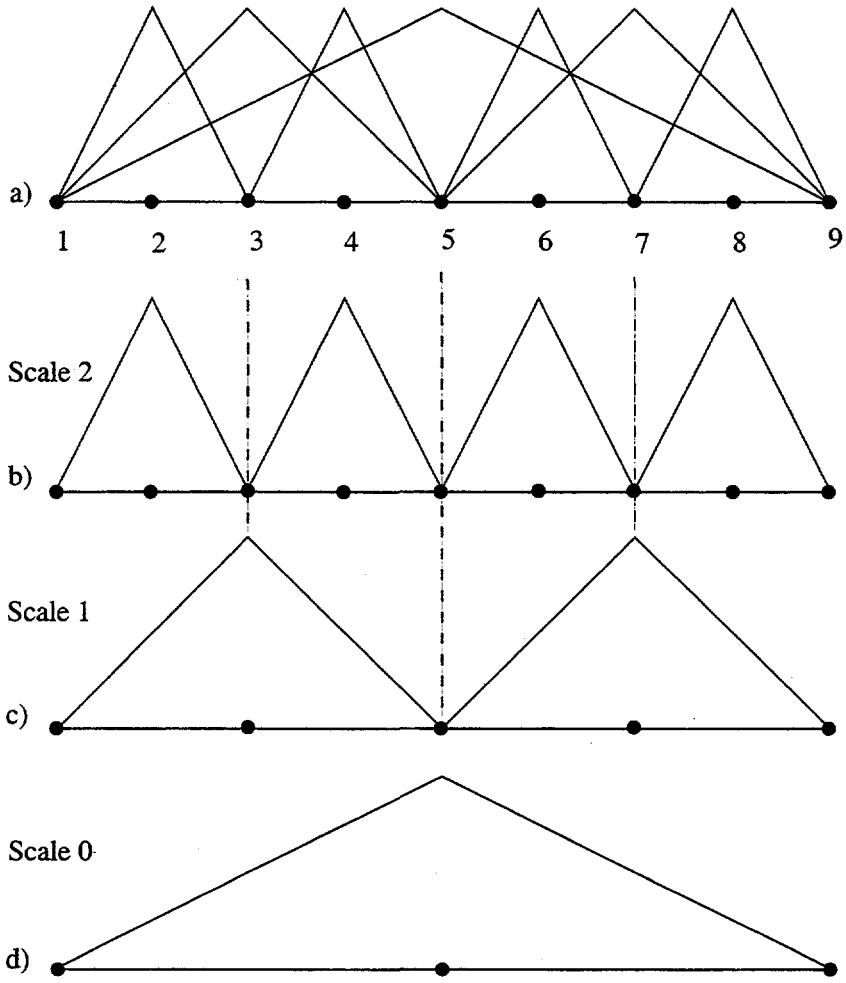

Figure 4.2: The hierarchical Schauder basis for level $j = 3$ showing a) the composite basis for 8 elements and 9 nodes, b) the basis functions for scale 2, c) the basis functions for scale 1, and d) the basis functions for scale 0.

Proof:
Define the sequence c_j which gives the hat function centered at one with support $[1-2^j, 1+2^j]$ as

$$c_j = (1, -1/2, -1/2, 0, -1/4, -1/4, 0, 0, 0, 0, -1/8, -1/8, 0, 0, 0, \ldots).$$

Thus,

$$\|c_j\|_{\ell^2}^2 \geq 1,$$

$$\|c_j^T \Psi_j\|_{L^2}^2 = \frac{2}{3}\frac{1}{2^j}.$$

■

4.2 Wavelet-Galerkin Method

In this section, a brief overview of the tensor product formulation for the Galerkin method is presented with "experimental" comparisons of the linear finite element and the hierarchical Schauder bases. We begin by defining the Frobenius product which generalizes the outer product of two matrices and gives a convenient general framework for the two-dimensional calculations.

Definition 4 *Frobenius Product: The Frobenius product* $\overset{F}{*}$ *of two rectangular matrices* A *and* B *of dimensions* $m \times n$ *and* $r \times s$ *respectively is the* $mr \times ns$ *matrix defined by*

$$A \overset{F}{*} B := (Ab(i,j))_{i,j} = \begin{pmatrix} Ab_{1,1} & Ab_{1,2} & \cdots & Ab_{1,s} \\ Ab_{2,1} & Ab_{2,2} & \cdots & Ab_{2,s} \\ \vdots & \vdots & \ddots & \vdots \\ Ab_{r,1} & Ab_{r,2} & \cdots & Ab_{r,s} \end{pmatrix}.$$

Remark 6 *Given rectangular matrices* A, B *and* C *with* B *and* C *having the same dimensions, the following are easily verified:*

$$A \overset{F}{*} B \neq B \overset{F}{*} A \quad for \quad A \neq B$$

$$\begin{aligned}(A \overset{F}{*} B)^T &= A^T \overset{F}{*} B^T \\ (B+C) \overset{F}{*} A &= B \overset{F}{*} A + C \overset{F}{*} A \\ A \overset{F}{*} (B+C) &= A \overset{F}{*} B + A \overset{F}{*} C.\end{aligned}$$

Definition 5 *Column stack: The column stack operator* $\vec{()}$ *of a rectangular matrix* C *of dimension* $m \times n$ *with column vectors* $c_1, c_2, \ldots, c_n$ *is the* $mn \times 1$ *vector defined by*

$$\vec{C} := \begin{pmatrix} c_1 \\ c_2 \\ \vdots \\ c_n \end{pmatrix}.$$

The inverse of the column stack operator will be denoted by $\overleftarrow{()}$.

Remark 7 *The Frobenius product is used here to permit the direct application of the one-dimensional wavelet transform in the development of the multi-scale mass and stiffness operators. The multi-scale finite element presented in subsequent sections illustrates the direct use of the multi-scale basis functions for the generation of the multi-scale operators.*

4.2.1 The Model Problem

In this section, the one and two-dimensional formulations are presented. For notational convenience the bases are configured as a vector in 1-D and a matrix in 2-D. Given a basis $\Phi(x)$ in 1-D, we form the 2-D tensor product basis, $\mathbf{\Phi}(x,y)$, using the Frobenius product as follows

$$\begin{aligned}\mathbf{\Phi}(x,y) &:= \Phi(x) \overset{F}{*} \Phi(y)^T \\ &= \begin{pmatrix} \phi^1(x)\phi^1(y) & \phi^1(x)\phi^2(y) & \cdots & \phi^1(x)\phi^n(y) \\ \vdots & \ddots & \vdots & \vdots \\ \phi^n(x)\phi^1(y) & \phi^n(x)\phi^2(y) & \cdots & \phi^n(x)\phi^n(y) \end{pmatrix}.\end{aligned}$$

The boundary value problem with homogeneous Dirichlet boundary conditions is

$$\begin{aligned} -\epsilon\Delta u + u &= f \quad \text{on} \quad \Omega \\ u &= 0 \quad \text{on} \quad \Gamma. \end{aligned} \tag{4.1}$$

The discrete formulation of (4.1) is

1-D:

$$(M_k + \epsilon K_k)c = f_k^{\Phi},$$

$$\begin{aligned} M_k &:= \left(\int_\Omega \phi_k^i(x)\phi_k^j(x)dx\right)_{i,j} \\ K_k &:= \left(\int_\Omega \partial_x\phi_k^i(x)\partial_x\phi_k^j(x)dx\right)_{i,j} \\ f_k^{\Phi} &:= \left(\int_\Omega f(x)\phi_k^j(x)dx\right)_j. \end{aligned}$$

2-D:

$$(M_k^{2d} + \epsilon K_k^{2d})\,\vec{C}_k = \vec{F}_k^{\Phi},$$

where

$$\begin{aligned} M_k^{2d} &= M_k \overset{F}{*} M_k \\ K_k^{2d} &= M_k \overset{F}{*} K_k + K_k \overset{F}{*} M_k \\ \vec{F}_k^{\Phi} &= \left(\int_\Omega f(x)\phi_k^i(x)\overrightarrow{\phi_k^j}(y)dxdy\right)_{i,j}. \end{aligned}$$

For Galerkin formulation, $u_k, v_k \in \mathcal{V}_k \overset{finite}{\subset} H_0^1$, where Φ_k is a finite dimensional basis for the subspace $\mathcal{V}_k$. Here, $u_k = c_k^T\Phi_k(x)$ and $u_k^{2d} = \Phi_k(x)^T C_k \Phi_k(y)$ for one and two dimensions respectively.

4.2.2 1-D Comparison: Schauder vs. Linear Finite Element

With the Galerkin formulation for the model problem established, a comparison between the hierarchical basis and the linear finite element basis on a uniform discretization is presented. It should be noted that the hierarchical Schauder basis retains its properties for a non-uniform grid as well. In Figure 4.3, the non-zero entries of the mass and stiffness matrices are illustrated for both the Schauder and the linear finite element bases. The non-zero structure of the mass matrix for the Schauder basis has been termed a "finger diagonal matrix".

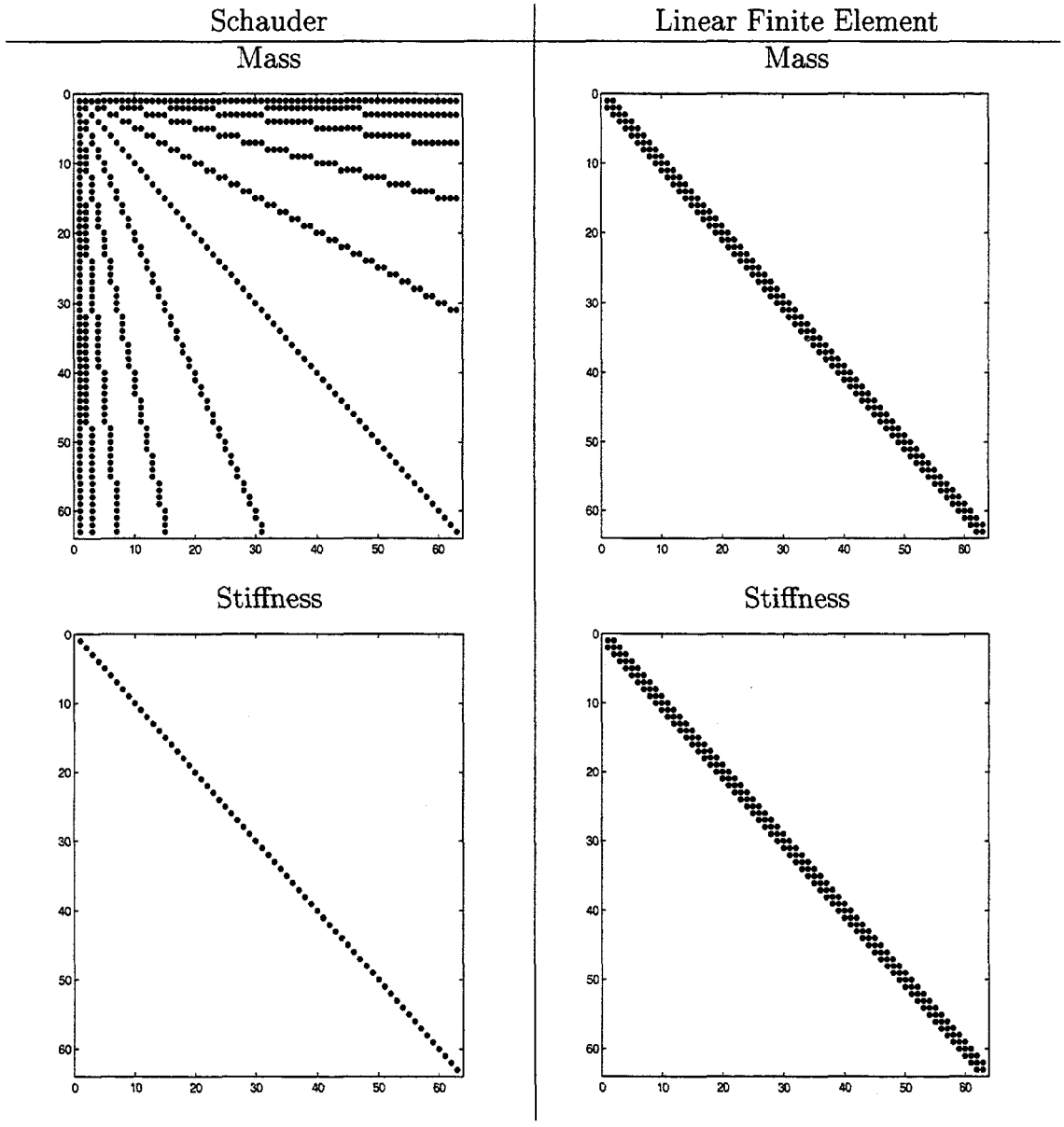

Figure 4.3: The nonzero entries in the mass and stiffness matrices for both the Schauder and linear finite element bases for a mesh with 64 nodes.

Number of non-zeros in the 1-D mass and stiffness matrices.			
Basis-matrix	Level	Unknowns	Non-zeros
Linear Finite Element – M_k	k	N	$3N-2$
Linear Finite Element – K_k	k	N	$3N-2$
Schauder – M_k	k	N	$(2k-1)(N+1)+3$
Schauder – K_k	k	N	N

Table 4.1: Formulas for the number of non-zeros in the 1-D mass and stiffness matrices where $N = 2^{k+1} - 1$.

The number of non-zeros can be calculated for the mass and stiffness operators for both the Schauder and finite element bases and are shown in Table 4.1. Because the Schauder basis diagonalizes the stiffness, the storage is N for the the diagonal, while the finger-diagonal mass matrix, although sparse, requires increased storages relative to the tri-diagonal finite element mass matrix.

Attention is now turned to the condition number associated with each operator. In general, the finite element mass matrix and the Schauder stiffness matrix are both well conditioned operators. In fact, the Schauder stiffness is ideal since this choice of basis makes the stiffness operator diagonal. In contrast, the finite element stiffness and the Schauder mass matrices are both poorly conditioned operators. To be more precise, the finite element basis is uniformly stable in L^2, but it is not in H^1. In contrast, the Schauder basis is uniformly stable in H^1, but it is not stable in L^2. Again, the concept of a stable basis is defined in §4.1.

In order to illustrate the differences between the finite element and the Schauder bases, consider the condition numbers associated with the mass and stiffness operators for the finite element and Schauder bases shown in Table 4.2. Here, multiple levels of mesh refinement are considered with $k = 1$ corresponding to a mesh with 3 nodes (2 elements). The growth of the condition numbers for K_k is seen to be proportional to $O(h^{-2})$ for the linear finite element bases, while the condition numbers for the mass matrix are bounded asymptotically at 3. The condition number associated with the combined mass and stiffness operator is dominated by the stiffness for the finite element basis in this case since $\epsilon = 1$. In contrast, the mass matrix for the Schauder basis yields a condition number that grows approximately as $O(h^{-3/2})$ while the condition number for the stiffness is uniformly bounded at

Condition Numbers: 1-D						
Level	Linear Finite Element			Schauder		
k	M_k	K_k	$M_k + K_k$	M_k	K_k	$M_k + K_k$
1	2.09	6	4	7	1	1.23
2	2.71	25	18	18	1	1.27
3	2.92	103	74	49	1	1.29
4	2.98	414	295	121	1	1.29
5	3.00	1659	1181	288	1	1.29
6	3.00	6640	4724	667	1	1.29
7	3.00	26560	18900	1517	1	1.29

Table 4.2: Condition numbers for the 1-D mass and stiffness matrices after diagonal preconditioning.

$O(1)$. Surprisingly, the combined mass and stiffness operator for the Schauder basis is also uniformly bounded indicating the dominance of the stiffness in this example.

Mass Lumping

An ad-hoc procedure of mass lumping is considered in this section. In a finite element setting, mass lumping refers to the row-sum lumping procedure used to obtain a diagonal mass matrix. The use of a lumped mass matrix can have deleterious effects, particularly for problems with a dominant hyperbolic character.[19,45] Here, the interest in mass lumping is due to the computational gains that may be obtained for the Schauder mass matrix, i.e., it would be convenient to have both a diagonal mass and diagonal stiffness matrix. However, in the context of a multi-scale basis, the physical interpretation of mass lumping is not simple, and the idea is perhaps even less well founded than the use of mass lumping for the linear finite element basis.

Regardless of these issues, experimentation with mass lumping has suggested that it may be a viable procedure for the multi-scale Schauder basis. After a brief trial and error process, it was determined that lumping the mass by summing the values to the left and above the diagonal entry to the diagonal works the best. Thus, after a simple vector divide and a multi-scale reconstruction, an approximation to the solution is obtained. Inspection of the resulting approximate wavelet coefficients obtained by the lumping pro-

cedure indicated that a small correction to the largest wavelet coefficients can dramatically improve the solution quality. This process amounts to permuting the rows and columns of $A := M_k + \epsilon K_k$ with respect to the largest lumped approximate wavelet coefficients and solving for these coefficients with a correction from the smaller "lumped" approximate coefficients. The lumped-mass algorithm proceeds as follows.

Algorithm 1 *Lumped-Mass Correction Algorithm*

1. *Lump the mass matrix resulting in a diagonal matrix,* $A^L := M_k^L + \epsilon K_k$.
2. *Calculate the lumped approximate wavelet coefficients* d^L *by dividing* f^Φ *by the diagonal entries of* A^L.
3. *Permute the components of* d^L *so that the largest* N *coefficients are at the top. Let* d^N *be the largest* N *lumped-approximate wavelet coefficients and* d^R *be the remaining coefficients such that*

$$perm(d^L) = \begin{pmatrix} d^N \\ d^R \end{pmatrix}.$$

4. *Permute the rows and columns of* A *to match the permutation of* d^L. *Let the superscript* N *denote the first* N *rows and* R *the remaining rows.*
5. *Solve the smaller system, i.e., the coarse-grid correction,*

$$perm(A)^N d^N = perm(f^\Psi)^N - perm(A)^R d^R.$$

In practice, the coefficients associated with the coarsest grid resolution tend to be the largest and are the ones that need to be corrected. Thus, the permutation step can be replaced with a solve of the N coarsest coefficients however they are arranged. Figure 4.4 illustrates the effectiveness of the mass lumping for the hierarchical Schauder basis for solving the model problem with $\epsilon = 1$. Here, $\epsilon = 1$ was chosen because it provides equal weighting between the mass and stiffness operators.

Further experimentation with the idea of the row-column lumping has demonstrated that using the lumped approximate solution at level k and a correction for the coarsest coefficients of level $k-2$ yields significantly reduced

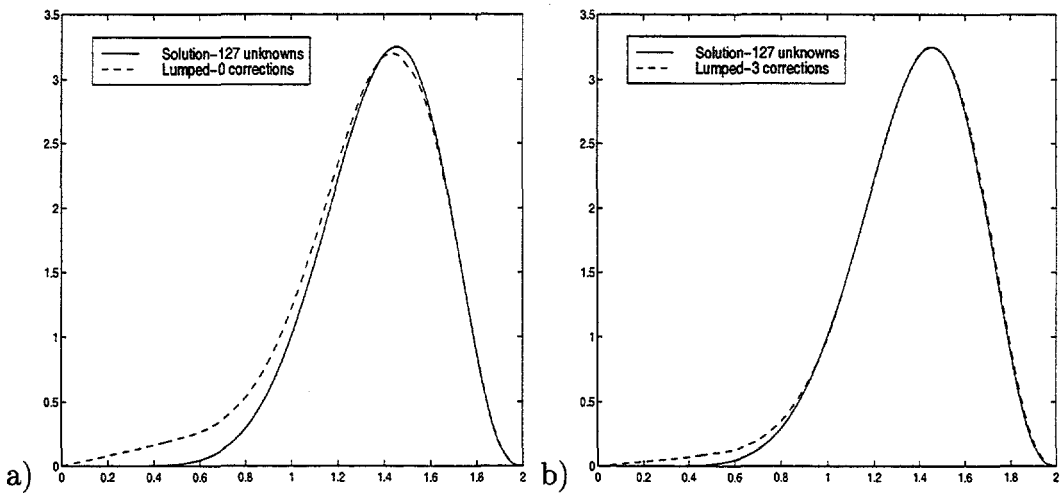

Figure 4.4: Solutions, u, on $0 \leq x \leq 2$ using the Schauder basis with mass-lumping and a) no corrections and b) 3 wavelet coefficient corrections.

error in H^1 when compared to solving the consistent system at level $k-2$. This effect is shown in Table 4.3 where the H^1 error for the consistent and lumped-corrected results are compared. Thus, in this algorithm, the mass lumping can improve the approximation order with respect to the number of unknowns solved for using the conjugate gradient method.

4.2.3 2-D Comparison: Schauder vs. Linear Finite Element

In two dimensions, the behavior of the Schauder basis changes rather significantly. Most apparent is the change in the structure of the stiffness matrix which is no longer diagonal, but is a finger diagonal matrix. This is shown in Figure 4.5 for a 32×32 mesh. In addition, the $O(1)$ conditioning for the discretized 1-D stiffness matrix becomes $O(log(h^{-2}))$ in 2-D. Because of the change in sparsity of the stiffness matrix and the conditioning, computational complexity becomes an important issue in the comparison between the Schauder and linear finite element bases.

Recall that the system of equations to be solved is

$$(M_k^{2d} + \epsilon K_k^{2d})\, \vec{C}_k = \vec{F}_k^{\Phi}\,.$$

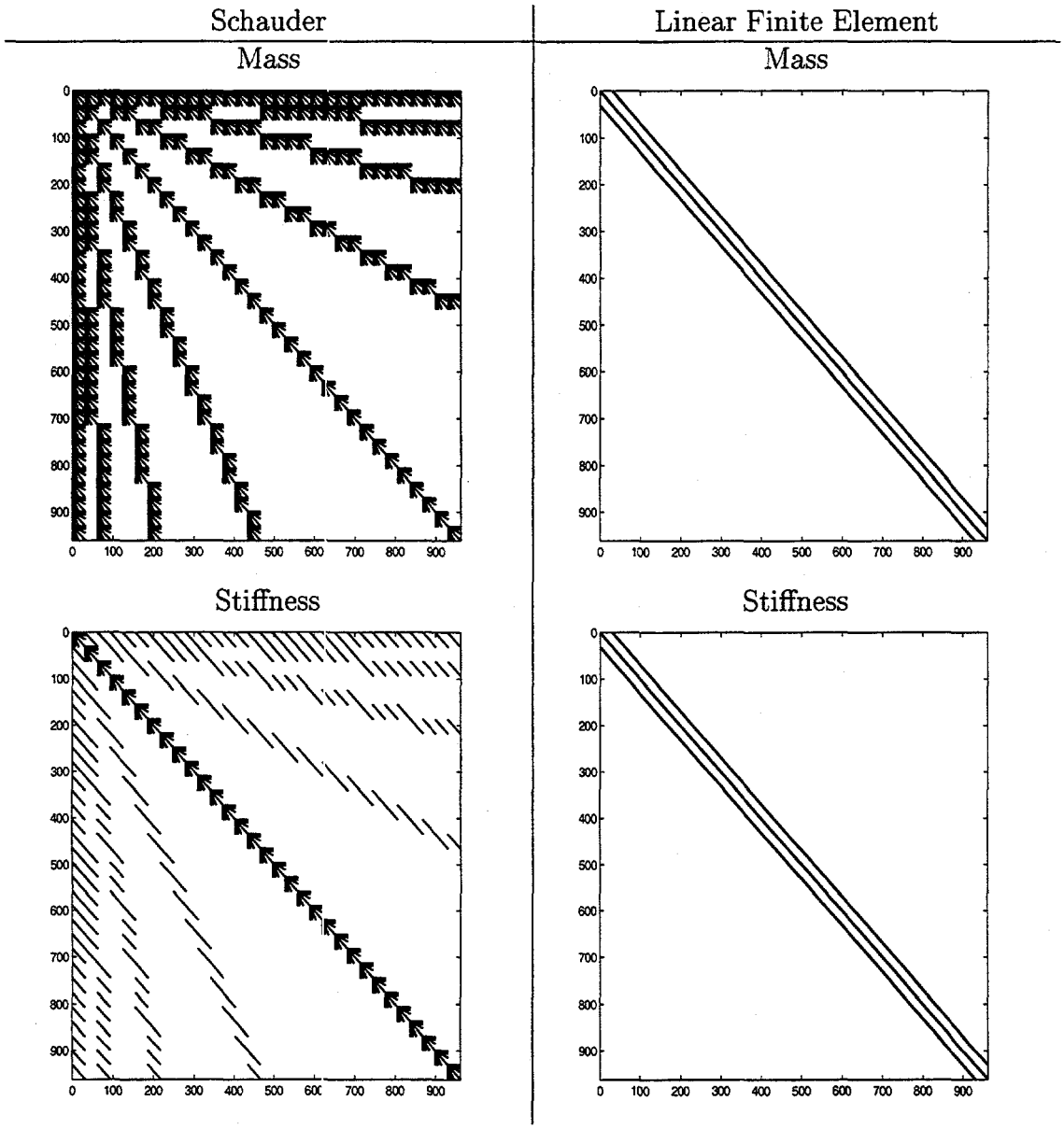

Figure 4.5: The nonzero entries in the mass and stiffness matrices generated with the Schauder and linear finite element bases in 2-D for a 32×32 mesh.

Mass Lumping Comparison		
Number of	H^1 – Error	
Unknowns	Consistent	Lumped
7	3.0467	1.7719E-1
15	3.2727E-1	6.7459E-2
31	7.0667E-1	1.9166E-2
63	1.7120E-2	4.9829E-3
127	4.2464E-3	1.2600E-3
255	1.0594E-3	3.1587E-4
511	2.6467E-4	7.8867E-5
1023	6.6141E-5	1.9565E-5

Table 4.3: Comparison of H^1 error for equivalent conjugate gradient method unknowns for the consistent and lump-corrected solutions for the model problem with $\epsilon = 1$.

Because M_k^{2d} and K_k^{2d} can be created by the Frobenius product of the 1-D matrices, the number of non-zero entries in the mass and stiffness operators may be easily computed. The formulae for the number of non-zero entries in the mass and stiffness operators are shown in Table 4.4.

Number of non zeros in 2-D mass and stiffness matrices.			
Basis–matrix	Level	Unknowns	Non zeros
Linear Finite Element – M_k^{2d}	k	N^2	$(3N-2)^2$
Linear Finite Element – K_k^{2d}	k	N^2	$(3N-2)^2$
Schauder – M_k^{2d}	k	N^2	$((2k-1)(N+1)+3)^2$
Schauder – K_k^{2d}	k	N^2	$N((4k-3)(N+1)+7)$

Table 4.4: Formulae for the number of non zeros in 2-D mass and stiffness matrices where $N = 2^{k+1} - 1$.

As mentioned above, in two dimensions, the condition numbers for the stiffness matrix using the Schauder basis grows as $O(log(h^{-2}))$. In contrast, the condition number for the finite element stiffness (using the 2-D bilinear element) grows as $O(h^{-2})$ regardless of the dimensionality. Table 4.5 illustrates how the condition numbers grow for the model problem.

Condition Numbers: 2-D						
Level	Linear-Finite Element			Schauder		
k	M_k	K_k	$M_k + K_k$	M_k	K_k	$M_k + K_k$
1	4	3	3	49	7	8
2	7	13	11	334	18	19
3	9	52	43	2396	49	51
4	9	207	172	14621	121	123
Estimation based on trend						
5	9	828	688	102347	303	308
6	9	3312	2752	716429	758	770

Table 4.5: Condition numbers for the 2-D mass and stiffness matrices after diagonal scaling.

In order to estimate the computational cost associated with solving the problem with the Schauder basis, both the number of non-zero entries in the matrix, and the number of iterations required to solve the problem are required. Table 4.6 shows the number of non-zero entries and associated iteration count for the Schauder and linear finite element bases for the model problem with $0 \leq \epsilon \leq 1000$. Due to the finger-diagonal structure of the hierarchical basis, the number of non-zero entries grows nearly exponentially for the Schauder basis.

During experimentation with the 2-D Schauder basis, it was observed that the number of non-zero entries in the stiffness matrix grows more slowly than for the mass matrix. This effect is shown in Table 4.7 with the iteration count associated with a Jacobi preconditioned conjugate gradient algorithm.

However, accounting for both the number of non-zero entries, and the number of iterations, i.e., the number of floating point operations per solve, the Schauder basis does have a lower overall computational cost for large problems.

Using these various estimates, Table 4.8 gives an order of magnitude estimate for the computational complexity for the Schauder and linear finite element bases. From this data, the Schauder basis does eventually have a lower computational cost as shown in Figure 4.6. For the "purely" elliptic operator, K_k^{2d}, the Schauder basis wins, i.e., has lower computational cost, for mesh resolution exceeding 10^5 degrees-of-freedom. In contrast, for the

Schauder Basis $M_k^{2d} + \epsilon K_k^{2d}$: Number of CG iterations							
Level	Unknowns	Non zeros	$\epsilon = 0$	$\epsilon = 0.1$	$\epsilon = 1$	$\epsilon = 10$	$\epsilon = 1000$
1	9	49	3	3	3	3	3
2	49	729	11	10	10	9	9
3	225	6889	50	27	25	22	22
4	961	51529	187	48	42	37	37
5	3969	335241	488	73	61	52	51
6	16129	1990921	979	107	87	70	59
Linear Finite Element Basis $M_k^{2d} + \epsilon K_k^{2d}$: Number of CG iterations							
Level	Unknowns	Non zeros	$\epsilon = 0$	$\epsilon = 0.1$	$\epsilon = 1$	$\epsilon = 10$	$\epsilon = 1000$
1	9	49	3	3	3	3	3
2	49	361	6	6	7	7	7
3	225	1849	7	13	15	16	16
4	961	8281	6	27	31	31	31
5	3969	34969	5	54	62	63	63
6	16129	143641	3	110	125	126	126

Table 4.6: Jacobi preconditioned conjugate gradient iterations required for the Schauder and linear finite element bases in 2-D.

Schauder Basis for K_k^{2d}: Number of PCG iterations			
Level	Unknowns	Non zeros	$\epsilon = \infty$
1	9	33	3
2	49	329	9
3	225	2265	22
4	961	13113	37
5	3969	68985	51
6	16129	342265	59

Table 4.7: Storage requirements and Jacobi preconditioned conjugate iterations for "purely" elliptic model problem.

$M_k^{2d} + \epsilon K_k^{2d}$ case, the Schauder basis does not win until the mesh resolution exceeds 10^8.

Mass Lumping in 2-D

For the purposes of this study, the lumped 2-D mass matrix was generated by lumping the 1-D mass matrix and then forming the 2-D mass and stiffness matrices using the Frobenius product. Since the stiffness matrix is diagonal for the 1-D Schauder basis, the resulting 2-D mass and stiffness matrices are diagonal. In one sense, this is akin to lumping the stiffness matrix. Although the row-sum lumping procedure is not valid for the nodal basis, it is valid for the multi-scale representation of the stiffness. In other words, the multi-scale representation of the stiffness does not retain the "row-sum to zero" property of the nodal stiffness matrix. Thus, after doing a vector divide and a multi-scale reconstruction, the result is a reasonable initial solution. Figure 4.7 illustrates the lumped-approximation with no correction and the correction of the largest wavelet coefficient respectively. Using the lumped-approximation as an initial solution shows some promise as a component of an overall solution strategy. For example, the row-column lumping procedure could be used to generate a good initial solution for an iterative procedure. As shown in Table 4.9, using the lumped-approximate solution as an initial guess reduces the number of iterations required to solve the linear system.

Computational Complexity Comparison							
		# Unknowns		# Non zeros			
Basis	Level	1D	2D	1D	2D	Iter-2D	Flops
Lin-FEM	k	N	N^2	$3N$	$9N^2$	N	$9N^3$
Sch-$(M+\epsilon K)$	k	N	N^2	$2kN$	$4k^2N^2$	$12k$	$48k^3N^2$
Sch-K	k	N	N^2	N	$4kN^2$	$12k$	$48k^2N^2$

Table 4.8: Computational comparison between the linear finite element and the hierarchical Schauder basis where $N = 2^k$.

Schauder Basis $M_k^{2d} + K_k^{2d}$: Number of PCG iterations w/ initial approx.							
Level	Unknowns	Non zeros	$\epsilon = 0$	$\epsilon = 0.1$	$\epsilon = 1$	$\epsilon = 10$	$\epsilon = 1000$
1	9	49	3	3	3	3	3
2	49	729	11	10	9	10	9
3	225	6889	51	26	21	22	22
4	961	51529	178	47	38	33	37
5	3969	335241	494	70	57	48	48
6	16129	1990921	899	101	80	66	56

Table 4.9: Number of PCG iterations using the lumped approximation as an initial guess.

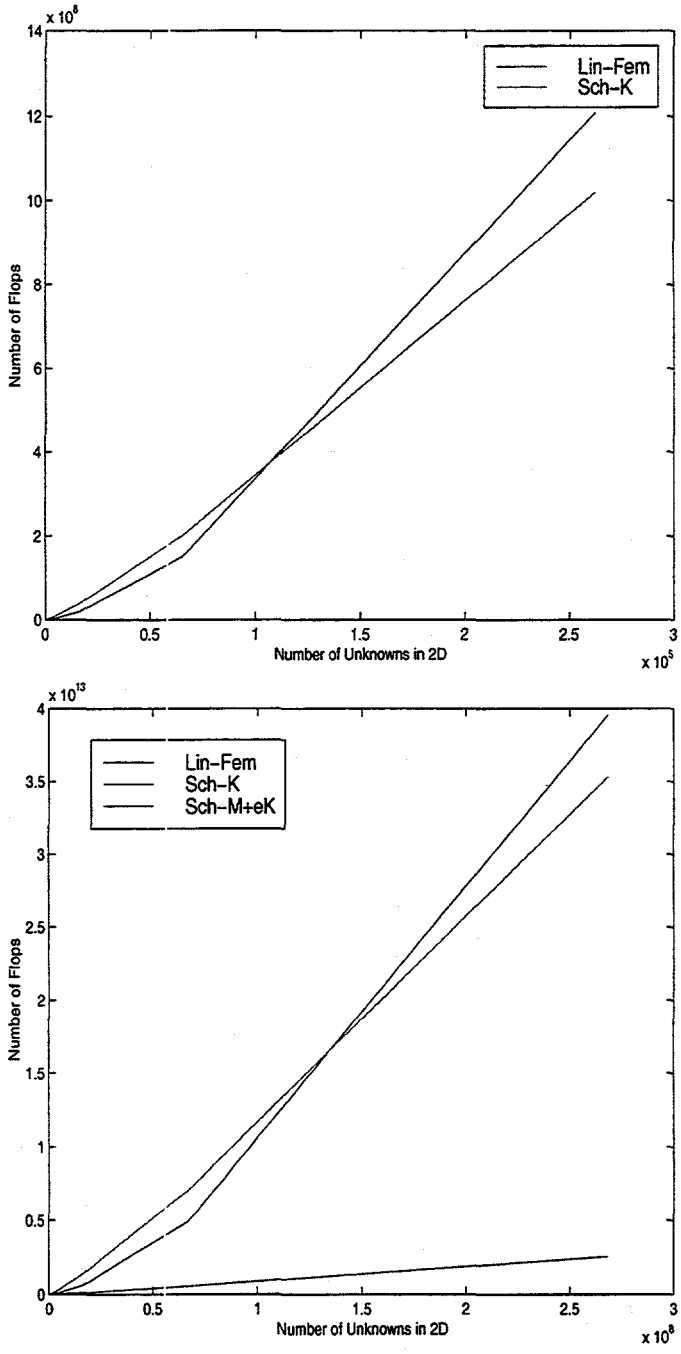

Figure 4.6: Number of unknowns versus number of flops

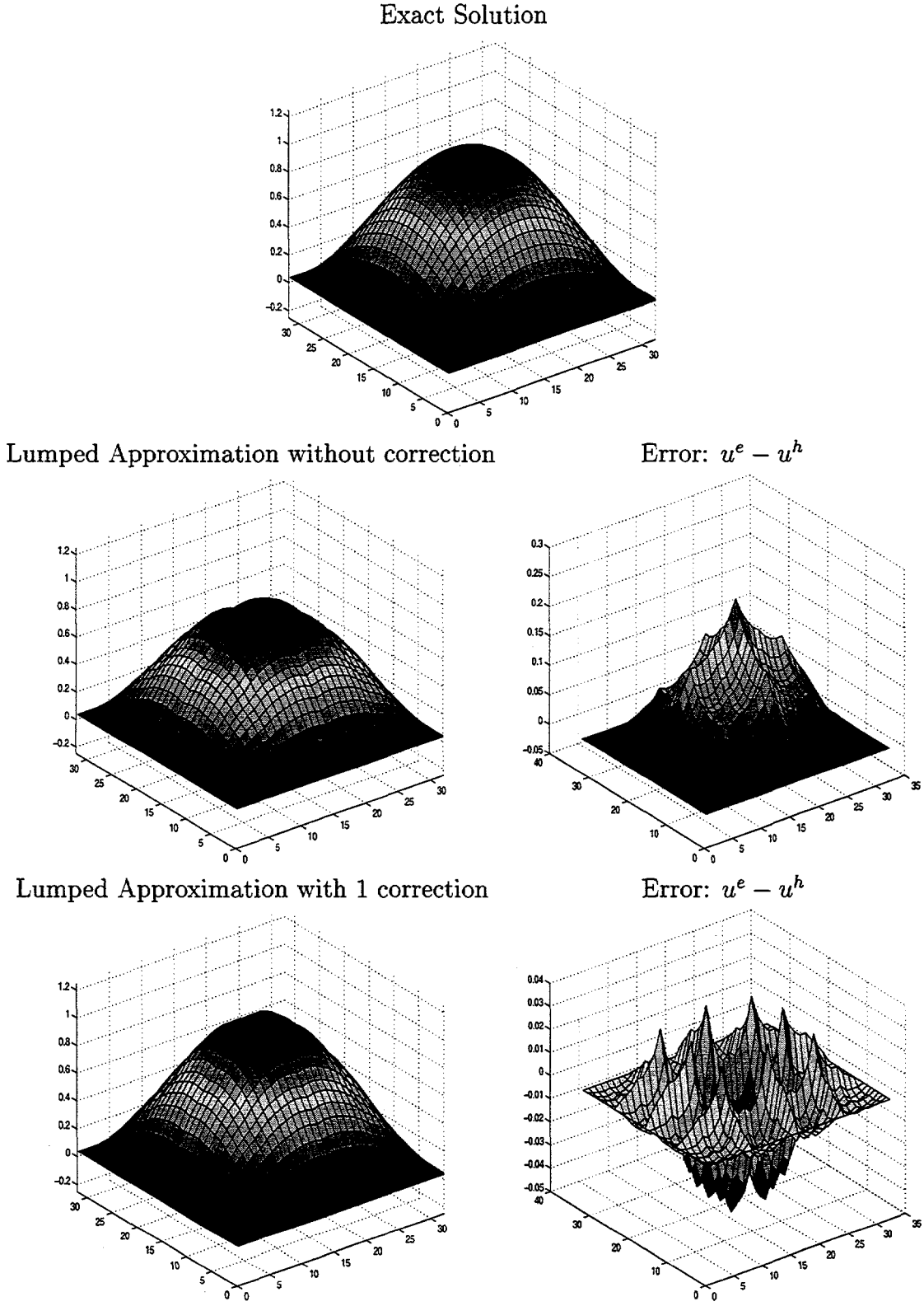

Figure 4.7: The exact and approximate solutions using the lumping procedure with and without wavelet correction for a 32×32 2-D mesh. (u^e is the interpolant of the exact solution, and u^h is the discrete solution.)

4.3 The Multi-Scale Finite Element

This section outlines the 1-D and 2-D multi-scale finite element formulations. The multi-scale element is based upon the Schauder basis with the change-of-basis incorporated at the element-level in order to make use of the well-known finite element assembly procedure.[51]

4.3.1 Multi-Scale Transformations Revisited

Before embarking on a description of the 1-D multi-scale finite element, a brief review and interpretation of the multi-scale transformation is presented. Recall from §3.2 that

$$\Psi_k = W_k^T \Phi_k, \tag{4.2}$$

where W_k is the multi-scale transformation operator.

In order to make this transformation concrete, consider the following example. Beginning with a 1-D grid consisting of 5 grid points and 4 linear elements, the nodal basis will be decomposed into a coarse-grid consisting of two elements and the associated "pseudo-wavelets". This decomposition is shown schematically in Figure 4.8.

Remark 8 *Here, the term "pseudo-wavelet" refers to the fact that the elements of $\mathcal{W}_k$ in the Schauder basis do not possess the property that their zeroth moment is zero. However, the elements of $\mathcal{W}_k$ are used to complete the subspace at scale k and they are semi-orthogonal in an H^1 sense so the term pseudo-wavelet seems appropriate.*

In this example, the wavelet transform, $\Psi_0 = W_1^T \Phi_1$, is

$$\begin{Bmatrix} \phi_0^3 \\ \psi_0^1 \\ \psi_0^2 \end{Bmatrix} = \begin{bmatrix} 1/2 & 1 & 1/2 \\ 1 & 0 & 0 \\ 0 & 0 & 1 \end{bmatrix} \begin{Bmatrix} \phi_1^2 \\ \phi_1^3 \\ \phi_1^4 \end{Bmatrix}, \tag{4.3}$$

where the subscript indicates the scale, and the superscript indicates the node number. From this, it is clear that the wavelet transform performs an averaging procedure to obtain the coarse-grid basis elements, Φ_0, and an injection to obtain the coarse-grid pseudo-wavelets, Ψ_0.

The decomposition of nodal variables, u, may be accomplished with the wavelet transform as well. Here, the inverse transform is required to obtain the coarse-grid coefficients

$$\Delta u = W^{-1}u, \tag{4.4}$$

where Δu is the multi-scale or incremental component of the field. Relying on the inverse wavelet transform is impractical because the orthogonality constraint between the wavelets and scaling functions have been relaxed in the Schauder basis. However, incorporating the Schauder basis at the element level will yield solution algorithms that compute the multi-scale solution directly and rely only on the reconstruction algorithm, i.e., $u = W\Delta u$. Thus, given a multi-scale representation of the field that corresponds to the multi-scale basis elements in Figure 4.8, the reconstruction algorithm is simply

$$\left\{ \begin{array}{c} u_1^2 \\ u_1^3 \\ u_1^4 \end{array} \right\} = \left[\begin{array}{ccc} 1/2 & 1 & 0 \\ 1 & 0 & 0 \\ 1/2 & 0 & 1 \end{array} \right] \left\{ \begin{array}{c} u_0^3 \\ \Delta u_0^1 \\ \Delta u_0^2 \end{array} \right\}. \tag{4.5}$$

Thus, the reconstruction algorithm relies on data at both the coarse grid and the detail from the "pseudo-wavelets", Δu, at the finer scales. These concepts are carried over to the finite element methodology where the reconstruction algorithm is applied at the element level.

As an aside, the wavelet transform is comprised of two components and both may be viewed in terms of a discrete convolution. Using the nomenclature introduced in Chapter 3, $T_1 = [H_1|G_1]$, where

$$H_1 = \left[\begin{array}{c} 1/2 \\ 1 \\ 1/2 \end{array} \right], \tag{4.6}$$

and

$$G_1 = \left[\begin{array}{cc} 1 & 0 \\ 0 & 0 \\ 0 & 1 \end{array} \right]. \tag{4.7}$$

In this simple example of a two-scale decomposition, $W_1 = T_1$, but in general, the wavelet transform is computed recursively as

$$W_k = T_k \left[\begin{array}{cc} T_{k-1} & 0 \\ 0 & I_{k-1} \end{array} \right] \cdots \left[\begin{array}{cc} T_1 & 0 \\ 0 & I_1 \end{array} \right]. \tag{4.8}$$

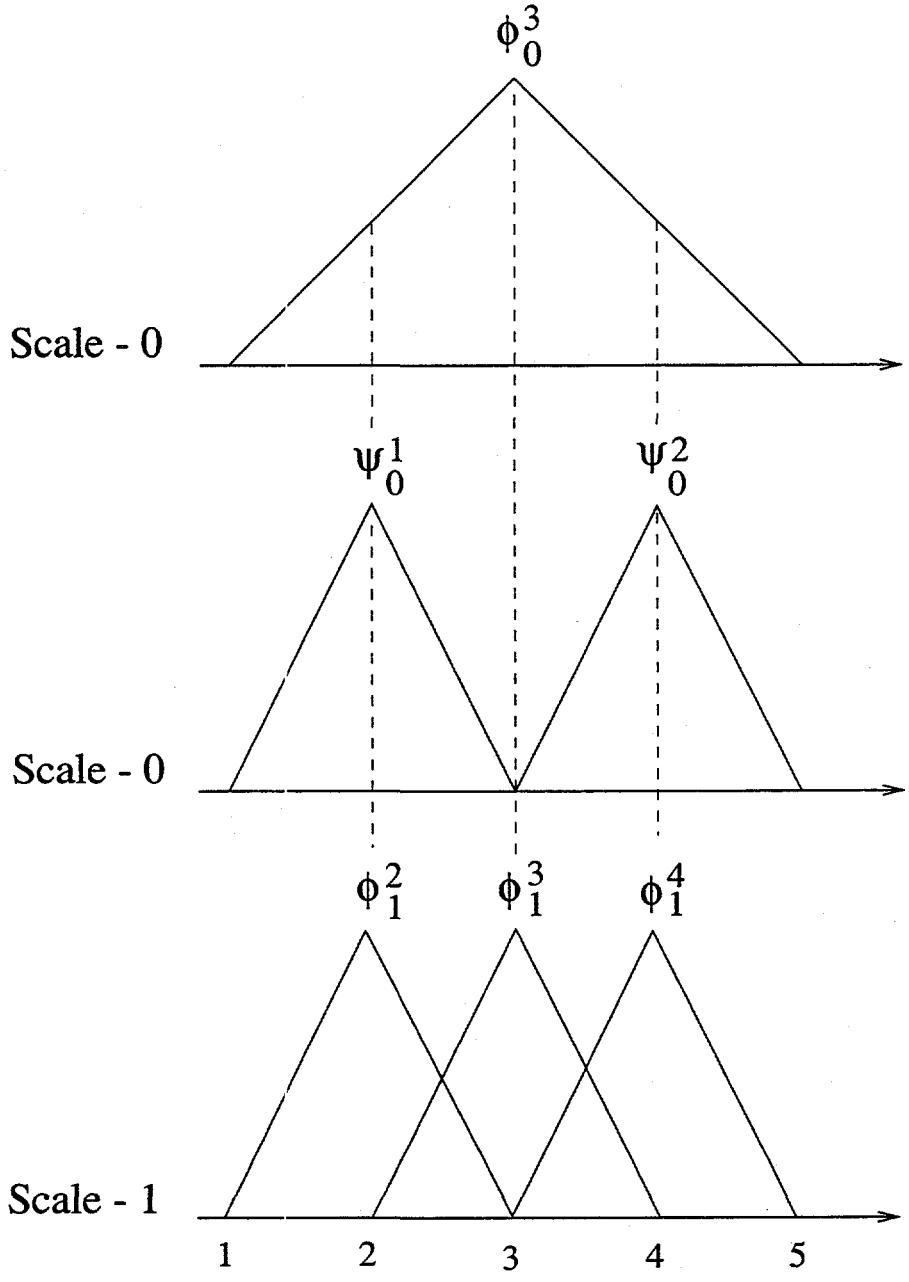

Figure 4.8: One dimensional two-scale decomposition of the finite element nodal basis.

4.3.2 One-Dimensional Element

The description of the multi-scale element begins with the linear finite element for which the shape functions are

$$N_i = \frac{1}{2}(1 - \xi_i \xi). \tag{4.9}$$

Here, ξ is the natural coordinate, ξ_i is the nodal value of the natural coordinate, $i = 1, 2$, and $-1 \leq \xi \leq 1$ for the linear element.

The concept of scale is introduced at the element level by injecting degrees-of-freedom (DOF) that are supported by the "pseudo-wavelets" of the Schauder basis. The 1-D multi-scale element is shown in Figure 4.9 where a single "internal" degree-of-freedom located at $\xi = 0$ in the element is introduced at Scale-1, two DOF are introduced at Scale-2, and four DOF at Scale-3.

At Scale-1, the pseudo-wavelet is

$$\psi_1(\xi) = \begin{cases} 1 + \xi & \text{if } -1 \leq \xi \leq 0 \\ 1 - \xi & \text{if } \ 0 \leq \xi \leq 1. \end{cases} \tag{4.10}$$

More generally, the pseudo-wavelets for the multi-scale DOF may be written in terms of the translates and dilates of $\psi(\xi)$ as

$$\psi_k(\xi) = \psi(\tilde{\xi}) \tag{4.11}$$

where

$$\tilde{\xi} = 2^{k-1}(1 + \xi) - 2j - 1, \tag{4.12}$$

and

$$\begin{aligned} 2^{2-k}j - 1 \leq \ \ \xi \ \ &\leq 2^{2-k}j + 2^{1-k} - 1 \\ 2^{2-k}j + 2^{1-k} - 1 \leq \ \ \xi \ \ &\leq 2^{2-k}j + 2^{2-k} - 1. \end{aligned} \tag{4.13}$$

Here k indicates the scale, and j indicates the translates in the element parametric space $(-1 \leq \xi \leq 1)$.

The derivatives of the shape functions yield constant functions that are orthogonal to the derivatives of the pseudo-wavelets at all scales. The derivatives of the pseudo-wavelets yield Haar wavelets as illustrated in Figure 4.9, and at any given scale they are orthogonal with the derivatives at all other scales in the multi-scale element.

The reconstruction algorithm may be viewed as an element-by-element procedure that relies only on the multi-scale information in each element. The reconstruction is shown schematically in Figure 4.9 where the DOF

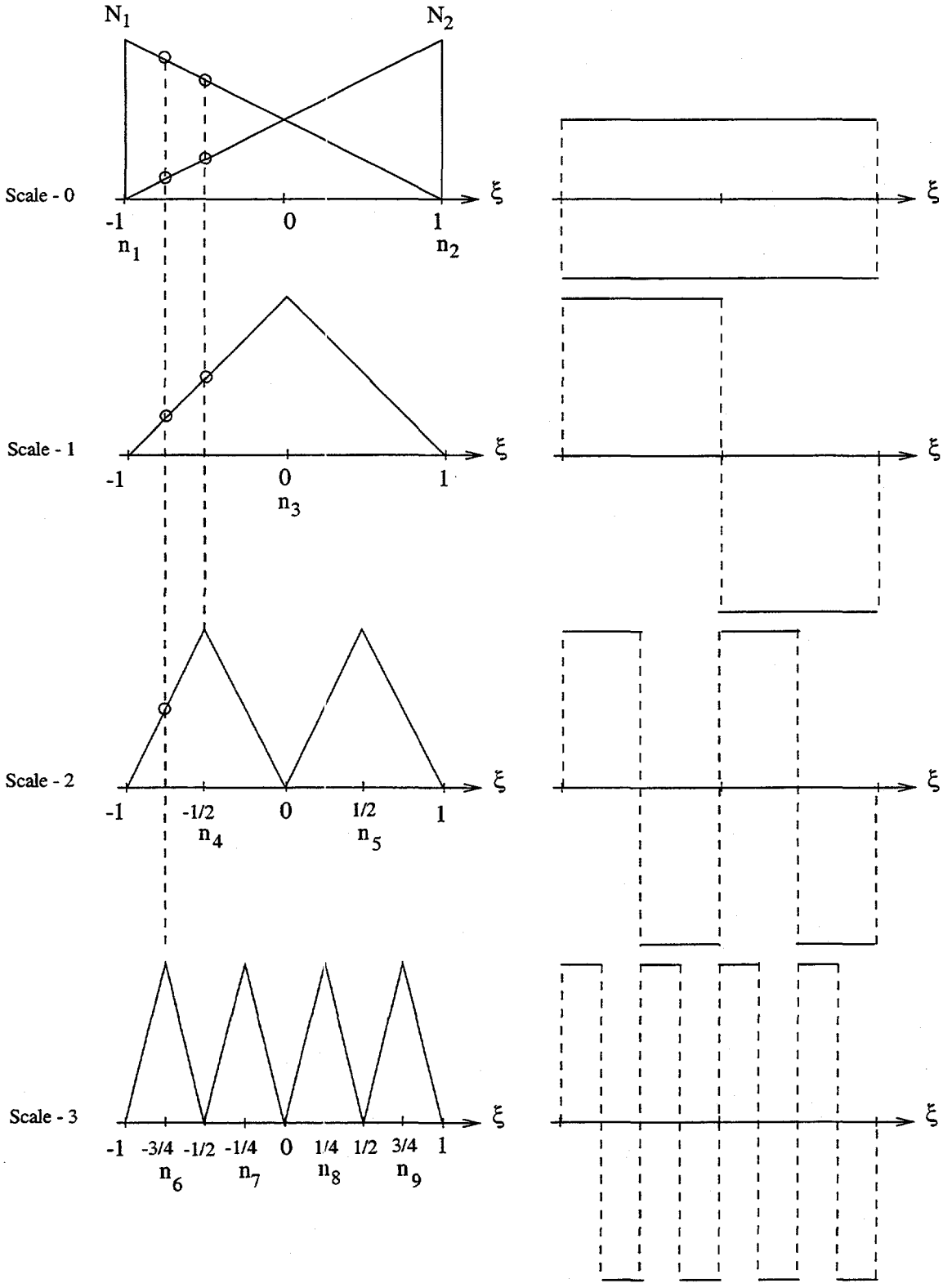

Figure 4.9: Basis elements and their piecewise derivatives for the one dimensional multi-scale element with three refinement scales. The derivatives have been scaled by $1/k$ for scales $k = 1, 2, 3$.

located at $\xi = -3/4$ is computed as a linear combination of the detail corrections, Δu, at scales $0 - 3$. Here, a canonical node-numbering scheme is used where the node numbers are n_1, n_2 at Scale-0, n_3 at Scale-1, n_4, n_5 at Scale-2, etc. as shown in Figure 4.9. That is to say, for $k > 0$, the node numbers are set according to the scale as $2 + 2^{k-1} + j$.

With this numbering scheme, the reconstruction for the DOF located at n_6 may be written as

$$u_6 = N_1 u_0^1 + N_2 u_0^2 + \psi_1^3 \Delta u_1^3 + \psi_2^4 \Delta u_2^4 + \psi_3^6 \Delta u_3^6, \tag{4.14}$$

where each of the basis elements is evaluated at $\xi = -3/4$. Thus, the reconstruction algorithm begins with the interpolant of the coarse-grid solution and injects refinements, or detail, up to the desired scale. The reconstruction may be written more generally as

$$u_k^{2+2^{k-1}+j} = \sum_{i=0}^{Nnpe} N_i u_0^i + \sum_{k=1}^{Nscale} \psi_k^{2+2^{k-1}+j} \Delta u_k^{2+2^{k-1}+j} \tag{4.15}$$

where the basis elements (N_i, and ψ_k) are evaluated at $\xi_{k,j}$ corresponding to the DOF location in the parent element.

The Multi-Scale Operators

The computation of the stiffness for a bilinear operator, $a(u, v)$, is a straightforward procedure that begins with the coarse-grid stiffness.

At the element level, i.e., Scale-0, this is simply

$$K_0^e = \frac{1}{h} \begin{bmatrix} 1 & -1 \\ -1 & 1 \end{bmatrix}, \tag{4.16}$$

where h is the node-spacing for the coarse-grid. Making use of orthogonality, the stiffness entries for the scale DOF, i.e., for $k > 0$, are

$$K_k^{2+2^{k-1}+j} = \frac{2^{k+1}}{h}. \tag{4.17}$$

The resulting element-level stiffness matrix with scale DOF included is

$$K^e = \frac{1}{h}\begin{bmatrix} 1 & -1 & & & & & \\ -1 & 1 & & & & & \\ & & 4 & & & & \\ & & & 8 & & & \\ & & & & 8 & & \\ & & & & & \ddots & \\ & & & & & & 2^{k+1} \end{bmatrix}. \tag{4.18}$$

With this form of the element stiffness, only the coarse-scale terms contribute to the element assembly procedure since all internal DOF simply require a point evaluation and do not rely on information outside the element.

The mass matrix computation is somewhat more involved because it requires the calculation of inner-products that involve the basis elements across scale. The computation of the multi-scale mass matrix consists of the following

$$\begin{aligned} M_0^e &= \int_\Omega^e N_i N_j d\Omega \\ M_{01} &= \int_\Omega^e N_i \psi_1 d\Omega \\ M_{10} &= \int_\Omega^e \psi_1 N_j d\Omega \\ M_{12} &= \int_\Omega^e \psi_1 \psi_2 d\Omega \\ &\vdots \end{aligned} \tag{4.19}$$

This series of element-level integrals leads to the finger-diagonal matrix structure described in the previous sections of this chapter. Figure 4.10 shows the composite finger diagonal structure with the inset coarse-grid element mass matrix.

The row-column lumping procedure is shown schematically in Figure 4.10 for the multi-scale DOF at n_7 in the element. Note that the traditional row-sum lumping for the coarse-grid mass matrix can be used for the nodes corresponding to the coarse-grid, but this type of mass lumping has not been effective for the multi-scale DOF in the element.

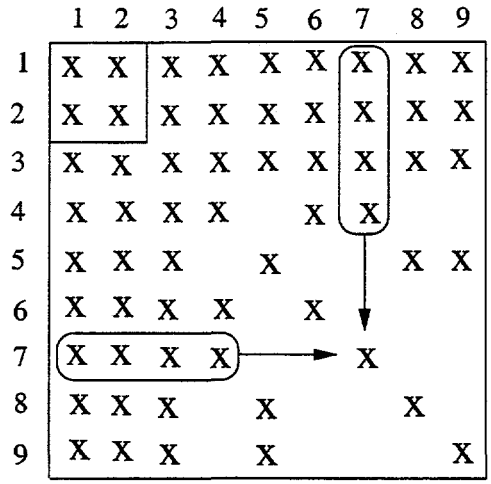

Figure 4.10: Finger diagonal structure of element mass matrix.

4.3.3 A Multi-Scale Algorithm

The application of the one-dimensional multi-scale finite element with the row-column mass lumping lends itself to the following adaptive solution strategy.

Algorithm 2 *Multi-Scale Solution Algorithm*

1. *Form the coarse-grid operators, M_0, and K_0, and solve the coarse-grid problem.*

2. *For each element, inject one scale DOF and solve for the wavelet coefficient, Δu_1. Here, the row-column mass lumping is used to permit point evaluation of the scale solution.*

$$\Delta u_k = [M_k + \alpha K_k]^{-1} F_k \tag{4.20}$$

3. *Compute the termination measure for the scale DOF injection. One possibility for the termination measure relies on stopping when the scale DOF are small relative to the overall solution. (Other stopping criteria have not been investigated.)*

$$\epsilon = \frac{\Delta u_k^{2+2^{k-1}+j}}{\|u_k\|} \tag{4.21}$$

4. *Repeat 1 – 3 until ϵ is smaller than some user-specified criteria.*

5. *Perform the element-by-element multi-scale reconstruction using Eq. (4.15).*

4.3.4 Example 1-D Calculation

As an example of the multi-level algorithm, consider the following problem.

$$-u''(x) = 1 \text{ on } [0,1], \tag{4.22}$$

with essential boundary conditions

$$u(0) = 0,\ u(1) = 0. \tag{4.23}$$

In this example, three scale solutions were computed. Scale-0 corresponds to the coarse-grid solution using two elements. Scale-1 corresponds to the injection of one multi-scale DOF per element, while Scale-2 corresponds to the injection of two multi-scale DOF per element. This may be seen in Figure 4.11 where the multi-scale DOF are shown relative to the elements (e_1, e_2) of the one-dimensional grid.

In this example, the multi-scale DOF for $k = 1$ correspond to $\Delta u_1^4 = \Delta u_1^5 = 1/32$. For $k = 2$, the multi-scale solution consists of $\Delta u_2^6 = \Delta u_2^9 = 1/128$, and $\Delta u_2^7 = \Delta u_2^8 = 1/128$. After the reconstruction procedure, the scale DOF yield solution values that interpolate the exact solution – a result that is expected for linear problems. Similar results have been obtained for problems with non-linear source terms, and for problems with inhomogeneous essential and natural boundary conditions.

Remark 9 *The algorithm presented for the 1-D multi-scale element possesses the property that all scale injection relies only on element-local data and does not require a re-solve of the coarse-grid problem to improve the solution. For problems that are mass-matrix dominated, the correction procedure outlined earlier in this chapter may be required when the row-column lumped mass is used.*

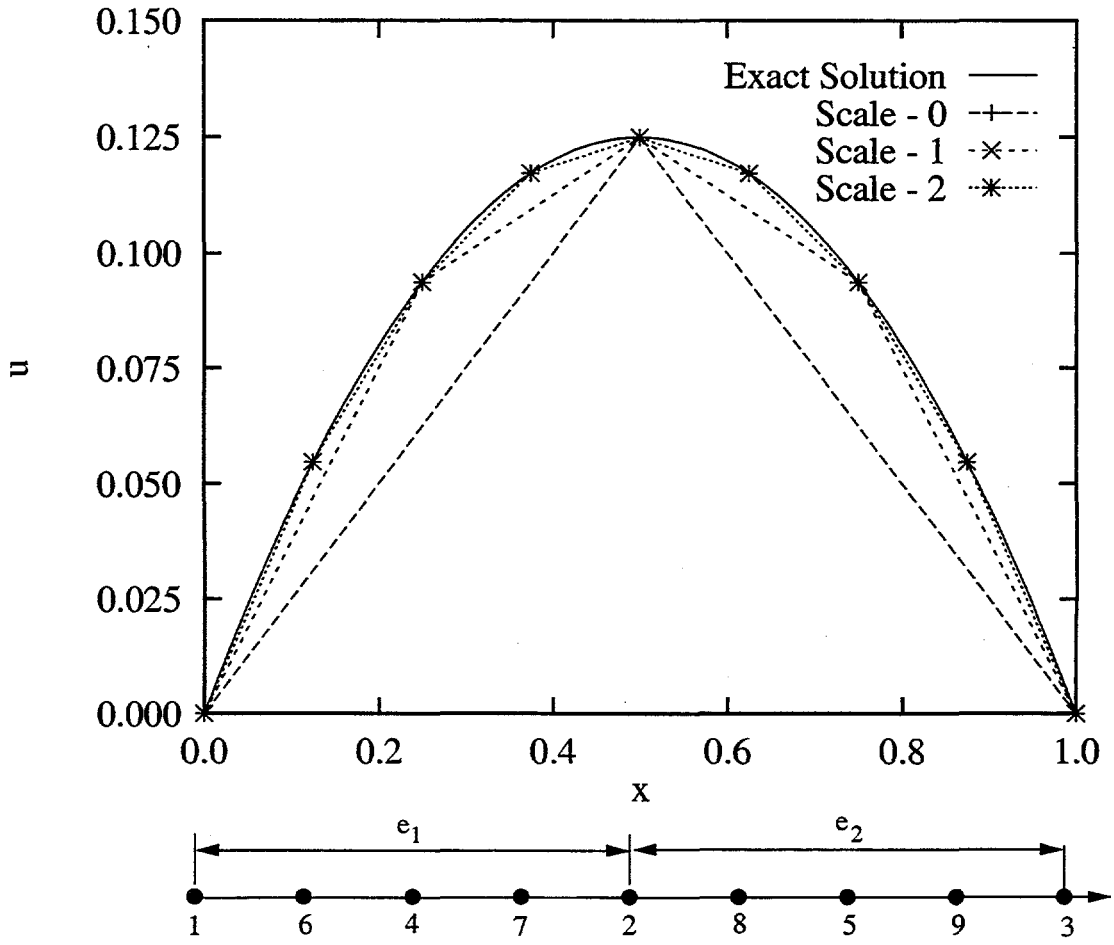

Figure 4.11: Exact solution and scale solutions for $k = 0, 1, 2$. (Node numbers correspond to the insertion of multi-scale DOF).

4.3.5 Two-Dimensional Element

Attention is now turned to the 2-D multi-scale element. As in the 1-D case, the 2-D bilinear element provides the element-level components of the global basis functions. However, the two-dimensional case is somewhat more complicated.

To begin, Figure 4.12 shows a four-patch of bilinear finite elements with the injected multi-scale DOF corresponding to $k = 1$. As in the 1-D element, the shape functions are treated as $k = 0$ and associated with the coarsest grid resolution. The configuration of the multi-scale DOF in the parent element is shown in Figure 4.13. Like the shape functions, the components of the pseudo-wavelets at the element level take on a value of 1 at the DOF location, and they are zero at all other node locations. Only one of the multi-scale DOF is completely supported in the two-dimensional element.

The shape functions for the 2-D bilinear element are

$$N_i = \frac{1}{4}(1 + \xi_i\xi)(1 + \eta_i\eta), \tag{4.24}$$

where $i = 1, 2, 3, 4$, and $-1 \leq \xi, \eta \leq 1$. At the first scale, $k = 1$, the pseudo-wavelets are

$$\begin{aligned} \psi_1^5 &= (1 - |\xi|)(1 - |\eta|) \\ \psi_1^6 &= \frac{1}{2}(1 + \xi)(1 - |\eta|) \\ \psi_1^7 &= \frac{1}{2}(1 - |\xi|)(1 + \eta) \\ \psi_1^8 &= \frac{1}{2}(1 - \xi)(1 - |\eta|) \\ \psi_1^9 &= \frac{1}{2}(1 - |\xi|)(1 - \eta). \end{aligned} \tag{4.25}$$

In a more general way, the pseudo-wavelets for the multi-scale DOF may be written in terms of the translates and dilates of the basis functions at scale $k = 1$. The pseudo-wavelets in two-dimensions are

$$\psi_k^m(\xi, \eta) = \psi_1^m(\tilde{\xi}, \tilde{\eta}), \tag{4.26}$$

where

$$\begin{aligned} \tilde{\xi} &= 2^{k-1}(1 + \xi) - 2j - 1 \\ \tilde{\eta} &= 2^{k-1}(1 + \eta) - 2j - 1, \end{aligned} \tag{4.27}$$

and

$$\begin{array}{rcl} 0 \leq & j & \leq k-1 \\ 2^{2-k}j-1 \leq & \tilde{\xi} & \leq 2^{2-k}j+2^{2-k}-1 \\ 2^{2-k}j-1 \leq & \tilde{\eta} & \leq 2^{2-k}j+2^{2-k}-1. \end{array} \tag{4.28}$$

Here k indicates the scale, j indicates the translates in the element parametric space ($-1 \leq \xi, \eta \leq 1$), and $m = 5, 6, 7, 8, 9$ for the element-local numbering of the pseudo-wavelets. With the basis elements defined this way, the use of recursion at the element level can be used to automate the computation of the mass and stiffness operators with a given scale of resolution, $Nscale$. This type of recursion is illustrated in Figure 4.12.

The performance of the 2-D Schauder basis was presented relative to the bilinear element in §4.2.3. However several key points are re-iterated here. First, the orthogonality of derivatives of the pseudo-wavelets between scales is not preserved in two dimensions – even on an orthogonal grid. The finger-diagonal matrices that arise from this discretization lead to extreme storage costs if the matrices are used without row-column lumping procedures. However, the row-column lumping can be applied to both the mass and stiffness operators, albeit only for the rows and columns corresponding to the multi-scale DOF. In addition, the 2-D multi-scale element is compatible with many h-adaptivity strategies being implemented in finite element codes, and the ability to use this element as a change-of-basis preconditioner is just beginning to be explored.

Remark 10 *The numerical performance of the 1-D and 2-D multi-scale element is identical to the bilinear element since any multi-scale solution can be cast in terms of the reconstructed solution in the finite element basis at the finest grid scale.*

4.4 Summary

The use of a Schauder basis in 1-D and 2-D has been considered with an emphasis on the stability of the basis. In terms of stability, the finite element basis is uniformly stable in L^2, but it is not stable in H^1. In contrast, the Schauder basis is uniformly stable in H^1, but it is not stable in L^2. For the purely elliptic problems, the Schauder basis is a good choice in terms of a lower computational cost with respect to a traditional nodal basis. However,

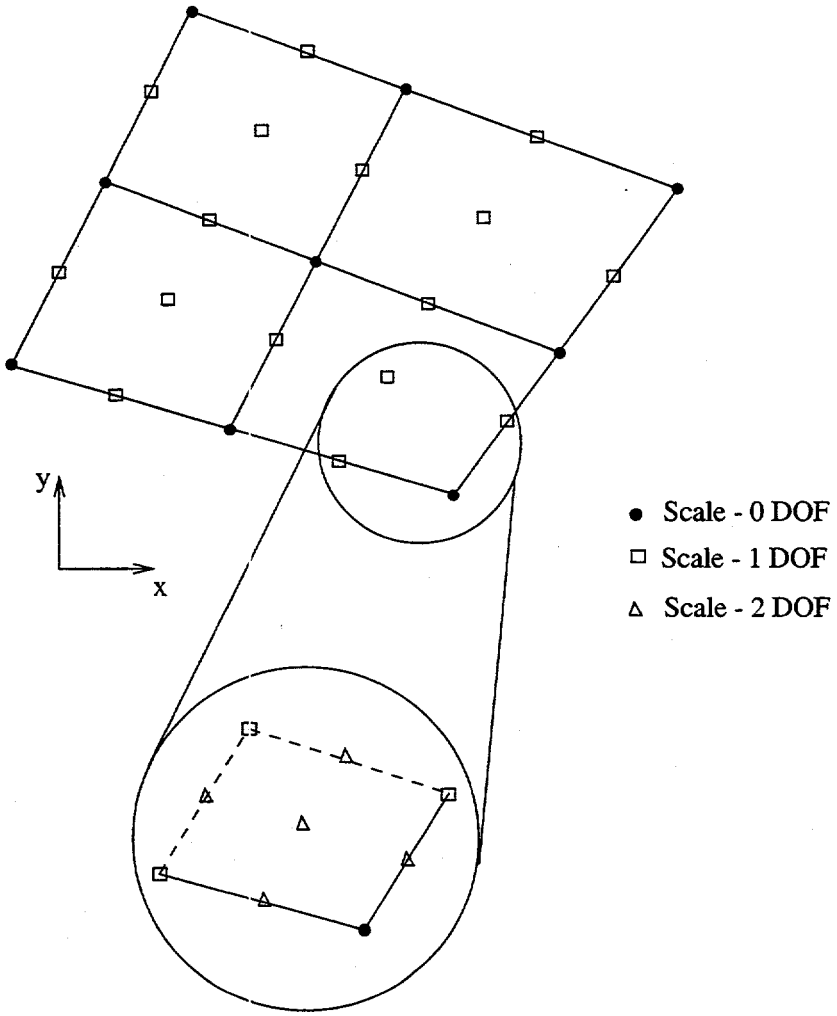

Figure 4.12: Four-patch of bilinear elements with multi-scale DOF.

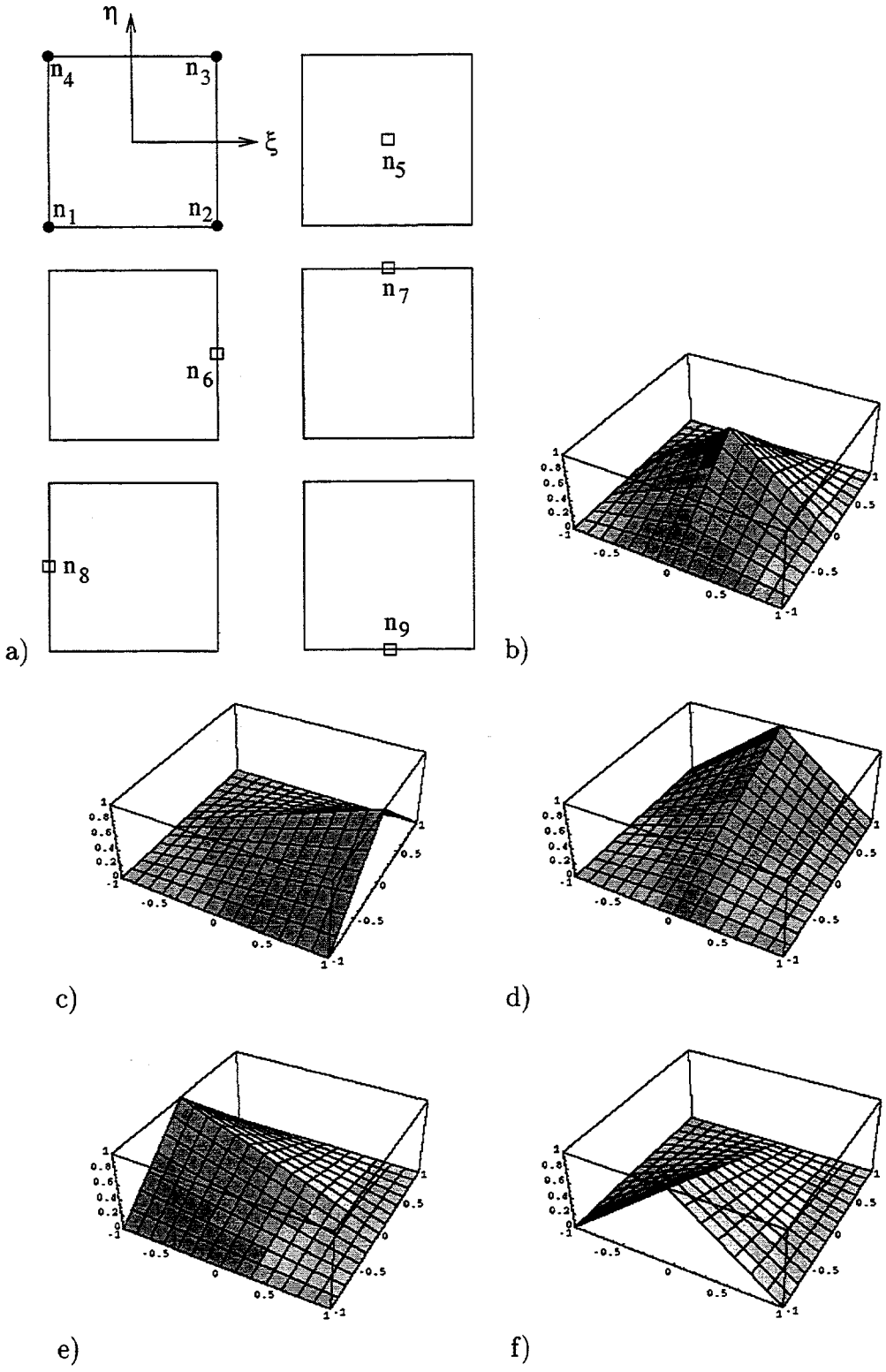

Figure 4.13: Parent element and multi-scale DOF for $k = 1$. a) reference element and basis elements for multi-scale DOF with $k = 1$, b) ψ_1^5, c) ψ_1^6, d) ψ_1^7, e) ψ_1^8, and f) ψ_1^9.

the benefit does not occur until the mesh resolution exceeds 10^5 degrees-of-freedom when the finger-diagonal form of the stiffness operator is used. The benefit of the preconditioning of the Schauder basis is not realized for the $M_k^{2d} + \epsilon K_k^{2d}$ case until the mesh resolution exceeds 10^8 grid points. However, the use of the row-column lumping procedure may be applied to both the multi-scale mass and stiffness operators yielding a solution algorithm that relies on a predictor with a simple vector divide. The 1-D and 2-D multi-scale elements provide a simple mechanism for implementing the Schauder basis in an existing code, albeit with extensions for the insertion of scale degrees-of-freedom. Although only uniform refinement at the element level was presented here, there is no restriction on the spacing of scale DOF in the multi-scale element.

Chapter 5

Reproducing Kernel Methods

The Reproducing Kernel Particle Method (RKPM) has many attractive properties that make it ideal for treating a broad class of physical problems. RKPM may be implemented in a "mesh-full" or a "mesh-free" manner and provides the ability to tune the method, via the selection of a window function and its associated dilation parameter, in order to achieve the requisite numerical performance. In RKPM, the dilation parameter plays a role similar to the dilation parameter in a scaling function although its implementation is somewhat different from traditional scaling functions that satisfy a two-scale difference relationship. RKPM also provides a framework for performing hierarchical computations making it an ideal candidate for simulating multi-scale problems. Although the method has many appealing attributes, it is quite new and its numerical performance is still being quantified with respect to more traditional discretization techniques.

In order to assess the numerical performance of RKPM, detailed studies of the method on a series of model partial differential equations has been undertaken. The results of von Neumann analyses for RKPM semi-discretizations of one and two-dimensional, first and second-order wave equations are presented in the form of phase and group errors. Excellent dispersion characteristics are found for the consistent mass matrix with the proper choice of dilation parameter. In contrast, row-sum lumping the mass matrix is demonstrated to introduce severe lagging phase errors. A "higher-order" mass matrix improves the dispersion characteristics relative to the lumped mass matrix but also yields significant lagging phase errors relative to the fully integrated, consistent mass matrix.

5.1 Formulation

This section begins with a brief overview of the reproducing kernel particle formulation. A detailed presentation of RKPM may be found in the work by Liu et al.[17,18,55,62–73,96] Following the overview is a derivation of the formulae for computing the normalized phase and group speed associated with semi-discretizations of the model hyperbolic partial differential equations.

5.1.1 Reproducing Kernel Particle Formulation

For the sake of clarity, the following overview is limited to one spatial dimension although the formulation may be easily extended to higher dimensions.[17,67,68] The RKPM formulation begins with the notion of a kernel approximation of a function, U, on a domain, Ω,

$$U^R(x) = \int_\Omega U(\xi)\varphi(x-\xi)d\xi, \tag{5.1}$$

where φ is the kernel function and U^R is the continuous approximation to U.[67,71] In order to address discrete problems, numerical quadrature (i.e., trapezoidal or particle integration) is used to evaluate Eq. (5.1) as

$$U^h(x) = \sum_{i=1}^{Np} d_i\varphi(x-x_i)\Delta x_i, \tag{5.2}$$

where U^h is the discrete analogue of U^R, d_i are the particle coefficients, and Np is the total number of particles in the domain, Ω.[67] In general, the coefficients, d_i, are different from the value of the function at particle i because the RKPM basis is non-nodal, that is, it does not posses the Kronecker-delta property.

One of the most commonly used RKPM kernel functions, and the one used here, is the cubic spline. In one-dimension, the cubic spline kernel function is

$$\varphi(z) = \begin{cases} \frac{2}{3r\Delta x}\left[1-\frac{3}{2}z^2+\frac{3}{4}z^3\right] & z<1 \\ \frac{1}{6r\Delta x}\left[2-z\right]^3 & 1\le z<2, \\ 0 & z\ge 2 \end{cases} \tag{5.3}$$

where $z = |x-x_i|/(r\Delta x)$, x_i is the position of particle i, Δx is the particle spacing, and r is the refinement parameter.[3,67,68] The refinement parameter

controls the dilation of the kernel function, and subsequently, the domain of influence for the function. For example, consider the cubic-spline window function with a uniform particle distribution. In this case, $r = 1/2$ results in support over 3 particles, while $r = 1$ results in support over 5 particles. In this work, the optimal dilation parameter, $r = 1.14$, established by Liu and Chen[65] to minimize aliasing error in terms of energy, is used.

In general, Eq. (5.2) will not exactly reproduce an arbitrary polynomial. The accurate reproduction of polynomials to order p is ensured by introducing a modified window function,

$$\overline{\varphi}(x - x_i) = \sum_{k=0}^{p} \beta_k(x)\varphi(x - x_i)\,(x - x_i)^k, \tag{5.4}$$

where $\beta_k(x)$ represents a set of correction functions that vary within the domain, Ω.[67,68] The modified window function, $\overline{\varphi}$, replaces φ in Eq. (5.2) yielding

$$U^h(x) = \sum_{i=1}^{Np} \overline{\varphi}(x - x_i)d_i\Delta x_i. \tag{5.5}$$

The correction functions are determined by substituting Eq. (5.4) into Eq. (5.5) and requiring that the resulting kernel approximation reproduce polynomials to the desired order. For linear consistency, the following constraints are required,

$$\sum_{i=1}^{Np} \left[\beta_0(x) + \beta_1(x)\,(x - x_i)\right]\varphi(x - x_i)\Delta x_i = 1 \tag{5.6}$$

$$\sum_{i=1}^{Np} \left[\beta_0(x) + \beta_1(x)\,(x - x_i)\right]\varphi(x - x_i)x_i\Delta x_i = x. \tag{5.7}$$

From these equations, $\beta_0(x)$ and $\beta_1(x)$ may be calculated in a point-wise fashion in the domain. With the correction functions in hand, the requisite derivatives for a Bubnov-Galerkin procedure may be computed. Although the calculation of these derivatives is rather straight forward, the algebra required is significant and the reader is directed to the work of Liu et al.[17,67,68] for details.

Remark 11 *As a brief aside, consider the limiting case where the linear "hat function" is used as the kernel function instead of the cubic-spline of*

Eq. (5.3). In this case, the window function is

$$\varphi(z) = \begin{cases} \frac{1-z}{r\Delta x} & z < 1 \\ 0 & z \geq 1 \end{cases} \tag{5.8}$$

If the dilation parameter is unity, then the resulting basis elements are simply the linear finite element functions and yield the usual form of the mass and stiffness operators.

In the ensuing dispersion analysis, tensor products of Eq. (5.3),

$$\tilde{\varphi}\left(\frac{x-x_i}{r\Delta x}, \frac{y-y_j}{r\Delta y}\right) = \varphi\left(\frac{x-x_i}{r\Delta x}\right)\varphi\left(\frac{y-y_j}{r\Delta y}\right), \tag{5.9}$$

are used to generate a two-dimensional kernel function with rectangular support.[3,68] The tensor-product kernel function in Eq. (5.9) is used with bilinear consistency enforced for the two-dimensional dispersion results presented in §5.2.3.

5.1.2 RKPM Two-Scale Decomposition

The use of the RKPM window functions in a multi-resolution analysis is briefly demonstrated in this section. Following the procedure outlined in Chapter 1, the projection of a discrete solution, U^h, onto the subspace, $\mathcal{V}_a$, may be written as

$$\mathcal{P}_a U^h_a = \mathcal{P}_{2a} U^h_{2a} + \mathcal{Q}_{2a} U^h_{2a}, \tag{5.10}$$

where $a = r\Delta x$ is the dilation parameter and relies on the refinement parameter and particle spacing. Here, the projection at scale-a is simply

$$\mathcal{P}_a U^h = \sum_{i=1}^{Np} \overline{\varphi}(x - x_i) U^h_i \Delta x_i. \tag{5.11}$$

The projection, $\mathcal{P}_{2a}$, may be thought of as the providing the representation of the field at twice the scale, or at half the grid resolution. The projection, $\mathcal{Q}_{2a}$, may be viewed as the detail or the "peeled-off" part of $\mathcal{P}_a U^h$.

Unlike the projections discussed in Chapter 1, the RKPM projections are not necessarily idempotent. The wavelets associated with the $\mathcal{Q}$-projection are defined as

$$\bar{\psi}_{2a} = \overline{\varphi}_a - \overline{\varphi}_{2a}. \tag{5.12}$$

Although these wavelets satisfy the property that the first moment is zero, the rigorous enforcement of orthogonality and the satisfaction of a two-scale difference relation has been abandoned.

Example 6 *The two-scale decomposition of a step-function using the "linear hat" function for the window function is shown in Figure 5.1. Here, the grid consists of 11 uniformly spaced particles with* $0 \leq x \leq 1$. *In this case, the original signal was represented on the grid using linear hat functions with* $r = 1$, *i.e.,* $a = \Delta x$. *The coarse scale representation of the original signal is shown with the wavelet projection at scale-2a.*

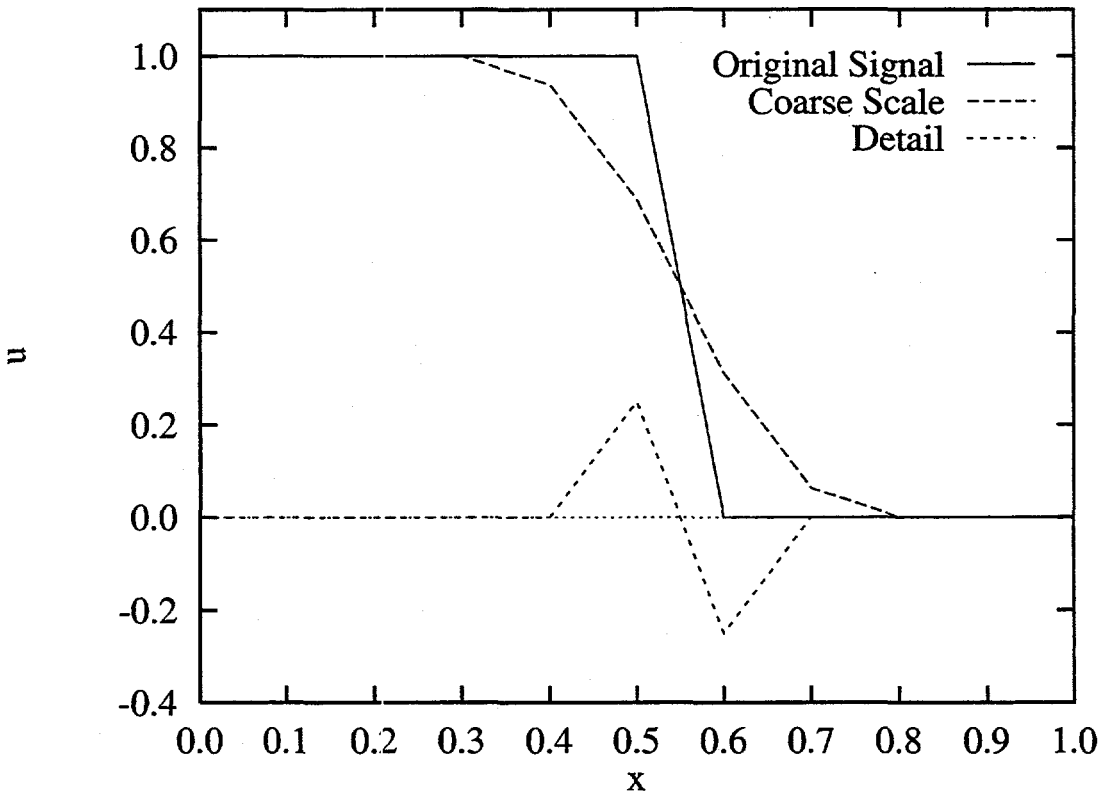

Figure 5.1: One-dimensional two-scale decomposition based on dilation of the window function.

Remark 12 *One interesting and useful aspect of the RKPM two-scale decomposition is that the field at scale-2a may be represented on the original grid. That is, there is no inherent down-sampling of the field that is required making wavelet projection useful for detecting steep gradients automatically.*

5.1.3 von Neumann Analysis

The accurate simulation of wave propagation or advection dominated processes using discrete numerical schemes hinges upon having a clear understanding of the constraining numerical errors, and sufficient computational resources to effect solutions at the requisite grid scale. Examples of this may be seen when attempting to simulate wave propagation in an acoustic medium, or compute turbulent flow fields via direct numerical simulation (DNS) or large eddy simulation (LES). In physical problems with a dominant hyperbolic character, controlling the dispersive errors, i.e., phase and group speed errors, to within 5% can require 8 to 10 grid points per wavelength with traditional finite difference or lumped-mass finite element methods. Thus, the simulation of hyperbolic problems is limited by the wavelength that the grid can accurately represent. Further, a failure to respect the so-called grid Nyquist limit can introduce deleterious aliasing effects that corrupt the simulation fidelity.

In general, the application of discrete methods to hyperbolic partial differential equations can result in solutions that are dispersive even though the physical model for wave propagation is non-dispersive. Dispersion errors are typically characterized by the differences between the apparent, i.e., numerical, phase and group speed of waves and their exact counterparts. Phase and group speed errors represent some of the most constraining numerical errors associated with the simulation of wave propagation and advection dominated flows.

In the context of linear acoustics, the phase speed is the speed at which individual waves propagate. In the absence of dispersion, i.e., for a perfect acoustic fluid, this is simply the sound speed. In a dispersive acoustic medium, the phase speed is a function of the frequency or wavelength of the propagating wave. Thus, phase error may be viewed as a measure of the influence of numerical dispersion on the apparent sound speed relative to the true sound speed.

In contrast to the phase speed, the group speed describes the propagation of wave packets that are comprised of short wavelength signals modulating

a slowly varying, longer wavelength envelope. Because the energy associated with a wave packet travels with the packet, the group speed is often referred to as the "energy" velocity. The group speed is also referred to as the speed of modulation. For a non-dispersive medium the phase and group speed are identical.

In discrete wave propagation problems, the group speed may be used to study and explain the propagation of short wavelength oscillations that are typically $2\Delta x$ in wavelength where Δx is the characteristic mesh spacing. Vichnevetsky[100,101] has demonstrated that spurious $2\Delta x$ oscillations, that are induced by rapid changes in mesh resolution and at physical boundaries, propagate at a group speed associated with a $2\Delta x$ wavelength.

The investigation of the dispersive errors associated with discrete solutions is not new and has been used by numerous researchers to characterize the performance of numerical methods. A brief review of earlier dispersion analyses may be found in Christon.[19] The focus of the current work is upon characterizing the dispersive nature of the reproducing kernel particle method for hyperbolic problems.

With the RKPM formulation outlined, the weak forms of three model partial differential equations (two hyperbolic and one parabolic) are presented along with a description of the Fourier analysis. For generality, the numerical dispersion and diffusion relations are generated for the two-dimensional model equations from which their one-dimensional counterparts are obtained.

The two-dimensional first-order wave, second-order wave and parabolic partial differential equations are, in Cartesian coordinates,

$$\frac{\partial U}{\partial t} + c_x \frac{\partial U}{\partial x} + c_y \frac{\partial U}{\partial y} = 0 \tag{5.13}$$

$$\frac{\partial^2 U}{\partial t^2} - c^2 \left[\frac{\partial^2 U}{\partial x^2} + \frac{\partial^2 U}{\partial y^2} \right] = 0, \tag{5.14}$$

and,

$$\frac{\partial U}{\partial t} - \alpha \left[\frac{\partial^2 U}{\partial x^2} + \frac{\partial^2 U}{\partial y^2} \right] = 0. \tag{5.15}$$

Here t is time, U is the dependent variable, c is the wave speed, $(c_x, c_y) = (c\cos(\theta), c\sin(\theta))$ are the advection velocity components, θ is the wave vector direction measured from the x-axis, and α is the diffusivity.

The semi-discrete forms of Eq. (5.13) through (5.15) are required for the following analysis. The details for obtaining the weak form of these equations

are well known,[51] and are not repeated here. The semi-discrete forms of the first-order wave, second-order wave and parabolic equations are,

$$\mathbf{M}\dot{\mathbf{d}} + \mathbf{A}(c)\,\mathbf{d} = 0, \tag{5.16}$$

$$\mathbf{M}\ddot{\mathbf{d}} + \mathbf{K}(c)\,\mathbf{d} = 0, \tag{5.17}$$

and,

$$\mathbf{M}\dot{\mathbf{d}} + \mathbf{K}(\alpha)\,\mathbf{d} = 0, \tag{5.18}$$

where $\mathbf{A}$ is the advection operator, and $\mathbf{K}$ is the stiffness matrix. The generalized mass matrix is defined as

$$\mathbf{M} = \gamma\mathbf{M}^c + (1-\gamma)\mathbf{M}^l, \tag{5.19}$$

where $\mathbf{M}^c$ and $\mathbf{M}^l$ are the consistent and row-sum-lumped mass matrices respectively, and $0 \leq \gamma \leq 1$ is the lumping parameter.

It should be noted that some form of numerical quadrature is required for the evaluation of $\mathbf{A}$, $\mathbf{K}$ and $\mathbf{M}$ above. This integration may be performed by placing a grid of quadrature points overlaying the nodal points and employing, for instance, Gaussian quadrature. Alternatively the nodal points can themselves be used as the quadrature points with the appropriate weight being the variational volume associated with the node (termed trapezoidal integration here). Both integration techniques and their effects on the discretization errors are considered.

Proceeding with the Fourier analysis, a plane wave solution is placed on an infinite span (alternatively, on a finite domain with periodic boundary conditions) in order to compare the exact and semi-discrete solutions. It can be shown that the particle values, $\mathbf{U}^h$, satisfy the same evolution equations as the coefficients, $\mathbf{d}$, when a periodic domain and symmetric window functions are used.[101] Thus, Eq. (5.16) and (5.17) may be rewritten in terms of $\mathbf{U}^h$ for the purposes of this analysis, and the plane wave solution to Eq. (5.13) and (5.14) may be expressed as

$$U(x,y,t) = U_0 \exp[\iota k(x\cos(\theta) + y\sin(\theta)) - \iota\omega t]. \tag{5.20}$$

Here, U_0 is the amplitude, k is the wave number, θ is the propagation direction of a plane wave measured from the x-axis, and $\iota = \sqrt{-1}$.

For the parabolic equation, Eq. (5.15), the particle values also satisfy the same evolution equation as the particle coefficients, $\mathbf{d}$, and so the periodic solution to the parabolic equation is

$$U(x,y,t) = U_0(x,y)\exp[-\alpha k^2 t]. \tag{5.21}$$

Remark 13 *The use of the term "von Neumann" analysis for the parabolic equation is somewhat misleading because the partial differential equation does not admit wave solutions under ordinary circumstances (although the authors are aware of a hyperbolic theory for heat conduction). Instead, the interpretation relies on consideration of the fact that the diffusivity is now a function of wavelength, i.e., $\alpha = \alpha(\lambda)$. With this in mind, for each wavelength, i.e., Fourier mode, there is an associated diffusivity. Thus, the analogue to dispersion error for the hyperbolic equations is the observation that the wavelength dependent rate of diffusion leads to errors in the overall rate of diffusion.*

Now, considering a mesh with nodes equally spaced at intervals of Δx and Δy, any node $(i+m, j+n)$ at coordinates (x_{i+m}, y_{j+n}) may be located relative any other node (i,j) as $x_{i+m} = x_i + m\Delta x$ and $y_{j+n} = y_j + n\Delta y$. Thus, solutions to the semi-discrete hyperbolic and parabolic equations are,

$$U_{i+m,j+n} = U_0(x_i, y_j) \exp[ik(m\Delta x \cos\theta + n\Delta y \sin\theta)] \exp[-i\omega t] \tag{5.22}$$

and,

$$U_{i+m,j+n} = U_0(x_i, y_j) \exp[ik(m\Delta x \cos\theta + n\Delta y \sin\theta)] \exp[-\alpha k^2 t], \tag{5.23}$$

respectively.

Given an arbitrarily wide kernel function, the semi-discrete forms of the first and second-order wave and parabolic equations for node (i,j) are

$$\sum_{l=-n}^{n} \sum_{m=-n}^{n} \left\{ M_{(i,j),(i+l,j+m)} \dot{U}_{i+l,j+m} + A_{(i,j),(i+l,j+m)} U_{i+l,j+m} \right\} = 0, \tag{5.24}$$

$$\sum_{l=-n}^{n} \sum_{m=-n}^{n} \left[M_{(i,j),(i+l,j+m)} \ddot{U}_{i+l,j+m} + K_{(i,j),(i+l,j+m)} U_{i+l,j+m} \right] = 0, \tag{5.25}$$

and,

$$\sum_{l=-n}^{n} \sum_{m=-n}^{n} \left[M_{(i,j),(i+l,j+m)} \dot{U}_{i+l,j+m} + K_{(i,j),(i+l,j+m)} U_{i+l,j+m} \right] = 0, \tag{5.26}$$

respectively. In Eq. (5.24) through (5.26), $M_{(i,j),(p,q)}$, $K_{(i,j),(p,q)}$ and $A_{(i,j),(p,q)}$ are the mass, stiffness and advection matrix entries on the row associated with node (i,j) and the column associated with node (p,q) on a natural ordered Cartesian grid.

Substituting the appropriate forms of Eq. (5.22) and (5.23) into Eq. (5.24) through (5.26) and canceling terms yields,

$$-i\omega \sum_{l=-n}^{n} \sum_{m=-n}^{n} [M_{(i,j),(i+l,j+m)} \exp(ik(l\Delta x \cos(\theta) + m\Delta y \sin(\theta)))] + \sum_{l=-n}^{n} \sum_{m=-n}^{n} A_{(i,j),(i+l,j+m)} \exp(ik(l\Delta x \cos(\theta) + m\Delta y \sin(\theta))) = 0 \quad (5.27)$$

and,

$$-\omega^2 \sum_{l=-n}^{n} \sum_{m=-n}^{n} [M_{(i,j),(i+l,j+m)} \exp(ik(l\Delta x \cos(\theta) + m\Delta y \sin(\theta)))] + \sum_{l=-n}^{n} \sum_{m=-n}^{n} [K_{(i,j),(i+l,j+m)} \exp(ik(l\Delta x \cos(\theta) + m\Delta y \sin(\theta)))] = 0 \quad (5.28)$$

for the first and second-order wave equations and

$$-\alpha k^2 \sum_{l=-n}^{n} \sum_{m=-n}^{n} [M_{(i,j),(i+l,j+m)} \exp(ik(l\Delta x \cos(\theta) + m\Delta y \sin(\theta)))] + \sum_{l=-n}^{n} \sum_{m=-n}^{n} [K_{(i,j),(i+l,j+m)} \exp(ik(l\Delta x \cos(\theta) + m\Delta y \sin(\theta)))] = 0 \quad (5.29)$$

for the parabolic PDE. The computation of the normalized phase and group speed for the hyperbolic problems proceeds by solving for the circular frequency, ω, and making use of Eq. (5.20). The normalized phase speed associated with either semi-discrete equation is $\psi = \overline{c}/c$ where $\overline{c}$ is the apparent phase speed. Rearranging Eq. (5.27) and (5.28) yields

$$\psi_1 = \frac{1}{ick} \frac{\sum_{l=-n}^{n} \sum_{m=-n}^{n} [A_{(i,j),(i+l,j+m)} \exp(ik(l\Delta x \cos(\theta) + m\Delta y \sin(\theta)))]}{\sum_{l=-n}^{n} \sum_{m=-n}^{n} [M_{(i,j),(i+l,j+m)} \exp(ik(l\Delta x \cos(\theta) + m\Delta y \sin(\theta)))]} \quad (5.30)$$

for the first-order wave equation, and

$$\psi_2 = \frac{1}{ck} \sqrt{\frac{\sum_{l=-n}^{n} \sum_{m=-n}^{n} [K_{(i,j),(i+l,j+m)} \exp(ik(l\Delta x \cos(\theta) + m\Delta y \sin(\theta)))]}{\sum_{l=-n}^{n} \sum_{m=-n}^{n} [M_{(i,j),(i+l,j+m)} \exp(ik(l\Delta x \cos(\theta) + m\Delta y \sin(\theta)))]}} \quad (5.31)$$

for the second-order wave equation.

The appropriate error measure which arises for the parabolic PDE is the normalized apparent diffusivity, $\overline{\alpha}/\alpha$. Rearranging Eq. (5.29) yields

$$\overline{\alpha}/\alpha = \frac{1}{\alpha k^2} \frac{\sum_{l=-n}^{n} \sum_{m=-n}^{n} [K_{(i,j),(i+l,j+m)} \exp(ik(l\Delta x \cos(\theta) + m\Delta y \sin(\theta)))]}{\sum_{l=-n}^{n} \sum_{m=-n}^{n} [M_{(i,j),(i+l,j+m)} \exp(ik(l\Delta x \cos(\theta) + m\Delta y \sin(\theta)))]}. \tag{5.32}$$

The one-dimensional apparent dispersion and diffusion characteristics may be obtained from the two-dimensional relations results by setting $\theta = 0$ yielding,

$$\psi_1 = \frac{f_a}{ckf_m}, \tag{5.33}$$

$$\psi_2 = \frac{1}{ck}\sqrt{\frac{f_k}{f_m}} \tag{5.34}$$

and,

$$\overline{\alpha}/\alpha = \frac{1}{\alpha k^2}\frac{f_k}{f_m} \tag{5.35}$$

for the apparent phase speed, group speed and diffusivity respectively where,

$$f_a = A_{i,i} + 2\sum_{l=1}^{n} \sin(kl\Delta x) A_{i,i+l} \tag{5.36}$$

$$f_m = M_{i,i} + 2\sum_{l=1}^{n} \cos(kl\Delta x) M_{i,i+l}, \tag{5.37}$$

and

$$f_k = K_{i,i} + 2\sum_{l=1}^{n} \cos(kl\Delta x) K_{i,i+l}. \tag{5.38}$$

The normalized group speed, in one-dimension, is defined as $\zeta = v_g/c$, where $v_g = \partial\omega/\partial k$. Consideration of the normalized group velocity for the two-dimensional, semi-discretizations introduces significant complexities that make such analysis beyond the scope of this work.

Using Eq. (5.33) and (5.34), the normalized group speed in one-dimension is

$$\zeta_1 = \frac{g_a f_m - f_a g_m}{c f_m^2}, \tag{5.39}$$

and

$$\zeta_2 = \frac{\sqrt{f_m}}{2c\sqrt{f_k}} \frac{g_k f_m - f_k g_m}{f_m^2} \tag{5.40}$$

for the first and second-order wave equations respectively. Here,

$$g_a = \partial f_a / \partial k = 2\Delta x \sum_{l=1}^{n} l \cos(kl\Delta x) A_{i,i+l} \tag{5.41}$$

$$g_m = \partial f_m / \partial k = -2\Delta x \sum_{l=1}^{n} l \sin(kl\Delta x) M_{i,i+l}, \tag{5.42}$$

and

$$g_k = \partial f_k / \partial k = -2\Delta x \sum_{l=1}^{n} l \sin(kl\Delta x) K_{i,i+l}. \tag{5.43}$$

Unless otherwise noted, the normalized phase and group speed defined above are referred to simply as phase speed and group speed in the remaining text.

Remark 14 *There have been no restrictions (other than symmetry) placed on the form or type of basis functions used to obtain the mass, stiffness or advection operators. Thus, Eq. (5.30) through (5.40) are equally valid for Galerkin formulations that use the RKPM functions or finite element basis functions.*

5.2 Results

This section summarizes the results of the von Neumann analyses in terms of phase and group speed for RKPM semi-discretizations of the one-dimensional model hyperbolic equations followed by phase speed associated with the two-dimensional equations, and a brief discussion of the analysis for the parabolic equation. Unless otherwise noted, the normalized phase and group speeds defined in the previous section are referred to simply as phase and group speed in the remaining text. Both the one and two-dimensional RKPM formulations use the cubic spline kernel function in Eq.(5.3). Further, the two dimensional formulation uses the tensor product in Eq. (5.9) to produce a two dimensional kernel function. Both spatial formulations use the procedure outlined in §5.1.1 to generate modified window functions that ensure linear ($U(x) = 1 + x$; one-dimensional) and bi-linear ($U(x, y) = 1 + x + y + xy$; two-dimensional) functions are reproduced exactly.

For the purpose of comparison, results are presented for linear and bi-linear finite element (FE) semi-discretizations. Here, the linear and bi-linear finite element basis functions were chosen for comparison as they provide the

same order of consistency as the RKPM discretizations considered. The FE phase and group speed are calculated using the formulae presented in Section 2.2 with linear finite element basis functions.

In the discussion that follows, the phase and group speed results are presented as functions of non-dimensional wave number, $k\Delta x/\pi = 2\Delta x/\lambda$. In order to simplify the discussion, the following nomenclature has been adopted to identify the the mass matrix and quadrature rule used for both the FE and RKPM results. The mass matrix is identified as C for consistent ($\gamma = 1$), L lumped ($\gamma = 0$), or H higher-order ($\gamma = 1/2$); cf. Eq. (5.19). The numerical integration scheme is identified as either F indicating full Gauss quadrature, or T indicating a trapezoidal rule, i.e., particle integration.

The F nomenclature for "full Gauss quadrature" indicates a 2×2 quadrature rule for the bi-linear finite element and a 4×4 quadrature rule for the RKPM formulation. In the case of the RKPM formulation, the sensitivity of the matrix entries with respect to the quadrature rule was tested and demonstrated that the entries did not change appreciably with increased number of quadrature points beyond 4×4. For trapezoidal (particle) integration, the particle locations are used as quadrature points. Here, the motivation for consideration of particle integration is the potential reduction in computational complexity gained by elimination of the background integration mesh which also results in a truly mesh-free method.

5.2.1 1-D Hyperbolic Equations

In this section, the phase and group speed for the semi-discrete, one-dimensional, first and second-order wave equations are presented.

First-Order Wave Equation

Phase and group speed for the linear finite element semi-discretizations of the first-order wave equation are presented in Figure 5.2. Results are plotted for fully integrated, consistent (CF), lumped (LF) and higher-order (HF) mass matrix formulations. As shown, the FE formulations introduce strictly lagging phase speed for all wavelengths considered with the CF formulation delivering smaller phase errors up to the $2\Delta x$ limit. All three mass matrices result in a phase speed of zero at $2\Delta x/\lambda = 1$, i.e., wavelengths of $2\Delta x$ are stationary on the grid.

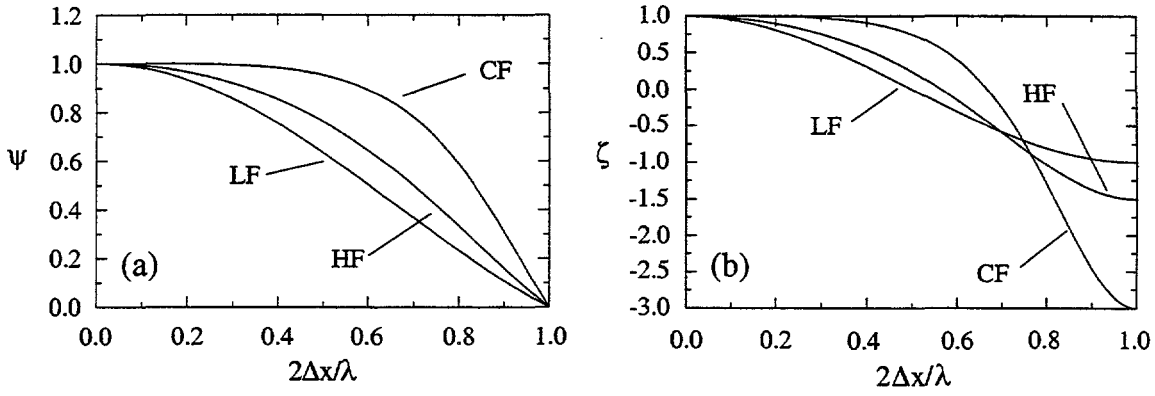

Figure 5.2: One-dimensional phase (a) and group (b) speed results for the first-order wave equation, linear finite element semi-discretization employing fully integrated, consistent (CF), lumped (LF) mass and higher-order (HF) matrix formulations.

The finite element discretizations also yield strictly lagging group speed for all three mass matrices. However, the lumped mass matrix yields a zero group speed for $4\Delta x$ wavelengths while both the CF and HF mass matrices have zero group speed at shorter wavelengths. The CF formulation performs better than the LF and HF formulations, i.e., yields smaller group errors for $\lambda \geq 3\Delta x$. All three formulations yield negative group speeds for short wavelengths indicating that the energy associated with $2\Delta x$ wavelength signals propagates in the opposite direction of the longer wavelength signals. Surprisingly, the LF formulation yields the smallest, albeit still negative, group speed in the limit of $2\Delta x$ wavelengths.

Figure 5.3 shows the phase and group speed for the one-dimensional RKPM semi-discretizations of the first-order wave equation. Again, fully integrated consistent (CF), lumped (LF) and higher-order (HF) mass matrix formulations are presented. In addition, results are shown for the consistent mass matrix formulation with particle integration of the advection and mass matrices (CT). As with the FE results in Figure 5.2, the RKPM method introduces lagging phase errors over the discrete spectrum of wavelengths. The consistent mass (CF) formulation performs the best and delivers significantly better phase speed relative to the FE results presented in Figure 5.2. In order to quantify the increased performance of the RKPM-CF method, consider a phase error, $\epsilon = |1 - \psi|$, of 5% or less to be appropriate for engineering purposes. For the FE-CF method, this criterion corresponds to $4\Delta x$ or 5 grid-points per wavelength. In contrast, the RKPM-CF and CT

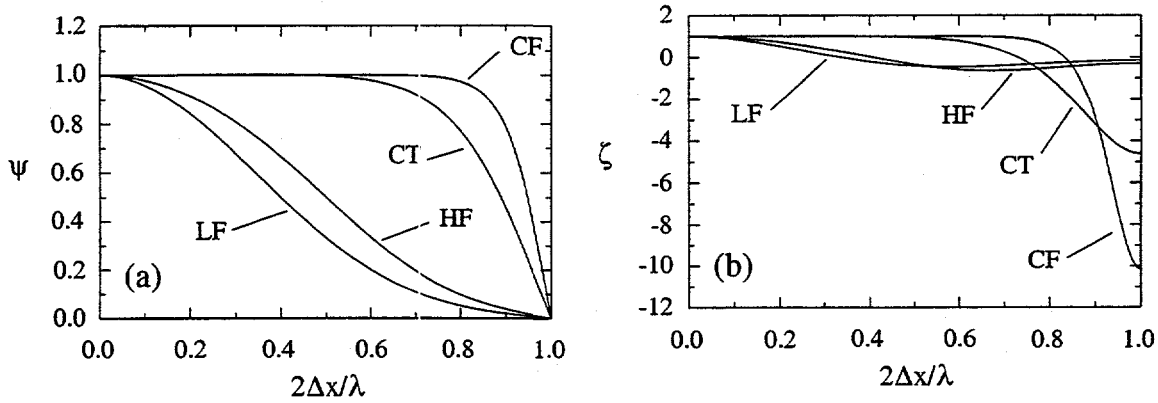

Figure 5.3: One-dimensional phase (a) and group (b) speed results for the first-order wave equation. Reproducing Kernel Particle semi-discretization employing full-integration consistent (CF), lumped (LF), higher-order (HF) and trapezoidal integration consistent (CT) mass matrix formulations.

methods require $2-3\Delta x$, or approximately $3-4$ particles per wavelength. While both the RKPM-CF and CT methods perform quite well, the lumped and higher-order formulations introduce severe lagging phase errors relative to their finite element counterparts.

In terms of the group speed, both the RKPM-CT and CF formulations are far superior to the LF and HF formulations. Similar to the phase speed, the CT formulation yields lagging group errors at longer wavelengths than the CF formulation. However, the trapezoidal mass matrix, CT, avoids the large negative group speed associated with the fully-integrated, CF, matrix at $2\Delta x$ wavelengths. Both the FE-CF and RKPM-CT formulations yield negative group speed for wavelengths shorter than $3\Delta x$, while the RKPM-CF formulation produces negative group speed for wavelengths shorter than about $2.5\Delta x$. However, the group error associated with $2\Delta x$ wavelengths for the RKPM-CF formulation is over 3 times larger than for the FE-CF case and is 10 times larger than the sound speed. From these results it is apparent that the RKPM-CT and CF formulations exhibit very good dispersive behavior, discounting the large negative group speed for the RKPM-CF case, with consistency identical to the finite element formulation.

Second-Order Wave Equation

Phase and group speeds for the linear finite element semi-discretizations of the second-order wave equation are presented in Figure 5.4 for the fully inte-

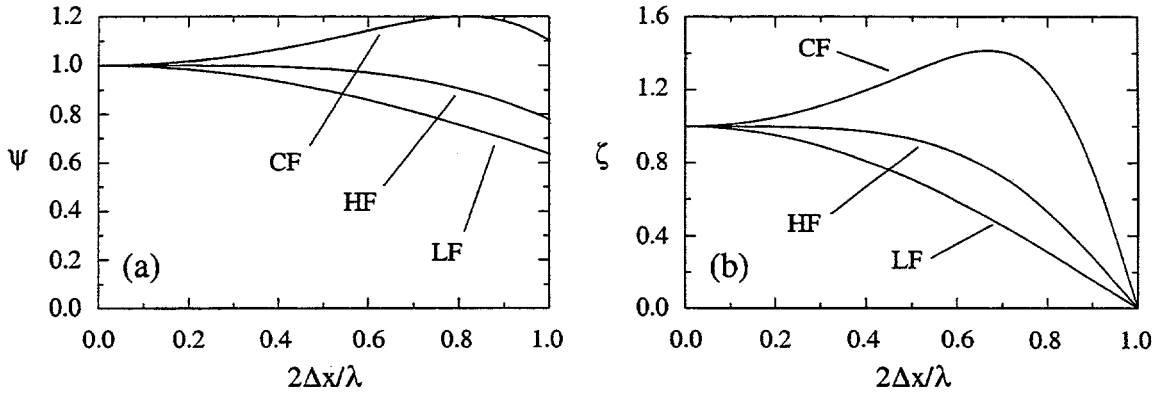

Figure 5.4: One-dimensional phase (a) and group (b) speed results for the second-order wave equation, linear finite element semi-discretization employing full-integration consistent (CF), lumped (LF) and higher-order (HF) mass matrix formulations.

grated, consistent, lumped and higher-order mass matrix formulations. The consistent mass formulation (CF) introduces leading phase errors while the lumped (LF) and higher-order (HF) methods exhibit strictly lagging phase errors. Additionally, both the LF and HF methods demonstrate lagging group speed for all wavelengths considered while the CF group speed is leading for $2\Delta x/\lambda \leq 0.85$.

Figure 5.5 shows the phase and group speeds for the one-dimensional, second-order wave RKPM semi-discretization using the CF, CT, LF and HF formulations. Relative to the FE results of Figure 5.4, the consistent mass matrix (CF) provides better phase and group speed. Surprisingly, the trapezoidal mass formulation (CT) yields zero phase speed for $2\Delta x$ wavelengths, i.e., these wavelengths are stationary on the grid. Additionally, the CT formulation results in large, lagging group errors for wavelengths shorter than $3\Delta x$. In contrast, the FE semi-discretizations do not yield any negative group speeds.

Employing the 5% phase error criterion introduced earlier, the FE-HF method requires approximately 4 nodes per wavelength while only 3 particles are required for the RKPM-CF method. As with the RKPM discretization of the first-order wave equation, the lumped and higher-order formulations introduce severe lagging phase and group errors relative to both the FE counterparts and the CT and CF mass matrices.

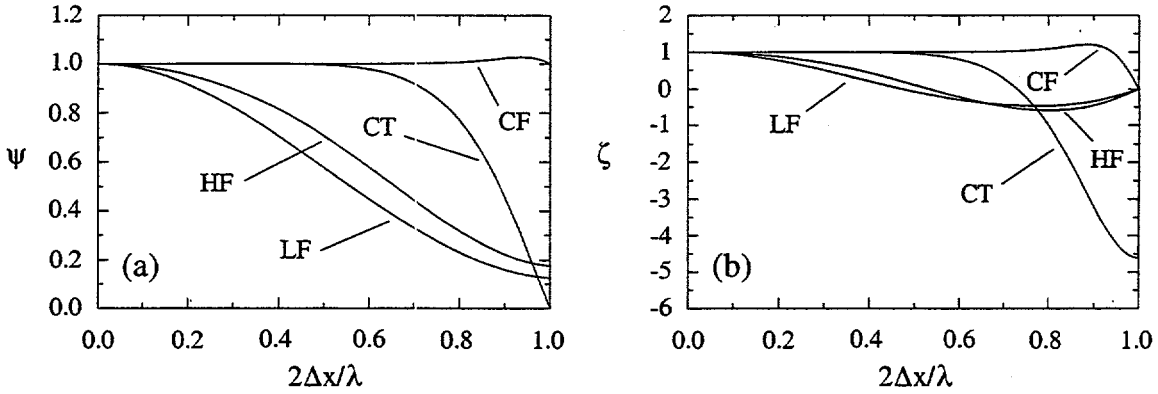

Figure 5.5: One-dimensional phase (a) and group (b) speed results for the second-order wave equation, Reproducing Kernel Particle semi-discretization employing the full-integration, consistent (CF), lumped (LF), higher-order (HF) and trapezoidal integration consistent (CT) mass matrix formulations.

5.2.2 2-D Hyperbolic Equations

This section presents the phase speed results for the semi-discrete, two-dimensional, hyperbolic equations. Results are plotted as functions of the propagation angle, θ, and non-dimensional wave number. For this analysis, the particle spacing is uniform with, $\Delta y/\Delta x = 1$. As with the one-dimensional analyses, a refinement parameter of $r = 1.14$ based upon a minimum energy error is used in the RKPM formulation. In order to highlight the directional dependence of the phase error, the phase speed is presented with both polar and Cartesian plots. The phase speed results exhibit angular symmetry about propagation directions, θ, that are multiples of $\pi/4$ as a result of the imposed uniform spacing of particles. However, the data is presented for $0 \leq \theta \leq 2\pi$ for the sake of clarity.

First-Order Wave Equation

Phase speed plots for the semi-discrete first-order wave equation using the fully integrated bi-linear finite element and a consistent mass matrix are shown in Figure 5.6. The polar plot of Figure 5.6a shows phase speed as a function of direction, θ, for several values of non-dimensional wavelength, $2\Delta x/\lambda$. The non-circular phase speed contours emphasize the anisotropic nature of wave propagation on the discrete mesh. Figure 5.6b presents the results of Figure 5.6a at five propagation angles, θ. It is apparent from Figure

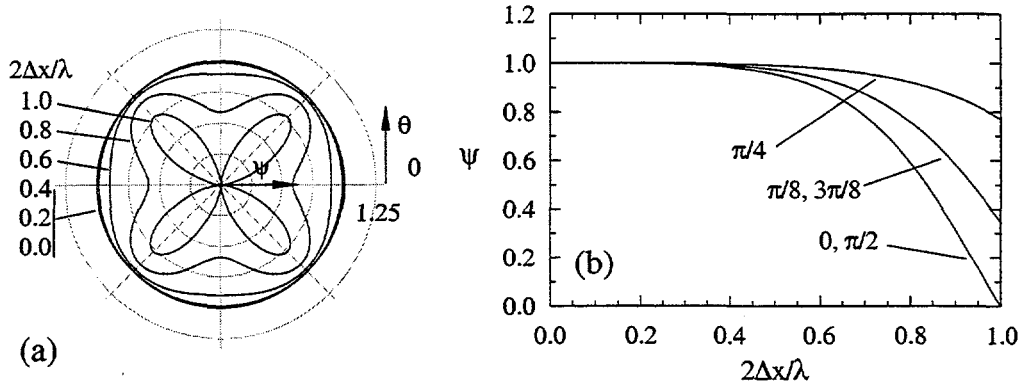

Figure 5.6: Polar (a) and Cartesian (b) plots of the phase speed for the FE semi-discretization of the two-dimensional, first-order wave equation employing a full-integration, consistent mass matrix formulation (CF).

5.6 that a minimum error in phase speed occurs when the wave propagation direction is $\pi/4$ from the x-axis. It is also apparent that the anisotropy becomes more pronounced for shorter wavelengths, i.e., $2\Delta x/\lambda > 0.4$ (cf. Figure 5.6a).

Phase speed results for the fully integrated "bi-linear" reproducing kernel particle method using a consistent mass matrix are shown in Figure 5.7. As with the FE formulation, the RKPM semi-discretization leads to strictly lagging phase speed with minimum phase speed errors occurring for $\theta = \pi/4$. However, unlike FE, RKPM shows negligible phase error in this direction. Further, relative to the finite element method, the anisotropic behavior has been significantly reduced, with wave propagation being effectively independent of wavelength and propagation direction for $2\Delta x/\lambda \leq 0.8$, i.e., for wavelengths greater than about $2 - 3\Delta x$.

Figure 5.8 shows polar and Cartesian plots of the phase speed for the "bi-linear" RKPM formulation using trapezoidal integration and a consistent mass matrix. Again, the phase speed is lagging and anisotropic, with minimum errors occurring in the $\theta = \pi/4$ directions. Although the phase speed appears anisotropic for short wavelength signals, this formulation delivers nearly isotropic wave propagation for $2\Delta x/\lambda \leq 0.6$, i.e., wavelengths greater than $3 - 4\Delta x$.

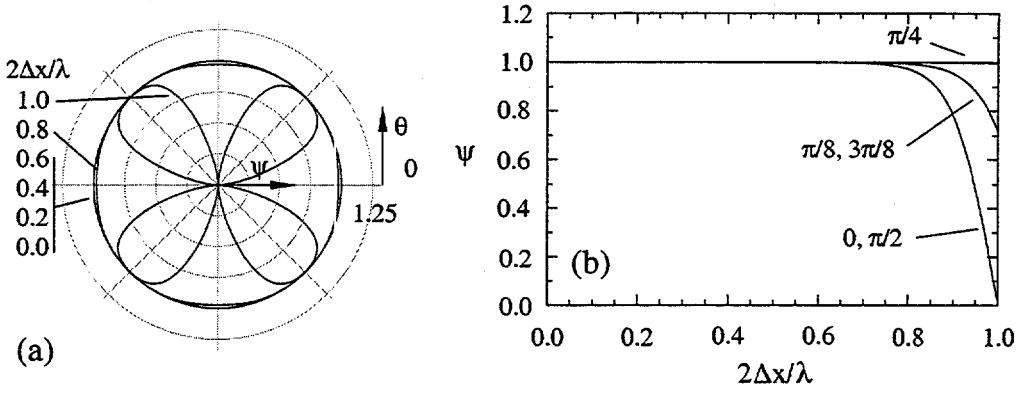

Figure 5.7: Polar (a) and Cartesian (b) plots of the phase speed for the RKPM semi-discretization of the two-dimensional, first-order wave equation with full-integration, and a consistent mass matrix (CF).

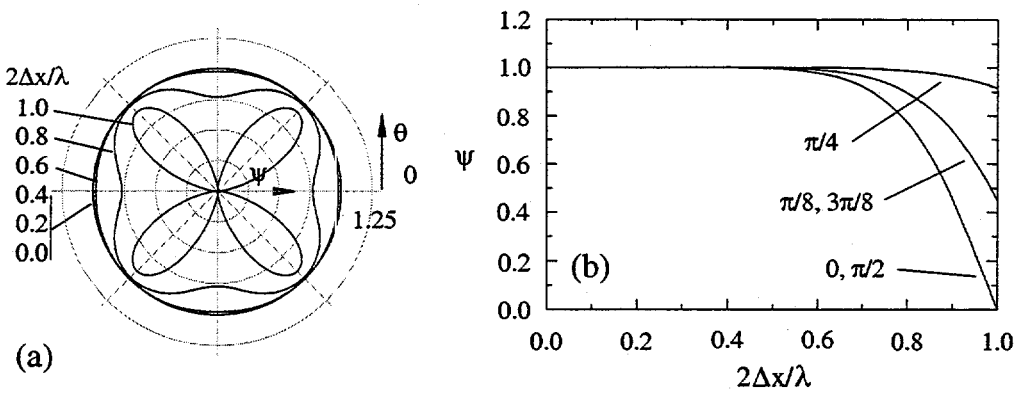

Figure 5.8: Polar (a) and Cartesian (b) plots of the phase speed for the RKPM semi-discretization of the two-dimensional, first-order wave equation with a consistent mass matrix and trapezoidal integration (CT).

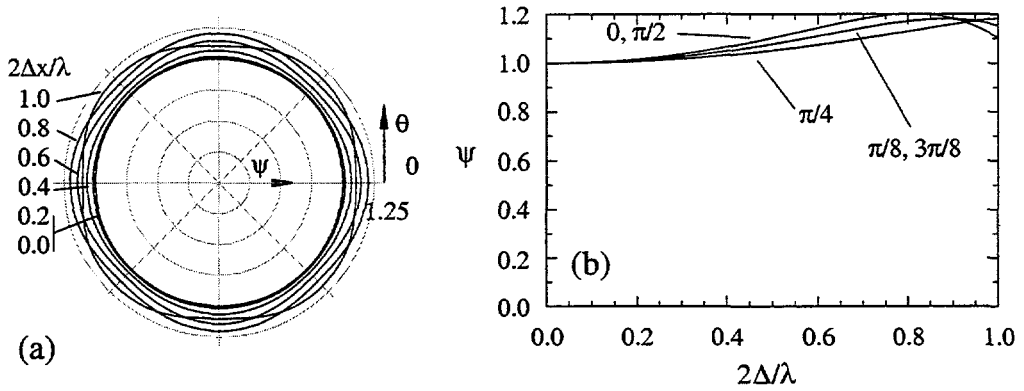

Figure 5.9: Polar (a) and Cartesian (b) plots of the phase speed for the FE semi-discretization of the two-dimensional, second-order wave equation using a full-integration, consistent mass matrix formulation (CF).

Second-Order Wave Equation

Figure 5.9 shows phase speed results for the second-order wave semi-discretization using a fully integrated bi-linear finite element method with a consistent mass matrix. The results indicate that the finite element formulation introduces strictly leading phase errors. The finite element semi-discretization results in anisotropic wave propagation, with a minimum phase error occurring in the $\theta = \pi/4$ propagation directions. However, the anisotropy is not as pronounced as for the first-order equation (cf. Figure 5.6)

The fully integrated "bi-linear" RKPM semi-discretization (consistent mass matrix) yields almost negligible phase errors as shown in Figure 5.10. Further, as phase errors are quite small for all θ, wave propagation is nearly perfectly isotropic. Some slight leading phase speed errors are evident for wavelengths approaching $2\Delta x$. However, these errors are less than 2.5% with a minimum in phase error occurring in the $\theta = \pi/4$ propagation directions.

Finally, Figure 5.11 shows the phase speed results for "bi-linear" RKPM semi-discretization using trapezoidal integration with a consistent mass matrix. Unlike the fully integrated results, anisotropic dispersion errors are quite evident for $2\Delta x/\lambda > 0.6$. However, for $2\Delta x/\lambda \leq 0.6$ phase errors are negligible and are significantly better than for the FE case (cf. Figure 5.9). Similar to the fully-integrated RKPM semi-discretization, the phase errors are minimized in the $\pi/4$ propagation directions, but with nearly perfect phase speed for wavelengths longer than $3 - 4\Delta x$.

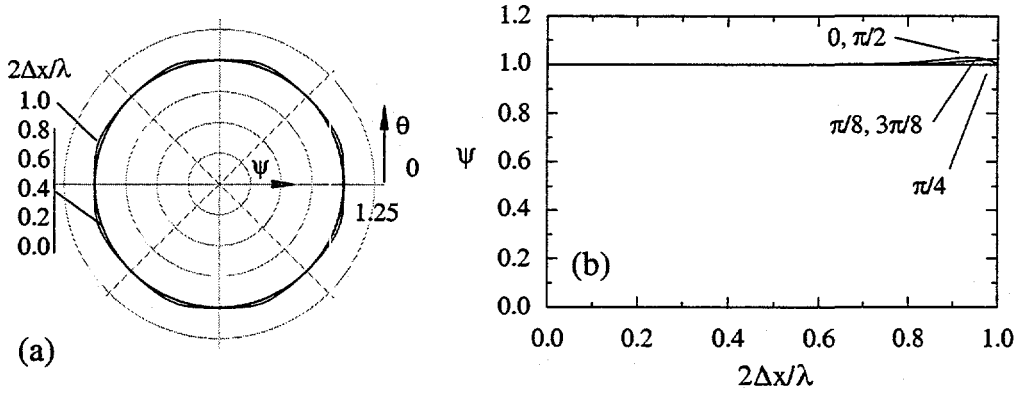

Figure 5.10: Polar (a) and Cartesian (b) plots of the phase speed for the RKPM semi-discretization of the two-dimensional, second-order wave equation using full-integration and a consistent mass matrix (CF).

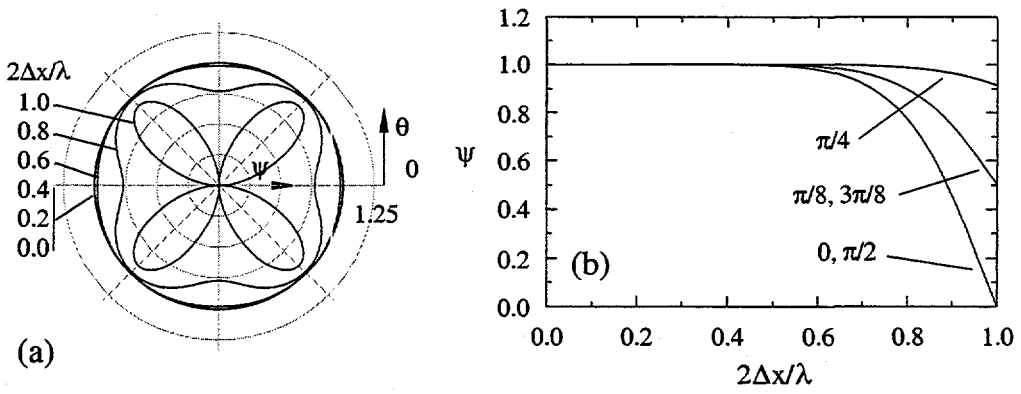

Figure 5.11: Polar (a) and Cartesian (b) plots of the phase speed for the RKPM semi-discretization of the two-dimensional, second-order wave equation using a consistent mass matrix and trapezoidal integration (CT).

Remark 15 *During the course of analyzing the results from the von Neumann analysis it was observed that the use of trapezoidal integration results in identical dispersion relations for the first and second-order wave equations with a consistent mass matrix. The fact that the discrete spectrum or* symbol[101] *for the first and second-order wave equations are identical may be seen clearly in Figures 5.3 and 5.5 for the one-dimensional case. Similarly, for the two-dimensional case, the phase speed shown for the first-order wave equation in Figure 5.8 is identical to the phase speed shown in Figure 5.11.*

Similar behavior has been noted by Vichnevetsky and Bowles[101] when a second-order central difference approximation is applied to both the first and second-order wave equation. In this situation, the semi-discrete first-order equation is a consistent representation of the second-order wave equation. In the case of RKPM, a similar result may be obtained in the one-dimensional case for a refinement parameter, $r = 1/2$. However, we have been unable to verify this behavior analytically for $r = 1.14$. Regardless of this, numerical experiments (cf. Figures 5.3, 5.5, 5.8, and 5.11) have verified that the discrete spectrum is identical for the two model hyperbolic equations when particle integration is used.

5.2.3 Parabolic Equation

The apparent diffusivity results are presented in Figure 5.12 for several RKPM semi-discretization techniques and a range of refinement parameters for the parabolic partial differential equation.

Figure 5.12 (a) shows the apparent diffusivity for the consistent mass, fully integrated formulation (CF) for refinement parameters 0.5, 0.75, 1.0, 1.14. Here, $r = 0.5$ corresponds to the usual finite element formulation with a consistent mass matrix and demonstrates that the shorter-wavelength modes will diffuse up to 40% faster than the long wavelength modes. As the refinement parameter approaches the minimum energy error value of 1.14, this effect is minimized with only a small error introduced for $2\Delta x/\lambda \geq 0.9$.

Figure 5.12 (b) shows the apparent diffusivity for RKPM using particle integration and a consistent mass matrix. Once again, the minimum energy error refinement parameter of 1.14 yields the best performance with nearly constant diffusivity up to $4\Delta x$ wavelengths. Surprisingly, all three refinement parameters result in apparent diffusivities that are zero for $2\Delta x$ wavelengths. Thus, any short-wavelength modes will not diffuse at all, but will persist on the grid.

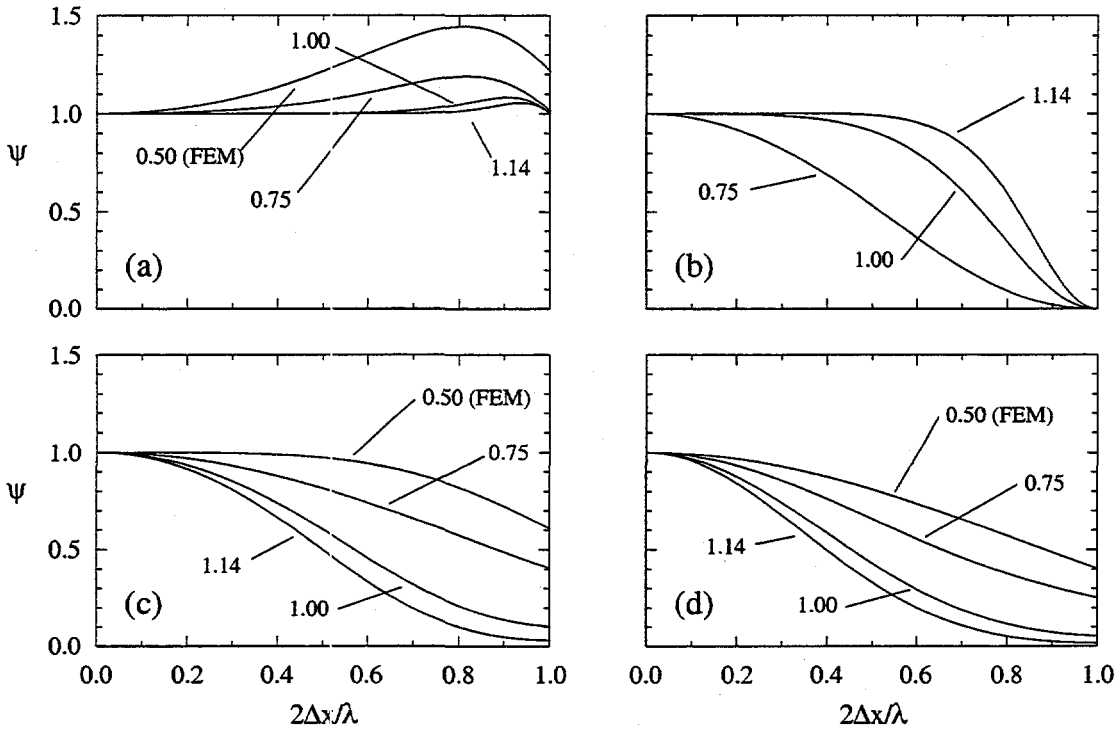

Figure 5.12: Parabolic PDE apparent diffusivity for the (a) fully integrated consistent mass (b) trapezoidal integration consistent mass (c) fully-integrated higher order mass and (d) fully-integrated lumped mass RKPM semi-discretizations.

Similar results are shown in Figure 5.12 when the lumped or higher-order mass matrix is used with a refinement parameter of 1.14. For the finite element formulation, i.e., $r = 0.5$, the apparent diffusivity is lagging for all wavelengths, but remains finite in the limit of $2\Delta x$ wavelengths. As in the case of the hyperbolic PDEs, the higher-order mass matrix yields the best overall behavior across the entire discrete spectrum. Unfortunately, any form of mass lumping procedure seems to severely deteriorate the performance of the RKPM formulation.

5.3 Summary

The results of the analyses presented here indicate that, for the formulations considered, the consistent mass RKPM-CF semi-discretizations display

better dispersion properties than the finite element method with similar consistency constraints. In a one-dimensional sense, phase errors of less than 5% are ensured with 3 to 4 particles per wavelength with RKPM while the FE formulations require 4 to 5 nodes. Incredibly, RKPM semi-discretizations of the second-order wave equation require only 3 particles per wavelength (the Nyquist limit) for phase errors of less than 2.5%. In addition, wave propagation with the consistent mass RKPM formulation in two-dimensions is nearly isotropic in terms of angular dependence of the phase speed and in terms of the amplitude of the phase errors.

While the consistent mass matrix RKPM formulations perform quite well, the lumped and higher order mass formulations introduce severely lagging phase and group speeds. Thus, the performance of these formulations is quite poor relative to their finite element counterparts.

Finally, the consistent mass RKPM results indicate that minimal losses in phase and group speed error result when particle integration of the matrices is employed in place of full (Gauss) quadrature. With the sacrifice of negative group speeds and a slight increase in phase speed errors, the use of particle integration may significantly reduce computational cost by reducing the number of quadrature points needed. Further, the method should be simpler to implement as the background integration mesh can be eliminated. However, further direct testing with particle integration is required.

Chapter 6

Summary and Conclusions

In the search for an optimal basis for performing multi-scale simulations, the following shopping list of characteristics was developed as the goal for the ideal multi-scale basis.

- Compact support.
- Low order, e.g., linear, for computational efficiency.
- Consistent reproduction of polynomials, e.g., reproduce $\{1, x, y, xy\}$ in two-dimensions.
- Nodal, i.e., possesses the Kronecker delta property.
- Hierarchical: $\mathcal{V}_1 = \mathcal{V}_0 \oplus \mathcal{W}_0$.
- Element based – compatible with isoparametric elements.
- Analytic expressions for the basis elements ϕ and ψ.
- Easy treatment of boundary conditions.
- Good numerical performance, e.g., dispersion characteristics, truncation error, etc.
- Appropriate for both Eulerian and Lagrangian computations.
- Computationally efficient decomposition and reconstruction of fields.
- Extensible to multiple spatial dimensions.

Based on these characteristics and the results of this exploratory effort the following conclusions are drawn.

1. The DGHM (and related) multi-wavelets are not a good choice for a multi-scale basis because they are relatively difficult to compute with and do not extend to multiple dimensional isoparametric elements. In addition, the DGHM element delivers the performance of a linear element at the cost of a quadratic element with inferior dispersive behavior.

2. The Schauder basis, and the 1-D and 2-D multi-scale elements, are prototypical of what the ideal multi-scale basis should be. Unfortunately, the storage and computational cost associated with the finger-diagonal operators from this type of basis is a significant penalty. However, the use of ad-hoc lumping procedures ameliorates this problem and offers the potential for the development of fast, simple preconditioners. Currently, the real value of the multi-scale elements lies in the application to elliptic problems.

3. The numerical performance of the reproducing kernel particle method makes it a viable candidate for both Eulerian and Lagrangian computations for a broad range of physical problems. However, the integration of wavelets with the multiple scale window functions remains a topic of current research. This research is currently being addressed by Professor Wing Kam Liu and his colleagues at Northwestern University.

4. As demonstrated in the discussion of the "semi-hat" bases, it is difficult to construct a basis that is stable in both $\mathbf{L}^2$ and in H^1, i.e., for all possible combinations of mass and stiffness operators. The application of wavelet bases that have been customized for a specific partial differential equation remains an open topic of active research.

5. The use of wavelet bases for the solution of partial differential equations remains a research topic that is centered squarely in the mathematics community at this time. Hierarchical solution procedures that use wavelets tailored to the physical problem appear to be the most viable candidates for using wavelet bases.

Recommendations for further work

1. At this time, the multi-scale elements are the best choice for a "wavelet" basis that can be implemented in existing finite element codes. The development of a preconditioner based upon the multi-scale element would be of great value in applications such as time-dependent incompressible flow, quasi-static electro-magnetics, as well as the obvious application to conduction problems, where there is a dominant elliptic component. The row-column lumping procedure combined with the element-based reconstruction algorithm can yield a computationally efficient preconditioner or multi-level solution scheme.

2. Another potential application for the 1-D multi-scale element is in the one-dimensional turbulence (ODT) sub-grid scale modeling efforts. Here, the implementation of a fast solution to the 1-D parabolic problem could aid in reducing the computational complexity of this approach.

3. The application of RKPM to high-rate, large-deformation physical problems has been demonstrated, but there are still many questions to be answered. Of particular concern here is the application to shock dominated problems and the construction of a viable artificial viscosity treatment. There is a clear need for continued refinement of search algorithms for the numerical integration procedures in RKPM.

4. The implementation of two-scale decomposition strategies based upon the finite-domain convolution kernel of RKPM promises to yield filtering strategies that can be used in a stand-alone mode for post-processing simulation results. In addition, this type of filter possesses consistency properties that make it a viable candidate for explicit filtering in large eddy simulations where a dynamic sub-grid scale model is used.

Bibliography

[1] K. AMARTUNGA AND J. R. WILLIAMS, *Wavelet-galerkin solutions for one-dimensional partial differential equations*, International Journal for Numerical Methods in Engineering, 37 (1994), pp. 2703–2716.

[2] A. AVERBUCH, G. BELYKIN, R. COIFMAN, AND M. ISRAELI, *Multiscale inversion of elliptic operators*, Signal and Image Representation in Combined Spaces, (1995). (preprint).

[3] T. BELYTSCHKO, Y. KRONGAUZ, D. ORGAN, M. FLEMING, AND P. KRYSL, *Meshless methods: An overview and recent developments*, Computer Methods in Applied Mechanics and Engineering, 139 (1996), pp. 3–47.

[4] T. BELYTSCHKO AND R. MULLEN, *On dispersive properties of finite element solutions*, in Modern Problems in Elastic Wave Propagation, J. Milovitz and J. D. Achenbach, eds., International Union of Theoretical and Applied Mechanics, John Wiley and Sons, 1978, pp. 67–82.

[5] G. BEYLKIN, *Wavelets, multiresolution analysis and fast numerical algorithms*, INRIA lecturs, (1991).

[6] ——, *On the representation of operators in bases of compactly supported wavelets*, SIAM Journal on Numerical Analysis, 6 (1992), pp. 1716–1740.

[7] ——, *On the representation of operators in bases of compactly supported wavelets*, SIAM Journal on Numerical Analysis, 6 (1992), pp. 1716–1740.

[8] ——, *On the adaptive numerical solution of nonlinear partial differential equations*, preprint, (1993). (ftp://amath-ftp.colorado.edu/pub/wavelets/papers/wavelets_for_PDEs.ps.Z).

[9] ——, *Wavelets and fast numerical methods*, Proceedings of Symposia in Applied Mathematics, 47 (1993), pp. 89–117.

[10] G. BEYLKIN, R. COIFMAN, AND V. ROKHLIN, *Fast wavelet transforms and numerical algorithms i.*, preprint, (unknown).

[11] G. BEYLKIN AND N. COULT, *A multiresolution strategy for reduction of elliptic pde's and eigenvalue problems*, Applied and Computational Harmonic Analysis, 5 (1998), pp. 129–155.

[12] J. H. BRAMBLE, J. E. PASCIAK, AND J. XU, *Parallel multilevel preconditioners*, Mathematics of Computation, 55 (1982), pp. 1–22.

[13] W. CAI AND J. WANG, *Adaptive multiresolution collocation methods for initial boundary value problems of nonlinear pdes*, SIAM Journal on Numerical Analysis, 33 (1996), pp. 937–970.

[14] W. CAI AND J. Z. WANG, *Adaptive wavelet collocation methods for initial value boundary problems of nonlinear pde's*, Tech. Rep. ICASE Report No. 93-48, Institute for Computer Applications in Science and Engineering, July 1993.

[15] W. CAI AND W. ZHANG, *An adaptive spline wavelet adi (sw-adi) method for two-dimensional reaction-diffusion equations*, to appear in Journal of Computational Physics, (1997).

[16] P. CHARTON AND V. PERRIER, *A pseudo-wavelet scheme for the two-dimensional navier-stokes equations*, tech. rep., Laboratorie de Meteorologie Dyanmique du CNRS, Paris, France, 1996. (ftp://ftp.lmd.ens.fr/MFGA/pub/wavelets/ns.ps.Z).

[17] J.-S. CHEN, S. YOON, H.-P. WANG, AND W. K. LIU, *An improved reproducing kernel particle method for nearly incompressible hyperelastic solids*, submitted to Computer Methods in Applied Mechanics and Engineering, (1997).

[18] Y. CHEN, R. A. URAS, AND W. K. LIU, *Enrichment of the finite element method with reproducing kernel particle method*, in Joint ASME/JSME pressure vessels and piping conference, ASME/JSME, July 1995.

[19] M. A. CHRISTON, *The influence of the mass matrix on the dispersive nature of the semi-discrete, second-order wave equation*, Computer Methods in Applied Mechanics and Engineering, (accepted for publication, June, 1998). (Sandia SAND95-1979J).

[20] C. K. CHUI, *Wavelets: A Mathematical Tool for Signal Analysis*, Society for Industrial and Applied Mathematis, Philadelphia, Pennsylvania, 1997.

[21] A. COHEN AND R. MASSON, *Wavelet methods for second order elliptic problems, preconditioning and adaptivity*, preprint, (1997).

[22] S. DAHLKE AND A. KUNOTH, *Biorthogonal wavelets and multigrid*, Tech. Rep. 84, Institute for Geometry and Applied Mathematics – RWTH Aachen, Aachen, Germany, April 1993.

[23] S. DAHLKE AND I. WEINREICH, *Wavelet-galerkin methods: An adapted biorthogonal wavelet basis*, Contructive Approximation, 9 (1993), pp. 237–262.

[24] S. DAHLKE AND I. WEINREICH, *Wavelet-galerkin methods: An adapted biorthogonal wavelet basis*, Constr. Approx., 9 (1993), pp. 237–262.

[25] ——, *Wavelet bases adapted to pseudo-differential operators*, Applied Comput. Harmonic Anal., 1 (1994), pp. 267–283.

[26] W. DAHMEN, *Stability of multiscale transformations*, J. Fourier Anal. Appl., 2 (1996), pp. 341–362.

[27] ——, *Wavelet and multiscale methods for operator equations*, Acta Numerica, (1997), pp. 55–228.

[28] W. DAHMEN AND A. KUNOTH, *Multilevel preconditioning*, Numerishe Mathematik, 63 (1992), pp. 314–344.

[29] W. DAHMEN, A. KUNOTH, AND K. URBAN, *A wavelet-galerkin method for the stokes equations*, Tech. Rep. 111, Institute for Geometry and Applied Mathematics, RWTH Aachen, Aachen, Germany, February 1995. (ftp://ftp.igpm.rwth-aachen.de/pub/urban/igpm_111.tar.Z).

[30] W. DAHMEN, A. KURDILLA, AND P. OSWALD, eds., *Multiscale wavelet methods for partial differential equations*, vol. 6, Academic Press, San Diego, California, 1997.

[31] W. DAHMEN AND C. A. MICCHELLI, *Using the refinement equation for evaluating integrals of wavelets*, SIAM Journal on Numerical Analysis, 30 (1993).

[32] ——, *Biorthogonal wavelet expansions*, Tech. Rep. 114, Institute for Geometry and Applied Mathematics – RWTH Aachen, Aachen, Germany, May 1995.

[33] W. DAHMEN, S. MULLER, AND T. SCHLINKMANN, *Multigrid and multiscale decompositions*, Tech. Rep. 147, Institute for Geometry and Applied Mathematics – RWTH Aachen, Aachen, Germany, September 1997.

[34] W. DAHMEN AND R. STEVENSON, *Element-by-element construction of wavelets satisfying stability and moment conditions*, submitted to SIAM journal on Numerical Analysis, (1997). (see also Report No. 9725, Mathematics Department, University of Nijmegen).

[35] I. DAUBECHIES, *Orthonormal bases of compactly supported wavelets*, Communications on Pure and Applied Mathematics, XLI (1988), pp. 909–996.

[36] ——, *Ten lectures on wavelets*, SIAM, Philadelphia, Pennsylvania, 1992.

[37] G. DONOVAN, J. S. GERONIMO, AND D. P. HARDIN, *Fractal functions, splines intertwining multiresolution analysis and wavelets*, in Proceedings of SPIE, San Diego, California, July 1994, SPIE, pp. 238–243.

[38] G. C. DONOVAN, J. S. GERONIMO, D. P. HARDIN, AND P. R. MASSOPUST, *Construction of orthogonal wavelets using fractal interpolation functions*, SIAM Journal on Mathematical Analysis, 27 (1996), pp. 1158–1192.

[39] J. FROHLICH AND K. SCHNEIDER, *An adaptive wavelet-vaguelette algorithm for the solution of pdes*, Journal of Computational Physics, 130 (1997), pp. 174–190.

[40] J. S. GERONIMO, D. P. HARDIN, AND P. R. MASSOPUST, *Fractal functions and wavelet expansions based on several scaling functions*, Journal of Approximation Theory, 78 (1994), pp. 373–401.

[41] R. GLOWINSKI, W. LAWTON, M. RAVACHOL, AND E. TENENBAUM, *Wavelet solutions of linear and nonlinear elliptic, parabolic and hyperbolic problems in one space dimension*, in Computing Methods in Applied Sciences and Engineering, R. Glowinski, ed., Philadelphia, Pennsylvania, January 1990, SIAM, SIAM, pp. 55–120.

[42] R. GLOWINSKI, T.-W. PAN, J. RAYMOND O. WELLS, AND X. ZHOU, *Wavelet and finite element solutions for the dirichlet problem*, (ftp://cml.rice.edu/pub/reports/9201.ps.Z) TR92-01, Computational Mathematics Laboratory, Rice University, Houston, Texas, 1992.

[43] R. GLOWINSKI, A. RIEDER, R. O. WELLS, AND X. ZHOU, *A wavelet multigrid preconditioner for dirichlet boundary-value problems in general domains*, Tech. Rep. TR93-06, Computational Mathematics Laboratory, Rice University, Houston, Texas, 1994. (ftp://cml.rice.edu/pub/reports/9306.ps.Z).

[44] A. GRAPS, *An introduction to wavelets*, IEEE Computational Science and Engineering, 2 (1995), pp. 1–18.

[45] P. M. GRESHO, S. T. CHAN, R. L. LEE, AND C. D. UPSON, *A modified finite element method for solving the time-dependent, incompressible navier-stokes equations. part 1: Theory*, International Journal for Numerical Methods in Fluids, 4 (1984), pp. 557–598.

[46] P. M. GRESHO AND R. L. SANI, *Incompressible flow and the finite elmeent method, Advection-diffusion and isothermal laminar flow*, John Wiley & Sons, Chicester, England, 1998.

[47] A. GROSSMANN AND J. MORLET, *Decomposition of hardy functions into square integrable wavelets of constant shape*, SIAM Journal on Mathematical Analsysis, 15 (1984), pp. 723–736.

[48] W. HACKBUSCH, *The frequency decomposition multi-grid method, part i: Application to anisotropic equations*, Numerische Mathematik, 56 (1992), pp. 229–245.

[49] A. HARTEN, *Multi-resolution algorithms for the numerical solution of hyperbolic conservation laws*, Communications on Pure and Applied Mathematics, XLVIII (1995), pp. 1305–1342.

[50] M. HOLMSTROM, *Solving hyperbolic pdes using interpolating wavelets*, Tech. Rep. 189/1996, Uppsala University – Department of Scientific Computing, Uppsala, Sweden, December 1996.

[51] T. J. R. HUGHES, *The Finite Element Method*, Prentice-Hall, Inc., Englewood Cliffs, New Jersey, 1987.

[52] S. JAFFARD, *Wavelet methods for fast resolution of elliptic problems*, SIAM Journal on Numerical Analysis, 29 (1992), pp. 956–986.

[53] L. JAMESON, *On the wavelet optimized finite difference method*, Tech. Rep. NASA CR-191601, ICASE Report No. 94-9, Institute for Computer Applications in Science and Engineering, NASA Langley Research Center, Hampton, VA, March 1994.

[54] B. JAWERTH AND W. SWELDENS, *An overview of wavelet based multiresolution analyses*, preprint, (1997).

[55] S. JUN, W. K. LIU, AND T. BELYTSCHKO, *Explicit reproducing kernel particle methods for large deformation problems*, International Journal for Numerical Methods in Engineering, (1997).

[56] J. M. KEISER, *On I. Wavelet based approach to numerical solution of nonlinear partial differential equations and II. Nonlinear waves in fully discrete dynamical systems*, PhD thesis, University of Colorado, Boulder, Colorado, 1995.

[57] J. KO, A. J. KURDILA, AND P. OSWALD, *Multiscale Wavelet Methods for PDEs*, Academic Press, Inc., 1996, ch. Scaling Function and

Wavelet Preconditioners for Second Order Elliptic Problems, pp. 413–438.

[58] J. Ko, A. J. Kurdila, and M. P. Pilant, *Triangular wavelet based finite elements via multivalued scaling functions*, preprint, (1994).

[59] A. Kunoth, *Multilevel preconditioning – appending boundary conditions by lagrange multipliers*, tech. rep., Institute for Geometry and Applied Mathematics –RWTH - Aachen, Aachen, Germany, December 1994.

[60] A. Latto and H. L. Resnikoff, *The evaluation of connection coefficients of compactly supported wavelets*, Tech. Rep. AD910798, Aware, Inc., Cambgridge, Massachussets, August 1996.

[61] A. Latto and E. Tenenbaum, *Compactly supported wavelets and the numerical solution of burger's equation*, C. R. Academy of Sciences, 311 (1990), pp. 903–909.

[62] S. Li and W. K. Liu, *Moving least square reproducing kernel method part ii: Fourier analysis*, Computer Methods in Applied Mechanics and Engineering, 139 (1996), pp. 159–193.

[63] ——, *Synchronized reproducing kernel interpolant via multiple wavelet expansion*, Computational Mechanics, (Accepted for publication March, 1997).

[64] ——, *Moving least square reproducing kernel method (iii): Wavelet packet and its applications*, Computer Methods in Applied Mechanics, (submitted April, 1997).

[65] W. K. Liu and Y. Chen, *Wavelet and multiple scale reproducing kernel methods*, International Journal for Numerical Methods in Fluids, 21 (1995), pp. 901–931.

[66] W. K. Liu, Y. Chen, C. T. Chang, and T. Belytschko, *Advances in multiple scale kernel particle methods*, Computational Mechanics, 18 (1996), pp. 73–111.

[67] W. K. Liu, Y. Chen, J. S. Chen, T. Belytschko, C. Pan, R. A. Curas, and C. T. Chang, *Overview and applications of the reproducing kernel particle methods*, Archives of Computational Methods in Engineering, 3 (1996), pp. 3–80.

[68] W. K. Liu, Y. Chen, R. A. Uras, and C. T. Chang, *Generalized multiple scale reproducing kernel particle methods*, Computer Methods in Applied Mechanics and Engineering, 139 (1996), pp. 91–157.

[69] W. K. Liu and S. Jun, *Multiple scale reproducing kernel particle methods for large deformation problems*, International Journal for Numerical Methods in Engineering, (submitted 1997).

[70] W. K. Liu, S. Jun, S. Li, J. Adee, and T. Belytschko, *Reproducing kernel particle methods for structural dynamics*, International Journal for Numerical Methods in Engineering, 38 (1995), pp. 1655–1679.

[71] W. K. Liu, S. Jun, and Y. F. Zhang, *Reproducing kernel particle methods*, International Journal for Numerical Methods in Fluids, 20 (1995), pp. 1081–1106.

[72] W. K. Liu, S. Li, and T. Belytschko, *Moving least square reproducing kernel methods (i) methodology and convergence*, Computer Methods in Applied Mechanics and Engineering, (Accepted for publication - June, 1996).

[73] W. K. Liu and C. Oberste-Brandenburg, *Reproducing kernel and wavelet particle methods*, in Aerospace Structures: Nonlinear dynamics and system response, J. P. Cusumano, C. Peirre, and S. T. Wu, eds., New York, New York, November 1993, ASME Winter Annual Meeting, American Society of Mechanical Engineers, pp. 39–55.

[74] S. G. Mallat, *Multiresolution approximations and wavelet orthonormal bases of $l^2(r)$*, Transactions of the American Mathematical Society, 315 (1989), pp. 69–87.

[75] P. R. Massopust, *Fractal functions, fractal surfaces and wavelets*, Academic Press, San Diego, California, 1994.

[76] ——, *Lecture notes for multiwavelets and their application.* presented at Allegheny section of the MAA, June 1997.

[77] Y. MEYER, *Wavelets Algorithms and Applications*, SIAM, Philadelphia, Pennsylvania, 1993.

[78] P. MONASSE AND V. PERRIER, *Orthonormal wavelet bases adapted for partial differential equations with boundary conditions*, tech. rep., Laboratore de Meteorlogie Dynamique, Paris, Paris, France, October 1995.

[79] J. MORLET, *NATO ASI Series, Issues in Acoustic Signal/Image Processing and Recognition*, vol. 1, Springer, Berlin, 1983, ch. Sampling theory and wave propagation, pp. 233–261.

[80] J. MORLET, G. ARENS, I. FOURGEAU, AND D. GIARD, *Wave propagation and sampling theory*, Geophys., 47 (1982), pp. 203–236.

[81] P. OSWALD, *Multilevel finite element approximation*, B. G. Teubner, Stuttgart, Germany, 1994, ch. 4. Applications to multilevel methods, pp. 70–115.

[82] V. PERRIER AND P. CHARTON, *Towards a wavelet based numerical scheme for the two-dimensional navier-stokes equations*, tech. rep., Laboratorie de Meteorologie Dyanmique du CNRS, Paris, France, 1995. (ftp://ftp.lmd.ens.fr/MFGA/pub/wavelets/iciam95.ps.Z).

[83] G. PLONKA AND V. STRELA, *Mathematical Methods for Curves and Surfaces II*, Vanderbilt University Press, Nashville, Tennessee, 1998, ch. From wavelets to multiwavelets, pp. 375–399.

[84] S. QIAN AND J. WEISS, *Wavelets and the numerical solution of partial differential equations*, Journal of Computational Physics, 106 (1993), pp. 155–175.

[85] A. RIEDER, R. O. WELLS, AND X. ZHOU, *A wavelet approach to robust multilevel solvers for anisotropic elliptic problems*, Tech. Rep. TR93-07, Computational Mathematics Laboratory, Rice University, Houston, Texas, 1993. (ftp://cml.rice.edu/pub/reports/9307.ps.Z).

[86] ——, *On the wavelet frequency decomposition method*, Tech. Rep. TR94-13, Computational Mathematics Laboratory, Rice University, Houston, Texas, 1994. (ftp://cml.rice.edu/pub/reports/9413.ps.Z).

[87] D. W. ROACH, *Multiwavelet prefilters: orthogonal prefilters preserving approximation order p <= 3*, PhD thesis, Vanderbilt University, Nashville, Tennesee, May 1997.

[88] G. STRANG, *Wavelets and dilation equations: a brief introduction*, SIAM Review, 31 (1989), pp. 614–627.

[89] ——, *Wavelets*, American Scientist, 82 (1994), pp. 250–255.

[90] V. STRELA, *Multiwavelets: Theory and Applications*, PhD thesis, Massachusetts Institute of Technology, Boston, Massachusetts, June 1996.

[91] V. STRELA AND G. STRANG, *Finite element multiwavelets*, in Maratea NATO Conference, NATO, Kluwer, 1995.

[92] V. STRELA AND G. STRANG, *Pseudo-biorthogonal multiwavelets and finite elements*, preprint, (1997). (*http : //pascal.dartmouth.edu/ strela*).

[93] R. S. STRICHARTZ, *How to make wavelets*, The American Mathematical Monthly, 100 (1993), pp. 539–556.

[94] W. SWELDENS, *Compactly supported wavelets which are biorthogonal with respect to a weighted inner product*, preprint, (1996).

[95] C. H. TONG, T. F. CHAN, AND C. C. J. KUO, *A domain decomposition preconditioner base on a change to a multilevel nodal basis*, SIAM Journal on Scientific and Statistical Computing, 12 (1991).

[96] R. A. URAS, C. T. CHANG, Y. CHEN, AND W. K. LIU, *Multiresolution reproducing kernel particle methods in acoustics*, Journal of Computational Acoustics, (Accepted for publication, 1996).

[97] K. URBAN, *A wavelet-galerkin algorithm for the driven-cavity-stokes-problem in two space dimensions*, Tech. Rep. 106, Institute for Geometry and Applied Mathematics, RWTH Aachen, Aachen, Germany, September 1994. (ftp://ftp.igpm.rwth-aachen.de/pub/urban/igpm_106.tar.Z).

[98] O. V. VASILYEV AND S. PAOLUCCI, *A dynamically adaptive multilevel wavelet collocation method for solving partial differential equations in a finite domain*, Journal of Computational Physics, 125 (1996), pp. 498–512.

[99] ——, *A fast adaptive wavelet collocation algorithm for multidimensional pdes*, Journal of Computational Physics, 138 (1997), pp. 16–56.

[100] R. VICHNEVETSKY, *Wave propagation and reflection in irregular grid for hyperbolic equations*, Tech. Rep. MAE-1713, Department of Mechanical and Aerospace Engineering, Princeton University, July 1985.

[101] R. VICHNEVETSKY AND J. B. BOWLES, *Fourier Analysis of Numerical Approximations of Hyperbolic Equations*, SIAM, Philadelphia, PA, 1982.

[102] G. G. WALTER, *Orthogonal finite element multiwavelets*, preprint – Mathematical Science Department, University of Wisconsin-Milwaukee, (1997).

[103] J. WEISS, *The numerical resolution of turbulence and boundary value problems using the wavelet-galerkin method*, preprint, (1997).

[104] R. O. WELLS AND X. ZHOU, *Representing the geometry of domains by wavelets with applications to differential equations*, Tech. Rep. TR92-14, Computational Mathematics Laboratory, Rice University, Houston, Texas, 1992. (ftp://cml.rice.edu/pub/reports/9214.ps.Z).

[105] ——, *Wavelet solutions for the dirichlet problem*, Tech. Rep. TR92-02, Computational Mathematics Laboratory, Rice University, Houston, Texas, 1993. (ftp://cml.rice.edu/pub/reports/9202.ps.Z).

[106] D. C. WILCOX, *Turbulence Modeling for CFD*, DCW Industries, Inc., La Canada, California, 1993.

[107] J. R. WILLIAMS AND K. AMARTUNGA, *Introduction to wavelets in engineering*, International Journal for Numerical Methods in Engineering, 37 (1994), pp. 2365–2388.

[108] J.-C. XU AND W.-C. SHANN, *Galerkin-wavelet methods for two-point boundary value problems*, Numerishe Mathematik, 63 (1992), pp. 123–144.

[109] H. YSERENTANT, *On the multi-level splitting of finite element spaces*, Numerishce Mathematik, 49 (1986), pp. 379–412.

[110] H. YSERENTANT, *On the multi-level splitting of finite element spaces*, Numerisch Mathematic, 49 (1986), pp. 379–412.

[111] H. YSERENTANT, *Two preconditioners based on the multi-level splitting of finite element spaces*, Numerische Mathematik, 58 (1990), pp. 163–184.

[112] O. C. ZIEKIEWICZ, D. W. KELLEY, J. GAGO, AND I. BABUSKA, *The mathematics of finite elements and applications IV*, Academic Press, London, England, 1982, ch. Hierarchical finite element approaches, error estimates and adaptive refinement.

Distribution

External Distribution:

Prof. Ted Belytschko
Mechanical Engineering Dept.
Northwestern University
2145 Sheridan Road
Evanston, Illinois 60208-3111

Prof. Patrick J. Burns
Mechanical Engineering Dept.
Colorado State University
Ft. Collins, CO 80523

Dr. F. Farassat
NASA Langley Research Center
Mail Stop 460
Hampton, VA 23681-0001

Philip M. Gresho, Ph.D.
Lawrence Livermore National Laboratory
P.O. Box 808, L-262
Livermore, California 94551

Douglas P. Hardin
Mathematics Department
Vanderbilt University
Nashville, TN 37420

Prof. Thomas J. R. Hughes
Division of Applied Mechanics
Durand Building
Room No. 281
Stanford University
Stanford, California 94305-4040

Prof. Wing Kam Liu
Mechanical Engineering Dept.
Northwestern University
2145 Sheridan Road
Evanston, Illinois 60208-3111

Peter R. Massopust
7 S. Acacia Park Circle
The Woodlands, TX 77382

Prof. Philip J. Morris
Department of Aerospace Engineering
The Pennsylvania State University
University Park, PA 16802

Prof. Tayfun Tezduyar
AHPCRC
University of Minnesota
1100 Washington Avenue South
Minneapolis, MN 55415

Prof. Erik Thompson
Civil Engineering Dept.
Colorado State University
Ft. Collins, CO 80523

Prof. Don H. Tucker
Department of Mathematics
University of Utah
Salt Lake City, UTAH 84112

David W. Roach
Mathematics Department
University of Georgia
Athens, Georgia 30602

Prof. Jiun-Shyan Chen
Department of Mechanical Engineering
The University of Iowa
2133 Engineering Building
Iowa City, Iowa 52242-1527

Internal Distribution:

1	MS 0321	W. J. Camp, 9200
1	MS 0819	J. S. Peery, 9231
1	MS 0820	P. Yarrington, 9232
1	MS 1111	S. Dosanjh, 9221
1	MS 1111	B. Hendrickson, 9226
1	MS 1111	S. Plimpton, 9221
1	MS 0807	R. Haynes, 4918
1	MS 0819	D. Carroll, 9231
1	MS 0820	D. Crawford, 9232
20	MS 0819	M. Christon, 9231
1	MS 0819	E. Hertel, 9231
1	MS 0819	A. Robinson, 9231
1	MS 0819	J. R. Weatherby, 9231
1	MS 0835	T. E. Voth, 9113
2	MS 0825	R. S. Baty, 9115
1	MS 0836	S. P. Burns, 9116
1	MS 0819	T. G. Trucano, 9231
1	MS 1110	D. E. Womble, 9222

1	MS 0841	C. M. Hartwig, 9102
1	MS 0632	J. C. Hogan, 5507
1	MS 1207	D. A. Yocky, 5912
1	MS 0841	P. J. Hommert, 9100
1	MS 0828	T. C. Bickel, 9101
1	MS 0828	R. K. Thomas, 9104
1	MS 1111	T. Smith, 9221
1	MS 0865	J. L. Moya, 9105
1	MS 0826	W. L. Hermina, 9111
1	MS 0834	A. C. Ratzel, 9112
1	MS 0835	S. N. Kempka, 9113
1	MS 0827	R. O. Griffith, 9114
1	MS 0825	W. H. Rutledge, 9115
1	MS 0836	C. W. Peterson, 9116
1	MS 0836	J. H. Strickland, 9116
1	MS 0443	H. S. Morgan, 9117
1	MS 0439	D. R. Martinez, 9234
1	MS 9214	C. H. Tong, 8950
1	MS 0188	D. L. Chavez, LDRD Office, 4001
1	MS 9018	Central Technical Files, 8940-2
2	MS 0899	Technical Library, 4916
1	MS 0619	Review & Approval Desk, 15102 for DOE/OSTI